Spectral properties of X-ray background sources

Dissertation

Der Fakultät für Physik
der Ludwig-Maximilians-Universität München

zur Erlangung des Grades
Doktor der Naturwissenschaften
Dr. rer. nat.
vorgelegt von

Alina Streblyanska

aus Charkiv, Ukraine

München, den 5. Januar 2006

1. Gutachter: Prof. Dr. Ralf Bender
2. Gutachter: Prof. Dr. Hans Böhringer

Tag der mündlichen Prüfung: 31. Jan 2006

Summary

In this thesis we analysed the deepest XMM-Newton observations of the Chandra Deep Field South and the Lockman Hole. These two reference fields for studies of different X-ray background source classes, provide a unique opportunity to study physical and evolutionary properties of distant normal and active galaxies, clusters of galaxies and even faint Galactic stars using statistically significant samples. The main goal of the work was a further improvement of the knowledge about X-ray properties of AGN and galaxies in the distant Universe using the statistical treatment of these large samples of detected sources.

The main results of this work are as follows:

The 370 ksec XMM-Newton observation of the CDFS yielded 363 sources. The derived log N–log S relation is consistent with previous Chandra 1 Ms results. The cumulative number counts in the very hard band (5–10 keV) have a steeper slope than the soft (0.5–2 keV) and hard (2–10 keV) band source counts. Consistent with the models, most of the sources contributing to this band should be strongly absorbed AGN at relatively low redshifts. Comparison between the XMM-Newton and two independent deep Chandra catalogs reveal an excellent agreement in ($\sim$ 2 arcsec) between the source positions, showing that the XMM-Newton datasets are not significantly affected by source confusion. The derived fluxes reveal a reasonable agreement between the three observations, however with a noticeable scatter for sources with lower hard band fluxes. The scatter could indicate possible variability of some of the AGN between the different observation epochs, although it could also be due to systematic effects of the source detection procedure. We create a catalog of the 15 extended sources in our field, 7 of them are known previously from the deep Chandra observation and have been identified with galaxies and groups/clusters of galaxies. From the number of the detected extended sources we estimated the cluster number density of 84$\pm$ 22 clusters per square degrees at the 4×10^{-16} erg cm^{-2} s^{-1} flux level in the 0.5–2 keV band. Such cluster number density is among the highest known, and in agreement with other estimates at such flux levels. Our preliminary spectral analysis of these objects shows that the X-ray luminosities ($L_X \sim 10^{41}$–10^{43} erg s^{-1}) and temperatures ($kT < 3$ keV) are in good agreement with previous findings for such bright sources. From colour-colour and colour-flux diagrams we found that 165 newly detected XMM-Newton sources have similar hardness ratio properties to previously identified CDFS sources.

Selecting only sources with spectroscopic/photometric redshift information and with number of counts larger than 100 (pn detector), we create a representative sample of 127 X-ray sources (AGN and galaxies) over a wide range of redshifts and luminosities. We performed detailed source-by-source X-ray spectral analysis with different models in order to investigate the complexity of AGN spectra (e.g. soft excess, iron line, absorption edge etc). We observe a separation between so-called type-1 and the type-2 AGN as a consequence of different absorption column densities. More than 90% of the source spectra are in agreement with the so-called 'Unified model', which postulates that the optical and X-ray characteristics of AGN are determined by purely

geometrical conditions (specifically, the point of view on the accretion disc and its surrounding dust torus). However a fraction of 'atypical' sources (absorbed type-1 AGN and unabsorbed type-2 AGN) was also discovered. Most of these 'atypical' objects have good signal-to-noise ratio which does not allow us to ascribe these properties to the poor spectra quality. The observed mismatch between X-ray and optical properties may be explained by the difference in the physical conditions surrounding the emission regions. Most AGN spectra required only an (un)absorbed power law model, however we detect a fraction of sources with additional spectral components such as a soft excess (11 sources) and an iron line (7 sources). No obvious correlation between spectral continuum and absorption or between Γ, $N_{\rm H}$ and redshift are found. The comparison between Chandra and XMM-Newton fitting strategy reveals that there is a strong dependence between the obtained spectral slope and absorption in the selected energy range for spectral fitting. As a result, for sources exhibiting low intrinsic absorption Chandra, due to the limited energy range, obtained systematically higher values of the absorption columns and consequently flatter power law slopes. We also confirm a progressive hardening for the combined integrated spectra for faint objects, which at first was noted in the Chandra analysis of CDFS. Using the staking procedure to obtain integrated spectra for faint objects combined in groups by flux, we detected a clear evolution of decrease of $\langle\Gamma\rangle$ with decreasing flux in the hard 2–10 keV band. However, the detailed comparison of $\langle\Gamma\rangle$ values shows that the spectral slopes determined from XMM-Newton data are steeper typically by 0.1 than these detected by Chandra, even if exactly the same energy range (1–7 keV) is used by both instruments. The discrepancy becomes even larger if the soft 0.3–1 keV energy range is included in the fitting. For the first time derived integrated spectrum of the most distant type-2 QSO shows a strong X-ray absorption with a clear soft component (fitted with a scattering/partial covering model), implying that for the average distant ($z > 2.5$) type-2 QSOs this component is required. The general X-ray properties of the average high-z type-2 QSO spectrum is comparable to that of the highly absorbed sources in the local universe.

Using the 770 ksec XMM-Newton survey of the Lockman Hole field in combination with extensive optical identifications of the AGN population, we applied an alternative approach for studying iron line contribution to the XRB AGN spectra. Using the sample of 104 sources we derive average rest-frame spectra of type-1 and type-2 AGN. The most prominent feature in the obtained representative spectra is a strong fluorescent Fe line at rest-frame energy $\sim$ 6.4 keV. In both type-1 and type-2 AGN, a clear relativistic line profile is revealed, however the spectrum for the type-2 AGN indicates in addition to the broad line a narrow component. Modelling with different line models shows that a Laor line profile (i.e. rotating Kerr black hole) with an inner disk radius smaller than the last stable orbit of a Schwarzschild black hole gives the physical most consistent interpretation, indicating that the average supermassive black hole has significant spin. However, the statistical quality of the data does not rule out a Schwarzschild black hole with the entire emission comming from the last stable orbit. Equivalent widths of the broad relativistic lines range between 400–600 eV. We used the disk reflection model to compare the observed strength of the line with the

amplitude of the reflection component, concluding that to consistently describe the observations the average iron abundance should be about three times the solar value. This result implies that the presence of a strong, relativistic iron line in rest-frame spectra of the XRB sources is possibly due to a high metallicity in the average population. This conclusion has also been confirmed by the near-Infrared spectroscopical studies of a sample of high-redshift luminous quasars.

Most of the work discussed in this dissertation has been published in refereed journals and conference proceedings.

Chapter 2 and **3** are partly based on:

X-ray spectral properties of AGN in the Chandra Deep Field South, P. Tozzi, R. Gilli, V. Mainieri, C. Norman, G., Risaliti, P. Rosati, J. Bergeron, S. Borgani, R. Giacconi, G., Hasinger, M. Nonino, A. Streblyanska, G. Szokoly, J.X. Wang, W. Zheng, 2005, A&A, submitted

Spectral properties from XMM-Newton observation of Chandra Deep Field South sources, A. Streblyanska, J. Bergeron, H. Brunner, A. Finoguenov, G. Hasinger, V. Mainieri, 2005, Issue IAUS230, Cambridge University Press (proceedings of the International Astronomical Union)

Probing the X-ray Universe: Analysis of faint sources with XMM-Newton, A. Streblyanska, G. Hasinger, X. Barcons, H. Brunner, A. C. Fabian, A. Finoguenov and S. Mateos, 2005, MPE Report 288 (proceedings of the EPIC-XMM-Newton Consortium Meeting '5 Years of Science with XMM-Newton')

XMM-Newton observation of the Chandra Deep Field-South: statistical treatment of faint source spectra, A. Streblyanska, J. Bergeron, H. Brunner, A. Finoguenov, G. Hasinger, V. Mainieri, 2004, Nuclear Physics B (Proc. Suppl.) 132, 232 (proceedings of the Second BeppoSAX Symposium 'The Restless High-Energy Universe').

Chapter 4 is mostly based on:

XMM-Newton observations of the Lockman Hole: III. A relativistic Fe line in the mean X-ray spectra of type-1 and type-2 AGN, A. Streblyanska, G. Hasinger, A. Finoguenov, X. Barcons, S. Mateos and A. C. Fabian, 2005, A&A 432, 395

XMM-Newton observations of the Lockman Hole IV: spectra of the brightest AGNs, S. Mateos, X. Barcons, F. S. Carrera, M. T. Ceballos, G. Hasinger, I. Lehmann, A. C. Fabian and A. Streblyanska. 2005, A&A, 444, 79.

Zusammenfassung

In dieser Arbeit wurden die tiefsten, mit XMM-Newton durchgeführten Durchmusterungen im "Chandra Deep Field South" (CDFS) und im "Lockman Hole" (LH) analysiert. Diese beiden Referenzfelder für das Studium der verschiedenen, zur Röntgenhintergrundstrahlung beitragenden Objektklassen bieten einzigartige Möglichkeiten, physikalische Eigenschaften und die kosmologische Evolution von weit entfernten aktiven und normalen Galaxien, Galaxienhaufen und sogar schwachen Sternen in unserer Milchstraße mit Hilfe statistisch signifikanter Stichproben zu untersuchen. Das Hauptziel der Arbeit war eine verbesserte Beschreibung der Röntgeneigenschaften von aktiven Galaxien (AGN) in kosmologischen Entfernungen mit Hilfe statistischer Analysen großer Stichproben. Die Hauptergebnisse der Arbeit werden hier zusammengefasst.

In der 370 ksec langen XMM-Newton Beobachtung des CDFS wurden insgesamt 363 Röntgenquellen entdeckt. Die daraus abgeleiteten log N–log S Relationen stimmen mit den Ergebnissen der 1 Msec Chandra Beobachtung überein. Die kumulativen Flächendichten der Röntgenquellen haben im sehr "harten" Energieband (5–10 keV) eine deutlich steilere Abhängigkeit vom Quellfluss, als im "weichen" (0.5–2 keV) oder "harten" (2–10 keV) Band. Die meisten, zu diesem sehr harten Band beitragenden Röntgenquellen sollten stark absorbierte AGN bei relativ niedrigen Rotverschiebungen sein. Ein Vergleich der XMM-Newton Quellen mit zwei unabhängigen, tiefen Chandra Beobachtungen ergibt eine exzellente Übereinstimmung der Positionen ($\sim$2 sec), ein Hinweis darauf, dass die XMM-Newton Daten nicht signifikant unter Quellkonfusion leiden. Die abgeleiteten Quellflüsse zeigen eine vernünftige Übereinstimmung; für Quellen bei niedrigen Flüssen im harten Band gibt es jedoch eine erhebliche Streuung, die auf zeitliche Variabilität hindeutet. Im XMM-Newton Feld haben wir insgesamt 15 ausgedehnte Quellen entdeckt und damit mit die höchste Flächendichte ausgedehnter Quellen im Röntgenbereich. Sieben dieser Quellen waren bereits aus den früheren tiefen Chandra-Beobachtungen bekannt und konnten mit Galaxien bzw. Gruppen und Galaxienhaufen identifiziert werden. Unsere vorläufige Analyse der Röntgenspektren dieser Objekte zeigt, dass die Röntgenleuchtkräfte (10^{41-43} erg/s) und Temperaturen (kT $<$ 3 keV) gut mit früheren Ergebnissen bei helleren Objekten übereinstimmen. Für die 165 neuen, von XMM-Newton entdeckten Objekte fanden wir anhand von Zweifarben-Diagrammen und Farb-Helligkeits-Diagrammen ähnliche Spektralverteilungen wie bei den bisher bekannten CDFS-Quellen.

Durch eine Auswahl von Quellen mit spektroskopischen oder photometrischen Rotverschiebungen und mit mehr als 100 Quellphotonen im pn-CCD-Detektor konnten wir eine repräsentative Stichprobe von 127 AGN über einen weiten Bereich von Rotverschiebungen und Leuchtkräften definieren. Für diese Quellen führten wir detaillierte Spektralanalysen mit verschiedenen Modellen durch, um die Komplexität von AGN-Spektran (z.B. weiche Exzesse, Eisen-Linien, Absorptionskanten etc.) statistisch zu erfassen. Wir fanden einen Unterschied zwischen so genannten Typ-1 und Typ-2 AGN aufgrund ihrer verschiedenen intrinsischen Absorptions-Säulendichten. Mehr als 90% der Quellen folgen danach dem so genannten "Unified Model", nach dem die optischen und Röntgeneigenschaften von AGN durch rein geometrische Bedingungen (im wesentlichen dem Blickwinkel auf die Akkretionsscheibe und den sie umgebenden

Staubtorus) miteinander verknüpft sind. Wir fanden jedoch auch einen kleinen Anteil atypischer Quellen (absorbierte Typ-1 Quellen und unabsorbierte Typ-2 Quellen). Die meisten dieser atypischen Quellen haben ein gutes Signal-zu-Rausch-Verhältnis, so dass dieses Ergebnis nicht mit einer schlechten Qualität der Spektren zu erklären ist. Die beobachteten Abweichungen vom "Unified Model" müssten deshalb mit unterschiedlichen physikalischen Bedingungen in der Umgebung der Emissionsregion erklärt werden. Die meisten AGN-Spektren benötigen nur ein einfaches un-absorbiertes oder absorbiertes Potenzgesetz als beste Anpassung. Bei einem kleinen Teil der Spektren benötigen wir jedoch zusätzliche Spektrale Komponenten, wie zum Beispiel einen weichen Exzess (11 Quellen) oder eine Eisen-Linie (7 Quellen). Wir finden keine Korrelation zwischen der Steigung des Kontinuums und der Absorption oder der Rotverschiebung. Der Vergleich zwischen den Fits mit Chandra und XMM-Newton zeigt eine systematische Abhängigkeit zwischen der Steigung des Spektrums und der Absorption. Chandra, mit seiner kleineren Bandbreite in der Energie, findet für Quellen mit niedriger Absorption systematisch höhere Absorptionswerte und flachere Spektralindices als XMM-Newton. Aus den XMM-Newton-Beobachtungen bestätigt sich ein progressives Abflachen der kombinierten Spektren als Funktion des beobachteten Flusses, das ursprünglich in den Chandra-Daten des CDFS entdeckt wurde. Die detaillierten Spektralindices stimmen zwischen Chandra und XMM-Newton aber nicht überein, XMM-Newton findet typischerweise um etwa den Wert 0.1 steilere Spektren als Chandra, auch wenn der gleiche Energiebereich (1–7 keV) benutzt wird. Die Diskrepanz wird noch größer, wenn der Energiebereich 0.3–10 keV herangezogen wird. Dies lässt auf eine positive Krümmung im gemittelten Spektrum der Hintergrundsquellen schlieen. Zum ersten Mal haben wir ein mittleres Spektrum der Typ-2 Quasare abgeleitet, das auf eine starke intrinsische Absorption zusammen mit einer deutlichen weichen Komponente (interpretiert mit einem Reflektionsmodell oder einem "Partial Covering" Absorber) schließen lässt. Das mittlere Spektrum der Typ-2 Quasare bei Rotverschiebungen $z>2.5$ ist deshalb vergleichbar mit dem der am höchsten absorbierten Quellen im lokalen Universum.

Mit Hilfe der 770 ksec XMM-Newton Durchmusterung im Lockman-Feld, zusammen mit den bereits existierenden, extensiven optischen Identifikationen der AGN-Population haben wir einen alternativen Ansatz zur Untersuchung des Beitrags der Eisenlinien zu den Spektren der AGN des Röntgenhintergrundes entwickelt. Für eine Stichprobe von 104 Quellen haben wir die mittleren Spektren im Ruhesystem von Typ-1 und Typ-2 AGN bestimmt. Die prominenteste Struktur in diesen mittleren Spektren ist eine starke fluoreszente Eisenlinie bei einer Ruheenergie von etwa 6.4 keV. Sowohl Typ-1 als auch Typ-2 Quellen zeigen deutlich ein relativistisch verbreitertes, asymmetrisches Linienprofil, wobei sich im Profil der Typ-2 AGN noch eine zusätzliche Schmale Emissionslinie andeutet. Anpassungen mit verschiedenen Modellen für die Linie zeigen, dass ein Laor-Modell (für ein maximal rotierendes Kerr-Loch) mit einem inneren Radius der Scheibe der kleiner ist, als der letzte stabile Orbit eines nichtrotierenden Schwarzschild-Loches, die physikalisch konsistenteste Beschreibung liefert, ein Hinweis darauf, dass das mittlere super-massereiche Schwarze Loch im Universum signifikanten Spin trägt. Die statistische Qualität der Daten schließt allerdings nicht

ein Schwarzschild-Loch aus, bei dem die gesamte Emission vom letzten stabilen Orbit kommt. Die Äquivalentbreiten der relativistisch verbreiterten Eisenlinien sind mit 400–600 eV erstaunlich hoch. Mit Hilfe eines relativistisch verbreiterten, selbstkonsitenten Reflektionsmodells der Akkretionsscheibe konnten wir die beobachtete Stärke der Fluoreszenzlinie mit der Amplitude der Compton-Reflektion von der Scheibe vergleicchen und folgern, dass für eine konsistente Beschreibung der Daten eine Eisenhäufigkeit notwendig ist, die etwa der dreifachen solaren Häufigkeit entspricht. Dieses Ergebnis weist darauf hin, dass die Stärke der relativistischen Linie in den mittleren Spektren der Population der Hintergrundsquellen wahrscheinlich mit einer erhöhten Metallhäufigkeit der mittleren Quellpopulation zusammenhängt. Ähnliche Ergebnisse wurden auch aus optischen Spektren leuchtkräftiger Quasare gefunden.

Ein Großteil der hier dargestellten Ergebnisse wurde bereits in referierten Zeitschriften oder Konferenzbeiträgen veröffentlicht.

Acknowledgments

First of all, I wish to thank my advisor, Prof. Günther Hasinger for giving me the opportunity to work on such a fascinating topic and for supervising me over three years of my PhD. I am also very grateful to him for providing a significant help and guidance during the writing of this thesis. I am really grateful for him that he choose me as his PhD student and I hope that did not regret this.

I am grateful to Prof. Ralf Bender for agreeing to be my LMU affiliated supervisor and to Prof. Hans Böhringer for being my second referee.

I would also like to thank Alexis Finoguenov, who was for me a second supervisor, provided me with a lot of advice and help with the spectral analysis.

Many thanks to all the members of our X-ray group for their help and enthusiasm over the years. In particular, I am grateful to Hermann Brunner and Vincenzo Mainieri for their help with the source reduction and for providing the necessary programs, to Thomas Boller for his advice about the 'iron line stuff' and to Zdenka Misanovic for her invaluable help, in particular with the English.

I am especially grateful to my family, my mother, my cousin Vita and my fiance Alexey. Their support and love was very important for me during my PhD.

Finally, I wish to thank all the friends that helped and supported me in my private and scientific live in the last three years, to people who have made living in München pleasurable and the nicest years in my life: Zdenka, Yu-Ying, Katya, Dima, Tanya, Paolo, Linda, Dorina, Alexey and many others (the list is long, but I really remember all of you).

Thanks to all people in the MPE and outside for sharing with me a good time during my PhD.

Contents

List of Figures xiv

List of Tables xv

1 Introduction 1
1.1 X-ray Background . . . 1
1.2 Basic principles of the AGN phenomenon . . . 4
1.2.1 Unified model and types of AGN . . . 5
1.3 XRB source populations . . . 8
1.3.1 Optical and X-ray classifications . . . 11
1.3.2 Redshift distributions . . . 13
1.3.3 Evolution of AGN and SMBH . . . 13
1.4 The X-ray spectra of AGN . . . 15
1.4.1 Iron line . . . 20
1.4.2 Fe line and XRB . . . 24
1.5 The two deep XMM-Newton surveys . . . 24
1.5.1 The Chandra Deep Field South Field . . . 25
1.5.2 Optical identification in the CDFS . . . 26
1.5.3 The Lockman Hole Field . . . 27
1.6 XMM-Newton observatory . . . 28
1.7 Outline of this dissertation . . . 29

2 The Chandra Deep Field South 31
2.1 XMM-Newton observations . . . 31
2.2 X-ray source list . . . 32
2.2.1 Comparison between source catalogs from Chandra and XMM-Newton . . . 35
2.2.2 Extended sources . . . 36
2.2.3 New XMM-Newton sources . . . 39
2.3 X-ray colour-colour diagrams . . . 41
2.4 Conclusions . . . 44

3 Analysis of source spectra in the CDFS 49
3.1 Introduction . . . 49
3.2 X-ray sample and spectra extraction . . . 49

3.3 Spectral analysis and models . . . 53
3.4 Spectral parameters . . . 55
3.4.1 Photon index . . . 56
3.4.2 X-ray absorption . . . 57
3.4.3 Dependence of Γ and N_H on the flux, luminosity and redshift . . 61
3.4.4 Fe line . . . 65
3.4.5 Soft excess . . . 66
3.4.6 Representative X-ray spectra . . . 68
3.5 X-ray stacking analysis . . . 68
3.5.1 Type-2 QSOs . . . 70
3.5.2 Spectral index as a function of flux . . . 74
3.5.3 Spectral properties of the unresolved Cosmic X-ray background 76
3.6 Comparison between XMM and Chandra . . . 77
3.6.1 Type-1 AGN . . . 80
3.6.2 Type-2 AGN . . . 81
3.6.3 Galaxies and low-luminosity AGN . . . 82
3.6.4 Brief summary from the comparison . . . 82
3.7 Conclusions . . . 83

4 A relativistic Fe line in the mean X-ray spectra of type-1 and type-2 AGN 88
4.1 Introduction . . . 88
4.2 Observations and data reduction . . . 89
4.3 X-ray sample . . . 90
4.4 Spectral analysis . . . 91
4.4.1 Origin of the broad line feature in the type-1 AGN spectrum . . 93
4.4.2 Fe line in type-2 AGN . . . 97
4.5 Discussion . . . 97
4.6 Conclusions . . . 99

5 Conclusions 101
5.1 Statistical properties of Chandra Deep Field South sources . . . 101
5.2 Spectral analysis of individual sources and statistical treatment of background AGN population . . . 102
5.3 The iron line feature in the mean rest-frame spectra of type-1 and type-2 AGN . . . 103
5.4 Discussion and Future work . . . 104

Bibliography 106

List of Figures

1.1 The cosmic energy density spectrum 2
1.2 A unified AGN model 6
1.3 AGN contributions to the XRB 9
1.4 A type-1 AGN X-ray spectrum and reflection of an incident power-law spectrum off cold gas 17
1.5 The profile of the Fe K_α disc line 21
1.6 The dependence of the line profile on the observed inclination 22
1.7 Observed iron K_α line from MCG-6-30-15 23
1.8 The composite raw photon image of the CDFS and LH from XMM-Newton survey 25

2.1 The 0.5-10 keV image of the CDFS with overplotted positions of X-ray sources 33
2.2 Effective survey area in each energy band as a function of flux 34
2.3 Log N–Log S distribution 34
2.4 Comparison between Chandra and XMM X-ray fluxes in both the soft and hard bands 37
2.5 Example of group spectrum 38
2.6 Comparison between XMM-Newton and E-CDFS X-ray fluxes in both the soft and hard bands 40
2.7 The X-ray colour-colour diagram 42
2.8 X-ray colour-flux diagram 43
2.9 The two representative unfolded model spectra of the new XMM sources 45

3.1 Distribution of pn+MOS counts for our sample 50
3.2 The redshift distribution 51
3.3 The source and background spectra 52
3.4 Histograms of 0.2–10 keV fluxes for the 127 sources 54
3.5 X-ray fluxes from count rate vs. fluxes derived from the best fit model . 55
3.6 The $N_{\rm H}$ distribution 57
3.7 The rest-frame photon index versus absorption 60
3.8 Dependence of $N_{\rm H}$ with the soft and hard fluxes 62
3.9 Unabsorbed rest-frame $L_{\rm X}$ vs the detected $N_{\rm H}$ 62
3.10 Spectral slope Γ vs unabsorbed hard rest-frame $L_{\rm X}$ 63
3.11 Spectral slopes Γ and absorption $N_{\rm H}$ as a function of redshift 63

3.12 The total L_X as a function of redshift 64
3.13 An example of a spectrum with the detected Fe K_α line 66
3.14 The unfolded spectra of the sources with the detected soft component . 67
3.15 Representative X-ray spectra 69
3.16 Integrated X-ray spectrum for the distant type-2 QSOs 70
3.17 The mask region files for the stacked spectra by flux 72
3.18 The average power law indices of the stacked spectra of different flux subsamples 73
3.19 The spectrum of the unresolved X-ray background in the CDFS 76
3.20 Comparisons between XMM-Newton and Chandra fluxes 78
3.21 Comparisons between XMM-Newton and Chandra values for Γ and N_H 79
3.22 The power law slope distributions for XMM and Chandra samples . . . 79
3.23 The dependence between the power law slope values and the observed column densities 80
3.24 Comparison between XMM-Newton and Chandra values for unabsorbed luminosities in the two bands 81
3.25 An example of high-z BLAGN 82

4.1 Redshift distribution of the LH X-ray sources in our selected sample. . 90
4.2 The mean ratio plots from type-1 and type-2 AGN spectra. 92
4.3 The ratio plots from mean unfolded type-1 AGN spectra. 94
4.4 The ratio plots from mean unfolded type-2 AGN spectra. 94
4.5 The unfolded laor stacked spectra representative of the type-1 and type-2 AGN. 96

List of Tables

2.1 ECF for different energy bands and different photon indices 35
2.2 Extended sources 39
2.3 X-ray catalogue of the new XMM-Newton sources 46
2.3 Continued 47
2.3 Continued 48

3.1 Best fit parameters for 127 sources 85
3.1 Continued 86
3.1 Continued 87

4.1 Results of the spectral fitting using three line models for mean spectra of type-1 and type-2 AGN 95

Chapter 1

Introduction

The detailed investigation of the physical properties of Active Galactic Nuclei over a wide range of redshifts could provide useful information about the formation of supermassive black holes and AGN evolution in comparison with the evolution of normal galaxies. The best energy range for such studies is the X-ray band which is dominated by accretion processes, in particular, the X-ray background which is built up from individual objects at different redshifts and with different physical properties. Therefore, resolving the X-ray background into discrete sources and understanding their physical properties is crucial for forming our knowledge about the nature of the AGN and galaxy populations in the Universe. In this introduction I will briefly describe the physics and astronomy background which are most relevant to the work presented in this dissertation. In-depth reviews of the topics of the X-ray background and deep X-ray surveys can be found in Fabian & Barcons (1992), Gilli (2004), Brandt & Hasinger (2005), Brandt et al. (2005), as well as numerous broader reviews about the AGN phenomenon (e.g. Rees 1984, Peterson 1997) and fluorescent iron lines (Fabian et al. 2000, Reynolds & Nowak 2003, Fabian & Miniutti 2005).

1.1 X-ray Background

The cosmic X-ray background (XRB) extends from $\sim$0.1 to several hundred keV. Nowadays, we know that at the lowest energies ($<$0.9 keV) the dominant contribution is the diffuse thermal emission from hot gas in the local bubble, Galactic halo component and Warm–Hot Intergalactic Medium (WHIM; Sołtan 2005); the purely extragalactic component has been determined by shadowing experiments (Warwick & Roberts 1998). The spectrum reaches a peak intensity at $\sim$30 keV before decreasing exponentially at higher energies. It is now clear that at energies above $\sim$0.5 keV the background is made up of the summed emission from point sources, principally active galactic nuclei (AGN) along with some contribution at soft X-ray energies from thermal emission of galaxy clusters and stellar processes in normal galaxies. The XRB is one of the components of the total extragalactic background radiation, which represents all radiation processes in the Universe, integrated over cosmic time. Fig. 1.1 shows a compilation of recent determination of the cosmic energy density spectrum from radio

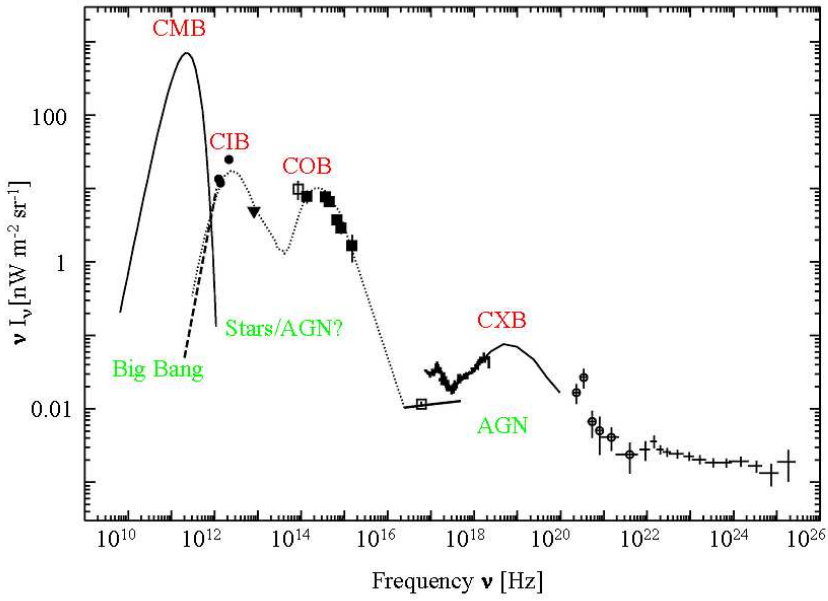

Figure 1.1: The cosmic energy density spectrum from radio to gamma bands in a νI_ν representation, where a horizontal line corresponds to equal radiation power per decade of energy. The four distinct components can be identified: the Cosmic Microwave Background (CMB), the Cosmic Far-Infrared Background (CIB), Cosmic Optical/UV Background (COB) and the Cosmic X-ray/Gamma-ray Background (CXB). The energy spectrum of the CXB has a characteristic hump at $\sim$ 30 keV and a long tail towards higher energies. The dotted line shows one of models in Dwek et al. (1998) extrapolated from the visual to the EUV range. Taken from Hasinger (2000).

to gamma rays (Hasinger 2000). Apart from the XRB, the extragalactic background light seems to be dominated by two distinct humps, one in the optical/near-infrared range (COB; has been resolved into discrete sources by the Hubble Space Telescope Deep Field images), and another one in the FIR/sub-mm range (CIB; most likely produced by dust emission in distant galaxies). The dust peak contains comparable (or even more) energy than the stellar peak, which indicates that a large amount of light in the early universe had to be absorbed by dust.

The X-ray background has been a matter of intense study since its discovery by Giacconi et al. (1962) during the first successful rocket launched to study the X-ray emission from the Moon. The XRB, the first cosmic background, which had been discovered, appears as a residual diffuse emission of approximately constant intensity from all directions observed during the flight. The lack of any correlation with the galactic latitude, and dipole anisotropy consistent with that of the dipole component of the Cosmic Microwave Background (CMB; Shafer & Fabian 1983) strongly argued

from the beginning in favour of a cosmological origin of this extragalactic background radiation.

The first broad-band spectrum measured by the HEAO-1 satellite (Marshall et al. 1980) is very well fitted by a 40 keV thin thermal bremsstrahlung model and is well described by a power-law spectral function ($F(E) \propto E^{-\Gamma}$) with photon index $\Gamma \sim 1.4$ from 3 up to $\sim$15 keV. On the other hand, the interpretation of XRB as a sum of discrete objects (AGN) requires the contribution from a larger number of sources ($N > 10^6$ sr^{-1}; Schwartz 1980). It was therefore quite natural to hypothesize the presence of a truly diffuse hot Inter Galactic Medium (IGM) with a characteristic temperature of $kT = 40(1 + z)$ keV, as was originally proposed by Field & Perrenod (1977).

This first explanation of the origin of the XRB has been then entirely discarded with results from first high angular resolution X-ray telescopes, which reveal the discrete nature of the CXRB. In addition, the results from the COBE satellite (Mather et al. 1990) show no evidence of the high-frequency distortions in the cosmic microwave background through inverse-Compton scattering, which should arise from a hot (T $\geq 10^8$ K) IGM. As a consequence, the only viable alternative for the XRB origin remained the superposition of discrete sources, and the most likely candidates appeared immediately to be AGN, particularly since pointed observations of previously known AGN show that they are luminous X-ray objects.

Since the early years of the Einstein observatory (e.g. Maccacaro et al. 1991) a significant fraction of the XRB has been resolved into discrete objects. Most ($\sim$70–80%) of the 0.5–2 keV background was resolved into point sources by ROSAT (Hasinger et al. 1998), a large fraction of which were identified, through extensive optical follow-up, as AGN (e.g. Schmidt et al. 1998, Zamorani et al. 1999, Lehmann et al. 2001). Therefore it was widely accepted that the XRB, at least in the soft 0.5–2 keV band, is largely due to the accretion onto supermassive black holes, integrated over cosmic time. In comparison with the soft band, progress at harder energies (>2 keV) has required the improved sensitivity and spatial resolution of the Chandra and XMM-Newton observatories. Before these two observatories were launched, the fraction of the resolved hard XRB was very low. Due to the limited angular resolution of the ASCA satellite, its medium-to-deep surveys resolved only $\approx$35% of the 2–10 keV XRB (Gendreau, Barcons & Fabian 1998). In the hardest 5–10 keV band 20–30% of the XRB has been resolved with the Beppo-SAX mission (e.g. Comastri et al. 2001).

The first deep X-ray survey conducted by XMM-Newton in the Lockman Hole field reached a limiting flux of $\sim 3 \times 10^{-15}$ erg cm^{-2} s^{-1} and was able to resolve some $\sim$60% of the 5–10 keV background (Hasinger et al. 2001). The two Chandra Deep Fields, North and South, probe down to $\sim$1.4–2.8 $\times 10^{-16}$ erg cm^{-2} s^{-1} over the 2–8 keV band and resolve $\sim$70–90% of the background in this broad, hard band (Giacconi et al. 2002, Moretti et al. 2002, Alexander et al. 2003, and references therein). Finally, Worsley et al. (2005), using results from all existing deep fields with Chandra and XMM-Newton, shows that while $\sim$85% and $\sim$80% were resolved in the broad 0.5–2 and 2–10 keV bands (depending on XRB normalization[1]) into discrete objects, only

[1]The remaining uncertainty in the resolved fraction attributed to deviations in the absolute value

$\sim$60% and $\sim$50% are resolved above 6 keV and 8 keV, respectively. Even if the 100% resolution into individual objects is not expected, since a small portion of the XRB could be due to truly diffuse emission (3–4% in soft and $\sim$1% in the hard bands; Sołtan 2003), the low fraction of the resolved background at the hard band unambiguously indicates the presence of a source population that could not be detected in current surveys. In the 10–100 keV band, where most of the XRB energy density resides, only a 3% of the background has been resolved (e.g. Krivonos et al. 2005).

Since resolving the XRB into individual sources is crucial to understanding the nature of the AGN populations in the Universe, an important question immediately arise: what is the nature of the missing source population? Before discussing this, I describe the nature of already resolved and identified XRB sources, which are mainly AGN.

1.2 Basic principles of the AGN phenomenon

In the central regions of many galaxies we can observe and study a natural phenomenon known as active galactic nuclei. The small spatially unresolved core of such objects can emit energy comparable or sometimes even larger than the total luminosity of the whole host galaxy. The emission is spread widely across the electromagnetic spectrum and cannot be ascribed to the integrated emission from stars (as it is possible for normal galaxies). In addition, the emission of some AGN appears to be variable on time scale of years, hours and even minutes, which implies as an emitting region a small volume of space, comparable with the size of the Earth's orbit around the Sun. The most favoured explanation for such a scenario is a supermassive black hole (SMBH) which lies at the center of the galaxy (e.g. Rees 1984). The high mass of the black hole (BH) of $\sim 10^7$–10^9 $M_\odot$ is the necessary attribute of this interpretation due to the high luminosity of most AGN.

Although accretion of gas and dust onto SMBH has been accepted as the explanation of AGN emission, obtaining unambiguous proof has been difficult, due to the lack of direct observational evidence. However, over the past years, indirect confirmation of the presence of a BH has been obtained in the optical, infrared, X-ray and radio bands. Optical studies of gas and dust kinematics of nearby galaxies, radio observations of collimated outflows at relativistic speeds and detection of water masers in the nucleus of NGC 4258, and the X-ray studies of enormous Doppler shifts and gravitational redshifts of the Fe emission line have been considered to be unambiguous signatures of the BH presence.

Recent data confirm the theoretical idea that a supermassive BH is present in most normal, non-active galaxies, as well. The most spectacular arguments supporting the SMBH theory come naturally from the centre of our own Milky Way (e.g. Genzel et al. 1997, Schödel et al. 2002). The ten years of high-resolution astrometric imaging has allowed to trace several stars orbits, in particular the two-thirds of the orbit of the

of the XRB itself due to cosmic variance (e.g. Gilli et al. 2003, Yang et al. 2003) and significant instrumental cross-calibration uncertainties (e.g. De Luca & Molendi 2004 and references therein).

star currently closest to the compact radio source (and a massive black-hole candidate) Sagittarius A*. The observations show that the star is on a bound, highly elliptical keplerian orbit around Sgr A*, with an orbital period of 15.2 years and a pericentre distance of only 17 light hours. The orbit with the best fit to the observations requires a central point mass of (3.7± 1.5) 10^6 $M_\odot$, which is the most accurate measurement of the BH mass up to-date. It is also possible to detect the presence of a BH in other galaxies with no signature of nuclear activity by studying their central stellar or gas kinematics (e.g. Magorrian et al. 1998).

1.2.1 Unified model and types of AGN

AGN have been classified in many ways, however, from the general point of view, which is widely accepted now, AGN can be separated into two broad categories: type-1 AGN (unabsorbed sources) and type-2 AGN (absorbed sources). Both of these types contain Seyferts[2] (with modest luminosities, but the best studied since they are generally quite nearby) and quasars (more luminous and more distant than Seyferts; 10% of quasars are radio-loud), and can be separated using their optical line widths (Osterbrock 1989). Type-1 exhibit broad emission lines, particularly hydrogen, that are attributed to ionised gas in the 'broad-line region' (BLR) within 0.1 pc of the central massive BH, whereas the spectra of type-2 AGN only show narrow emission lines, believed to originate from a much larger 'narrow-line region' (NLR) around the core (∼100 pc).

However, the detection of broad optical lines in the polarised, scattered component of the Seyfert 2 galaxy NGC 1068 (Antonucci & Miller 1985), clearly shows that type-2 AGN are only obscured versions of the first type. This and other similar observations led to a *unified model* for radio-quiet[3] AGN (Antonucci 1993), in which type-1 and type-2 AGN objects are intrinsically the same sources observed through different degrees of line-of-sight and therefore exhibit different absorption values.

The unified model for AGN (see Fig. 1.2) has a SMBH as its central power source. The SMBH is surrounded by an accretion disc produced by the matter that is transformed into radiation via accretion onto the hole at the Schwarzchild radius R_s (for 10^8 $M_\odot$ black hole, $R_s \approx 2$ astronomical units or 10^{-5} pc). The following two phenomena can coincide with the accretion disc: 1) the plasma jets produced by the winding up of magnetic fields and 2) the region with clouds of highly ionised gas with $T<10^4$ K and a density in the range of 10^6–10^{11} cm^{-3}, observed as BLR. This region is physically close to the BH and located at the distance of 20–30 light days (the result from reverberation mapping, e.g. Peterson et al. 1998).

The nucleus is surrounded by a thick dusty torus, which radiates predominantly in the infrared, and obscures our view of the BLR directly. This torus blocks ionizing photons from reaching the NLR in some directions, hence explaining the cone-shaped

[2]The official magnitude cutoff (using absolute B-band magnitude) is $M_B > -21.5 + 5log h_0$ for Seyferts; the more luminous objects are called quasars.

[3]Loudness (R) is defined by the flux ratio at 4.85 GHz and 4400 Å(rest-frame). Radio-quiet objects have R< 10. Most AGN from deep surveys are radio quiet.

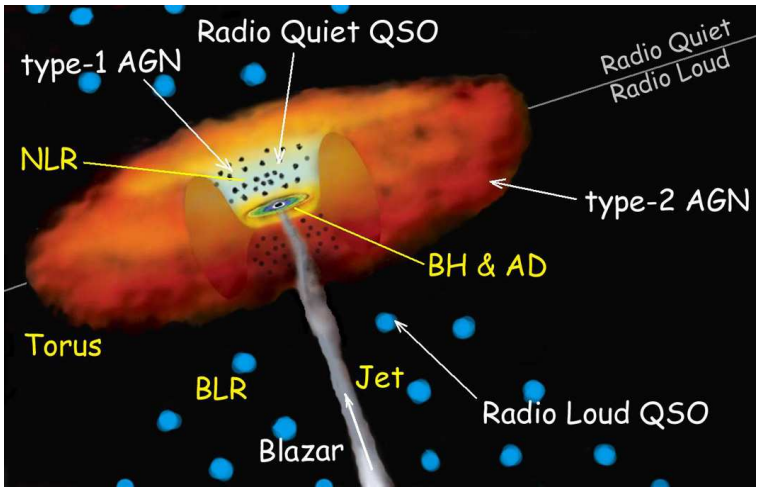

Figure 1.2: A schematic representation of the unified model of AGN. In the type-1 AGN (Seyferts and QSOs) we can see directly into the central regions. As a result, we observe both broad and narrow lines in the optical spectrum, and the direct emission from the accretion disc (AD). The type-2 AGN appears then the whole system is viewed edge-on (i.e. along the plane of the molecular torus) and blocks the view of the BLR area. In addition, according to the unified model, we can distinguish between radio loud and radio quite objects by considering the orientation of the AGN with respect to the jet location. Blazars are special cases of unobscured (type 1) objects where we are looking face-on at the nucleus and directly into the jet. Matter in the jet is moving at relativistic velocities, so that the radiation it emits is beamed and can vary in very short periods of time. Due to the strong emission from the jet, we cannot observe spectral lines from BLR and NLR.

NLRs that are sometimes seen. Outside of the molecular torus and within the polar cones are clouds of interstellar material, which are ionised by the radiation flowing from the central AGN and not blocked by the torus. These clouds together with the surrounding gas produce the Narrow-Line Region. Out to approximately 1 kpc are areas of molecular gas and dust that orbit the nucleus. The detected emission appears extended and isotropic, which implies a low density in this region. In addition, within this area are central HII star formation regions, which are strong emitters in far infrared, and are associated with star-burst activity. The radio jets may become prominent and extend out to 1 Mpc, which is far beyond the optical size of the galaxy ($\sim$50 pc).

In the unified scheme, the orientation of the molecular torus (i.e. viewing angle) determines the classification of the source. The type-1 AGN appear to be unobscured, because our line-of-sight is along the axis of the torus directly through the center toward the nucleus; whereas, in the type-2 AGN, their higher hydrogen column densities of $N_{\rm H} \sim 10^{22}$–10^{24} cm^{-2} around the nucleus block our line of sight. The detailed studies show that these two classes are not distinct, but form a continuous distribution between the two extremes. Hence, a large number of intermediate classes have been introduced since the original definition.

The relative proportion of Seyfert 1s to Seyfert 2s is hard to measure because it is difficult to obtain unbiased samples; however, the estimates suggest that there may be 4–9 times more type-2 Seyferts than type-1 (Osterbrock & Shaw 1988). This implies that the opening angle of the torus must be rather narrow and the torus covers almost the entire sky (covering fraction ~ 0.7) as viewed from the vicinity of the black hole. It has been estimated that 85% of all the accretion power in the Universe has been absorbed. The absorbed energy would be re-emitted in the far-infrared, but high spatial resolution would be needed to avoid confusion with the emission from the star-forming regions.

Nowadays this model appears to be universal, and in its frame we can also explain other observed AGN classes such radio galaxies, which have different relative position to the jet. In radio-quiet AGN the radio emission is concentrated at the nucleus, but *radio-loud AGN* are distinguished by their long, collimated relativistic jets, which apparently are launched from within a few tens of Schwarzschild radii of the central BH. With the sub-arcsecond imaging capability of the Chandra observatory, jets have now been resolved in the X-ray band (e.g. Chartas et al. 2000), where they show sometimes slightly different morphology than in the radio (e.g. Wilson & Yang 2002). Like radio-quiet AGN, radio-loud galaxies can be unobscured (Broad line radio galaxies; BLRGs) and obscured (Narrow-line radio galaxies; NLRGs). Radio-loud AGN can also be classified by their jet-lobe morphology (Fanaroff & Riley 1974). Fanaroff-Riley type 1 (FR I) sources have bright, wide jets that disperse gradually into less intense lobe. FR II galaxies (more rare than the first type) have narrower, more collimated jets which are connected to edge-brightened lobes, often with noticeable hot spots. The two classes are found to depend on radio luminosity, so that objects with L_ν (1.4 GHz) $\leq 10^{25}$ W Hz^{-1} are FR Is (Fanaroff & Riley 1974). This dividing luminosity is dependent on the optical luminosity of the AGN and is roughly $\propto L_{opt}^2$ (Ledlow & Owen 1996). FR I galaxies are considered in the unified scheme to be the counterparts of BL Lac Objects[4], while FR II objects are parent class for radio-loud galaxies.

It is still not clear why some of the AGN are radio-loud and other are not, however it is known that the type of host galaxy in which they reside appears to be important: the spiral galaxies host radio-quiet AGN only, and radio-loud AGN are found only in elliptical host galaxies.

Of course, the unified model is very general and assumes some approximations about physical structure of suggested components, due to the fact that real observations of the SMBH and regions around are very difficult. For example, recent studies of Seyferts and quasars showed that the distance to the BLR and NLR scales with luminosity, as $R_{BLR} \propto L^{0.7}$ (Kaspi et al. 2000) and $R_{NLR} \propto L^{0.5}$ (Bennert et al. 2002), implying a larger size of these regions (up to ten times) for quasars then for less luminous Seyferts. Most resent studies of the sample of quasars (Netzer et al. 2004) show that NLR in high-luminosity (and high-redshift) objects must be physically different from the same region seen in the nearby objects.

[4] *Blazars* (BL Lac Objects and Optically-Violent Variables) show featureless spectra and highly variable; according to the unified model seen when our line-of-sight lies close to the direction of a jet, i.e. a polar view to the SMBH.

However, there is much observational evidence supporting the unified model and suggesting that it is correct, at least to the first order. For example, in the well-resolved cases, NLRs are sometimes cone-shaped, possible due to the fact that the ionizing radiation is roughly collimated before emerging into the NLR, perhaps due to an obscuring torus, or 'prebeaming' by the accretion disc or its atmosphere. It seems also, that the NLR in type-1 Seyfert appears smaller than that in type-2, which is consistent with projection effects expected from the standard orientation unification model. And one of the strongest supports comes from the X-ray studies, for example the discovery of large columns of X-ray absorbing gas in type-2 AGN (Awaki et al. 1991, Risaliti et al. 1999), and the lack of this absorbing material in type-1 AGN.

Recent observational results from deep/shallow surveys suggest there are also objects which cannot be explained in terms of the unified model of AGN (e.g. the substantial absorption for type-1 AGN and no absorption for type-2; see Section 3.4 for discussion). However, more observational evidences are needed to see how significant these results are for the unified model. We need large samples of AGN covering a wide range of redshifts and luminosities to investigate whether the unified model holds.

1.3 XRB source populations

In order to explain the observed XRB, several authors developed detailed XRB population-synthesis models, constructed within the framework of AGN unification scheme. The models were devoted to account for the spectral intensity of the XRB and to explain the X-ray source counts in the soft and hard energy bands (e.g. Setti & Woltjer 1989; Comastri et al. 1995; Gilli, Salvati & Hasinger 2001). In these models the XRB spectrum is explained as a mixed emission from obscured and unobscured AGN folded with an evolving luminosity function. One of the predictions from these models is a strong X-ray absorption for the sources optically classified as type-2 AGN, and moreover, that the fraction of the obscured objects is significantly larger.

The predictions of these models were confirmed by optical identifications of the sources detected in the hard X-ray fields. First, the optical identification of soft background sources resolved by ROSAT show that most of these sources are *unobscured* AGN with spectra that are too steep to account for the flat XRB in the same energy band. While XRB has Γ =1.4, the intrinsic continuum of almost all individual X-ray sources is approximated well by a power law with $\Gamma \simeq 1.8$ (Mushotzky 1984), suggesting that an additional population of either absorbed or flat spectrum sources is needed to make up the background at higher energies. The simulations show that if we observed an object with high intrinsic neutral hydrogen column density, this additional amount of obscuring matter along the line-of-sight will affect the observed spectrum in the way that the resulting X-ray spectrum will peak at higher energies (from a few keV up to $\geq$ 10 keV, depending on the $N_{\rm H}$). If we fit such a spectrum with an unabsorbed power law its spectral index will be flatter. Therefore, the elegant theoretical solution for the 'spectral paradox' is the assumption that the XRB is a superposition of the absorbed and unabsorbed sources with the same intrinsic steep

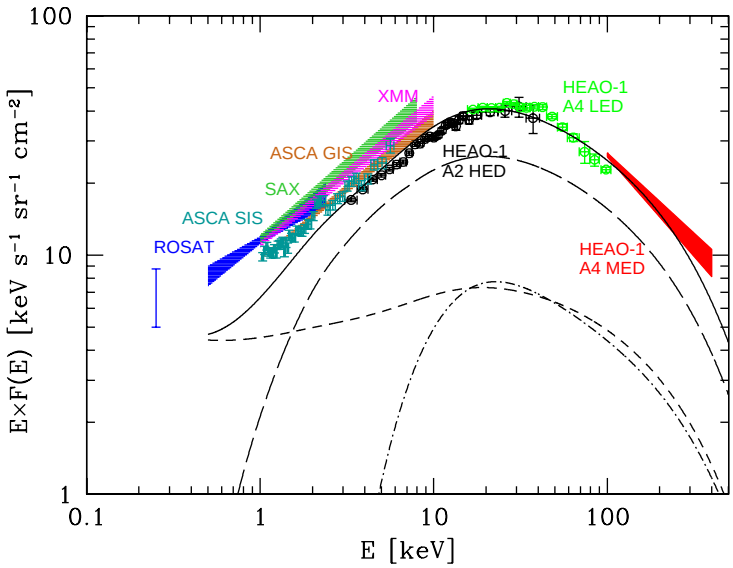

Figure 1.3: The AGN contribution (solid line) to the XRB spectral energy density as measured by different instruments (labeled). The contribution of unobscured ($N_{\rm H} < 10^{21}$ cm^{-2}, dashed line), Compton thin ($N_{\rm H} = 10^{21}$–10^{24} cm^{-2}, long-dashed line) and Compton thick ($N_{\rm H} > 10^{24}$ cm^{-2}, dot-dashed line) AGN is also shown. Figure taken from Comastri (2004).

power law continuum; the observed flatter value is only because the most of the flux in the XRB is produced by active galaxies that are obscured by gas. ROSAT, due to the bandpass limited to soft X-ray photons, naturally missed most of these absorbed sources.

The latter confirmations come with Chandra and XMM-Newton deep surveys. Because of excellent (1–3 arcsec) X-ray positional accuracy of these satellites, a significant improvement had been achieved in matching to faint multiwavelength counterparts. The efficient follow-up studies indicate that up to 80% of the detected sources are AGN, but in contrary to the objects from previous missions, a lot of these sources were obscured. Moreover, type-2 QSOs, a class of highly luminous and highly obscured type-2 AGN, as an analogue of unobscured type-1 quasars, has been detected in the deepest Chandra and XMM-Newton surveys (e.g. Norman et al. 2002).

All these results imply that depending of the flux/luminosity and energy limits we can detect and study different source populations, which build up the XRB: the extragalactic sources at bright X-ray fluxes ($\geq 10^{-13}$ to 10^{-14} ergs cm^{-2} s^{-1}) are mostly unobscured/mildly obscured AGN (e.g. Schmidt et al. 1998, Akiyama et al. 2003); below this flux several other populations show up, such as obscured AGN (e.g. Tozzi et

al. 2001, Barger et al. 2002, Mainieri et al. 2002) and starburst and quiescent galaxies (e.g. Giacconi et al. 2001, Hornschemeier et al. 2003). The most recent detailed study of contribution from different sources classes depending on energy range by Bauer et al. (2004) also shows that the most significant contribution to the XRB are from luminous ($L_{0.5-8keV} > 10^{43}$ ergs s^{-1}) sources in both soft and hard bands, with main differences that unabsorbed ($N_H < 10^{22}$ cm^{-2}) sources contribute to the soft band, and contribution to the hard band comes from sources with an evenly distributed range of absorption column densities. Other studies of the luminosity distribution show that most of the sources creating of 0.1–10 kev XRB have luminosities of 10^{42} (60% of them are obscured sources) to a few times 10^{44} erg s^{-1} (mostly unobscured). The trend also suggests that less luminous and more highly obscured AGN are dominating at higher energies, e.g. obscured quasars with luminosities of 10^{44}–10^{45} erg s^{-1} create $\sim$ 10 % of the 0.1–10 keV XRB.

With these results from deep surveys, our understanding of the origin of the X-ray background seems to be quite close, except the very hard 5–10 keV band where we still have quite a significant fraction of unresolved XRB, suggesting the existence of a postulated new population of faint sources, largely undetected within the current sensitivity limits of the deepest X-ray surveys. The most recent synthesis models (e.g. Gilli, Salvati & Hasinger 2001; Franceschini, Braito & Fadda 2002; Gandhi & Fabian 2003; Ueda et al. 2003; Comastri 2004) also suggest there may be an unresolved population of highly obscured, faint AGN; this theory supports by recent indications of steepening of X-ray source number counts at low fluxes (e.g. Rosati et al. 2002). Such objects would have negligible flux below 2 keV, and therefore weak scattered soft component, consistent with the emission from almost complete (4π sr) coverage by obscuring matter. Similar properties have the Compton-thick[5] objects, which are quite common at low z and comprise $\sim$ 40% or more of AGN in the local universe (e.g. Matt et al. 2000), but very rare, due to the difficulties of there detection, at high redshifts (Stern et al. 2002, Norman et al. 2002, Gandhi et al. 2004). The required column density for such AGN must be of $N_H \geq 10^{24}$ cm^{-2} in order to harden an intrinsic $\Gamma = 2$ emission spectrum into the shape of the faint, hard, unresolved population. Worsley et al. (2004) also proposed, using simulations, that this failure to account for XRB in the harder bands can be due to a population of faint and heavily obscured AGN at z $\sim$ 0.5–1.5. Therefore, we need to wait until the new even deeper surveys with current and future X-ray telescopes are conducted. These surveys will provide images of the hard X-ray components above 10 keV, and we will be able to test this hypothesis.

In Fig. 1.3 a compilation of XRB measurements in different energy bands is shown along with the best-fit model from Comastri et al. (2001). The integrated contribution of unobscured and obscured AGN, the latter split into Compton thin (N_H=10^{21}–10^{24} cm^{-2}) and Compton thick (N_H >10^{24} cm^{-2}) AGN, are also reported. Even though such model is not able to reproduce some of recent Chandra and XMM-Newton data, it can be considered representative of most of the population synthesis models in

[5]A source, which absorbed by column density equal or large than the inverse of the Thomson cross-section, $N_H \geq 1.5 \times 10^{24}$ cm^{-2}.

meaning of possible contribution of high obscured sources (Compton thick) into XRB spectrum (e.g. Ueda et al. 2003 derived very similar integrated contribution of mildly Compton thick sources, although they used the more satisfactory description of the recent observational constraints). The Compton thick sources provide a non-negligible contribution only around the peak energy of the XRB spectrum (around 20–30 keV), while the obscured, Compton thin AGN accounted for the most energy density in the whole band. However, the main problem of all population synthesis models is that the relative fraction of absorbed ($N_{\rm H}$ $>10^{22}$ cm^{-2}) sources as a function of the 2–10 keV flux is significantly overestimated over the entire range of fluxes. While the model (with included Compton thick sources) does fit the results from deep pencil beam surveys, the absorption distribution obtained with shallow, large-area surveys is different and shows up to 2 time less absorbed objects in the total number of sources (in comparison with deep surveys).

Such a discrepancy, together with the new redshift distribution of unobscured/obscured AGN (see Section 1.3.2) is calling for some revision of basic assumptions of the standard XRB model (e.g. Hasinger, Miyaji & Schmidt 2005) .

1.3.1 Optical and X-ray classifications

Studies of the composition of the X-ray background require the *optical* identification and classification of the X-ray sources. Hence, it is important to mention some rules of such identifications.

In the zero-th order unification schemes, there is a correspondence between X-ray and optical absorption: type-2 narrow-line objects are X-ray obscured and type-1 broad-line objects are not. The underlying continuum is intrinsically the same, and the differences in the optical and X-ray spectra are only due to orientation effects. Also assumed that Seyfert galaxies are AGN, and optical spectra without high-ionisation lines correspond to normal galaxies in both optical and X-ray classification. However, the large sample of already identified sources shows that the situation is not so simple and classification of X-ray sources is challenging for several reasons.

In optical studies we can subdivide Seyfert galaxies into two classes depending on the width of the Balmer lines compared to that of forbidden lines. Applying these definitions poses very serious problems for the study of faint X-ray sources, because at high redshifts (z $>$ 0.3) the Balmer lines are no longer in the optical range. In addition, the most of the objects associated with faint X-ray sources are at intermediate redshifts and comparable in size to the seeing achievable with ground-based optical telescopes. As a consequence, we can only study the integrated emission from these objects, as opposed to nuclear emission from local Seyfert galaxies. Consequently, the nuclear emission can be 'hidden' in the stellar light coming from the host galaxy. The study of local Seyfert galaxies confirms that about 60% of the local type-2 Seyferts would not be classified as Seyfert-2, if only the total emission were available (Moran, Filippenko & Chornock 2002). Therefore, an obvious challenge in applying the classical Seyfert definition for faint objects is merely to recognize that they are AGN.

XMM-Newton is providing additional evidence that the one to one association of

type-1 AGN with unabsorbed sources and type-2 AGN with absorbed sources fails clearly in some cases. For example, studies of statistically significant samples of AGN from deep/medium surveys reveal a fraction of type-1 AGN that *do* require absorbing columns along the line of sight (see Section 3.4 for details), while for such type of AGN no or very little absorption is expected. Therefore, not all X-ray obscured AGN have type-2 optical spectra, and not all AGN with type-1 optical spectra are X-ray unobscured.

In general, the counterparts of the X-ray sources reveal a broad variety of optical properties. When the optical classification is uncertain, the X-ray properties (luminosity, hardness ratio, X-ray to optical flux ratio) can be used to discriminate between nuclear and stellar activity (e.g. Schmidt et al. 1998). There are several types of objects detected in the deep surveys in addition to the unobscured and obscured AGN: optically faint X-ray sources, X-ray bright, optically normal galaxies, starburst and normal galaxies, groups and clusters of galaxies and stars. The detailed description of these basic source types is given by Brandt & Hasinger (2005), therefore here I only shortly provide the main information about these classes.

Unobscured AGN cover a broad range of redshift (z $\sim$ 0–5) and comprise a significant fraction of the brightest X-ray sources (e.g. Schmidt et al. 1998, Lehmann et al. 2001, Barger et al. 2003, Szokoly et al. 2004), while *obscured AGN* have mostly z $<$ 1.5. The *optically faint X-ray sources* cannot be identified spectroscopically as previous two classes, but can be detected at other wavelengths. Many of them appear to be luminous, obscured AGN at z$\sim$ 1–4 (photo-z; Zheng et al. 2004, Mainieri et al. 2005) and, therefore, most probably are some how represent an extension of the 'standard' obscured AGN class to higher redshifts and fainter optical magnitudes. *XBONGs (X-ray bright, optically normal galaxies)* are early type galaxies at low redshifts (z$<$1), which have very interesting X-ray/optical properties: while in the X-ray band they show evidence of AGN activity (e.g. X-ray luminosity about 10^{41}–10^{43} erg s^{-1} or hard X-ray spectrum), the optical spectra look like normal non-active galaxies (i.e. no non-stellar continua or AGN emission lines). The real nature of these objects is still under discussion; one of the most reasonable explanations is that observed galaxies host completely obscured active nuclei and/or the emission lines related to the more or less obscured AGN are diluted with the galaxy light and therefore very weak and inconspicuous in some cases. Nevertheless, the detection of such objects support previous suspicions that most, if not all, galaxies host a black hole in their center, many of them active but obscured. If the XRB models are roughly correct, the obscured accretion is $\sim$ 3 times more frequent in the Universe at a low luminosity regime than unobscured accretion. *Starburst and normal galaxies* (z $\sim$ 0.1–1.5) are mostly detected in the soft band at the flux lower than 10^{-16} erg cm^{-2} s^{-1}. The fraction of these sources significantly increases at fainter fluxes and they are believed to be the dominant source population below 10^{-18} erg cm^{-2} s^{-1} (e.g. Hornschemeier et al. 2003, Miyaji & Griffiths 2002). Their observed X-ray luminosity function has a lognormal form, as is also observed for galaxies at infrared and radio wavelengths (Norman et al. 2004). An additional contribution to the soft band comes also from *groups and low-luminosity clusters of galaxies* at z $\sim$ 0.1–1. The properties of these

soft extended sources are in good agreement with the properties of similar nearby objects (e.g. luminosity and temperature). For a good overview on this topic see Rosati, Borgani & Norman (2002). Finally, the late-type (G, K, M) *Galactic stars* are the smallest fraction of the detected X-ray sources and contribute mostly to the soft band ($\sim 5\%$).

1.3.2 Redshift distributions

Extensive multiwavelength follow-up observations give us the possibility to construct a large sample of distant and nearby AGN with secure redshift measurements and to compare their redshift distribution with those predicted by models. The X-ray background population synthesis models (e.g. Comastri et al. 1995, Gilli et al. 2001), based on the AGN X-ray luminosity function and its evolution, predict a maximum in the AGN/QSO redshift distribution at $z \sim 1.5$. Contrary to these expectations, the observed distribution peaks around 0.7 (e.g. Hasinger 2004) and implies that about 60% of the XRB originates at $z < 1$ (Barger et al. 2003). This low redshift peak is dominated by both types Seyfert galaxies with luminosity $L_X = 10^{42}$–10^{44} erg s^{-1}. This result indicates that the evolution of Seyfert galaxies occurs at significantly later cosmic time than that of QSOs. This clearly demonstrates that the population synthesis models will have to be modified to incorporate different luminosity functions and evolutionary scenarios for intermediate-redshift, lower-luminosity AGN (see following subsection).

One of the interesting results obtained from the observed redshift distribution from deep X-ray surveys is an excess of objects in particular redshift bins, which indicate a large-scale structures of X-ray sources (CDFS and CDFN, Gilli et al. 2003, Barger et al. 2002). These narrow redshift spikes ($z \sim 0.5$–2.5) are populated mostly by type-2 (about 70%) and type-1 AGN, as well as a few X-ray galaxies. Such spikes, which likely are a cause of the cosmic variance, are also seen at corresponding redshifts for sources in other wavelengths and have been associated with X-ray source clustering in large-scale sheet-like structures with sizes of $\geq$ 5–10 Mpc.

1.3.3 Evolution of AGN and SMBH

The cosmic evolution of AGN and their supermassive black hole is one of the important questions in the astrophysics. Until now most of the studies in this area were done using information obtained in the optical band based on large sample of optically selected luminous quasars. It was found, that these objects evolve positively with redshift up to $z \sim 2$ (a comoving space density at this redshift is more than 100 times higher than at $z = 0$) with a following strong decline from $z \geq 2.7$ (e.g. Croom et al. 2004, Schmidt, Schneider & Gunn 1995, Fan et al. 2001). Recently, it was possible to create sample of AGN selected in the soft and hard bands based on X-ray luminosity. Pure luminosity evolution (PLE) models, which provide acceptable fits to sample of optically selected luminous quasars, appear to be not well matched to the results of X-ray selected sample. Moreover, it was shown that X-ray selected moderate-

luminous AGN in both bands require luminosity-dependent density evolution (e.g. Miyaji, Hasinger & Schmidt 2000, Ueda et al. 2003, Hasinger, Miyaji & Schmidt 2005). The shape of the LDDE in different redshift shells is significantly different so that the cosmological evolution can be described neither by pure luminosity nor pure density evolution (which, in addition, have physical difficulties: PLE models tend to overpredict the number of very massive [$> 10^{10}$ $M_\odot$] black holes in the local universe, whereas simple PDE models tend to overpredict the local space density of quasars and the XRB intensity). A sample of about 1000 AGN selected in the 0.5–2 and 2–10 keV shows that strong positive evolution from z $\sim$ 0–2 is only seen at high luminosities; lower luminosity AGN evolve more mildly. The most resent analysis by Hasinger, Miyaji & Schmidt (2005) shows that the comoving space density of AGN in different luminosity ranges is a strong function of redshift: firstly, the AGN peak space density moves to smaller redshift with decreasing luminosity, and, secondly, the rate of evolution from the local universe to the peak redshift is slower for less-luminous AGN. These results imply that SMBH generally grow in an 'anti-hierarchical' fashion: the massive black hole ($\sim 10^8$–10^9 $M_\odot$) in rare luminous AGN grow efficiently at more early times (z $\sim$ 3), than the moderate massive ($\sim 10^6$–10^7 $M_\odot$) BH in the more-common, less-luminous AGN (z < 1.5).

Understanding of AGN evolution is the key requirement in the understanding of black hole demography. As discussed before, we have strong evidence that probably all galaxies contain black hole in their center, most of which do not show activity at the present time. The AGN luminosity function is important in terms that can be used to predict the masses of remnant SMBH in galactic centers. This is possible to do using the Sołtan's continuity argument (Sołtan 1982), adopting an AGN mass-to-energy conversion efficiency (η), the average redshift of the peak of AGN activity ($\langle z \rangle$) and the bolometric correction factor (k_{bol}, relates the total emissivity to the emissivity in the chosen band). In this case, the observed local BH mass density ($\rho_\bullet$) can be explained in terms of the overall black hole mass density accreted in the AGN phase:

$$\rho_\bullet = \frac{1}{\eta_{0.1} c^2} \frac{4\pi k_{bol}}{c} (1 + \langle z \rangle) I_0 \tag{1.1}$$

where $\langle z \rangle$ is the average redshift of the X–ray sources detected in the particular band, I_0 is the absorption corrected XRB intensity in the same energy band and $\eta_{0.1}$ is the mass-to-energy conversion efficiency of the accretion process divided by 0.1. Expected values of η are about 0.054 and $\sim$ 0.36 for a Schwarzschild (non-rotating) and Kerr (rapidly rotating) black hole, respectively. Early estimates from the XRB spectrum, including obscured accretion power (i.e. 80% of the accretion is obscured), and assuming the same evolution for moderate-luminosity AGN and quasars (i.e. $\langle z \rangle$ = 2) led up to 6–17 $\times$ 10^5 $M_\odot$ Mpc^{-3} (Fabian & Iwasawa 1999; Elvis, Risaliti & Zamorani 2002). However, these values need to be revised downward by a factor of $\sim$ 3 in light of the currently observed evolution of XRB sources (Fabian 2004). After these, obtained values will be in good agreement with the most reliable value to-date derived by Marconi et al. (2004) using the Ueda et al. (2003) hard X-ray luminosity function and a plausible correction for missed Compton-thick AGN: $\rho_\bullet \sim 3.5 \times 10^5$ $M_\odot$ Mpc^{-3}

(in comparison with $\rho_\bullet = 2$ in the above units derived from optical quasar luminosity function, e.g. Yu & Tremaine 2002).

Moreover, an important application of such studies is the possibility to compare the BH mass density expected from the AGN activity with that observed in nearby galactic bulges. This is done using the tight correlation observed between the BH mass and velocity dispersion ($M_\bullet$–σ relation) and luminosities of galactic bulges (e.g. Gebhardt et al. 2000; Ferrarese & Ford 2005; and references therein). Using appropriate σ- and luminosity functions for local galaxies, several author estimate $\rho_\bullet$ in order of the 3–5 $\times$ 10^5 $M_\odot$ Mpc^{-3} (Yu & Tremaine 2002, Marconi et al. 2004). These values are plausibly consistent with the current best estimates of accreted mass density for $\eta \sim 0.1$.

1.4 The X-ray spectra of AGN

X-ray observations probe the central regions of AGN where we expect to have high temperatures and extreme physical conditions. In the standard paradigm, this corresponds to the inner parts of a geometrically thin accretion disc (AD) around a supermassive black hole. As a result of hydrodynamical and/or magneto-rotational instabilities in an AD and the buoyancy of the generated magnetic field (e.g. Miller & Stone 2000), we expect to have a hot corona (T $\sim 10^8$ K) lying above the relatively cool AD. The structure and heating mechanism of the corona remains unclear although numerous authors have developed different models to fit the observations. The main geometry and corresponding models are: slab or sandwich corona (Shakura-Sunyaev Disc, slim disc), patchy corona (magnetic flare, separate active blobs), sphere+disk geometry (ADAF). Although the mechanisms of plasma heating are still under discussion, most probably they invoke magnetic processes (e.g. magnetic reconnection events), similar to flares in the solar corona.

The majority of models ascribe the main component of the X-ray spectrum, the power law continuum, to Inverse Compton scattering of optical/extreme ultraviolet photons (produced in the AD) by the disk's electron atmosphere. Variations in this scenario depend on the energy distribution of these electrons (i.e. thermal/Maxwellian or non-thermal/power law) and their exact location with respect to the AD (e.g. Haardt & Maraschi 1991, 1993; Zdziarski et al. 1994).

The intrinsic AGN spectrum can be described at low energies to first order by a power-law spectral function,

$$I(E) = FE^{-\Gamma} \tag{1.2}$$

with a flux density F (normally taken at 1 keV), and photon index Γ (Γ is the commonly used in X-ray astronomy instead the spectral index α; $\Gamma = \alpha + 1$). The mean X-ray photon index of AGN is 1.8 with the little scatter (e.g. Mushotzky 1984, Turner & Pounds 1989).

Observations with Beppo-SAX and the Compton Gamma Ray Observatory (Perola et al. 2002, Zdziarski et al. 1995) showed that the power law continuum of the Seyfert

1s have an exponential cutoff at an energy $E_{cut} \sim$ 70–300 keV. Therefore, a more general form for the power law spectrum is:

$$I(E) = FE^{-\Gamma}e^{-E/E_{cut}}$$

However, the power law model is only a simple approximation of the X-ray spectral complexity. High quality data show several other components which are important in specific regions of the X-ray spectrum. The theory predicts that some of the X-ray radiation is reprocessed in the surrounding optically thick material, such as the Compton-thick dusty molecular torus surrounding the accreting system, and the accretion disc, giving rise to prominent Fe K_α lines. These emission lines at 6.4–6.7 keV have been detected in a large number of obscured and non-obscured AGN (see e.g., Nandra & Pounds 1994, Nandra et al. 1997) and will be discussed in detail in the following subsection. The shape of the line and the exact location of the emission is still intensively studied, although most of the emission seems to come from neutral Fe in Compton-thick material, and in most Seyferts, the line is not broadened, so it must be produced beyond $\sim$20 R_g. The spectra are seen to harden at high energies (above $\sim$8 keV) to form a bump peaking at $\sim$ 30 keV (e.g. Pounds et al. 1990). This can be explained by reprocessing (Compton scattering or 'reflection') of the X-ray power law within optically thick material (accretion disc). Photoelectric absorption by elements within the disc result in Compton reflection only becoming dominant beyond the absorption edge of iron. Beyond the peak at $\sim$ 30 keV the spectrum steepens due to the effects of energy loss to electron recoil and reduction in the scattering cross-section.

The soft-excess, as one of the components in the observed AGN spectrum, is dominant at energies below $\sim$ 1 keV. This component is observed in both type-1 and type-2 AGN but its origin is believed to be different in these two classes. Although it origin in type-1 AGN is still unclear, since its determination depends on a knowledge of the shape of the power law and the quantity of absorption, there is evidence (e.g. Walter & Fink 1993) that it is connectected to the 'big-blue bump' seen in the UV spectra of AGN and therefore to the emission from the disc. The most popular model ascribes the observed component to soft primary (thermal) X-ray emission from the disc, while other interpretations include gravitational energy released by viscosity in the disc and secondary radiation from the reprocessing of hard X-rays in the surface layers of the disc. The soft excess in the type-1 AGN is commonly modeled as a blackbody emission with energies up to a few hundred eV, although acknowledging that the accretion disc could not produce such high temperature emission. A good alternative explanation for the high temperature (>100 eV) cases is that the emission could be result of Comptonization of lower-energy photons by a higher energy corona above accretion disc. However, the most recent relativistically blurred photoionized disc model by Ross & Fabian (2005) appears to be a successful competitor to simple models like a blackbody and power law. In this reflection dominated spectrum model, the soft excess is a consequence of a blurred ionized disc: the 'power law' is largely made up of broadened iron-line emission and the 'soft excess' of other relativistically blurred emission lines, plus the Compton reflection component. This model is designed to reproduce the radiation from the inner accretion disc around a Kerr black hole, and is more successful

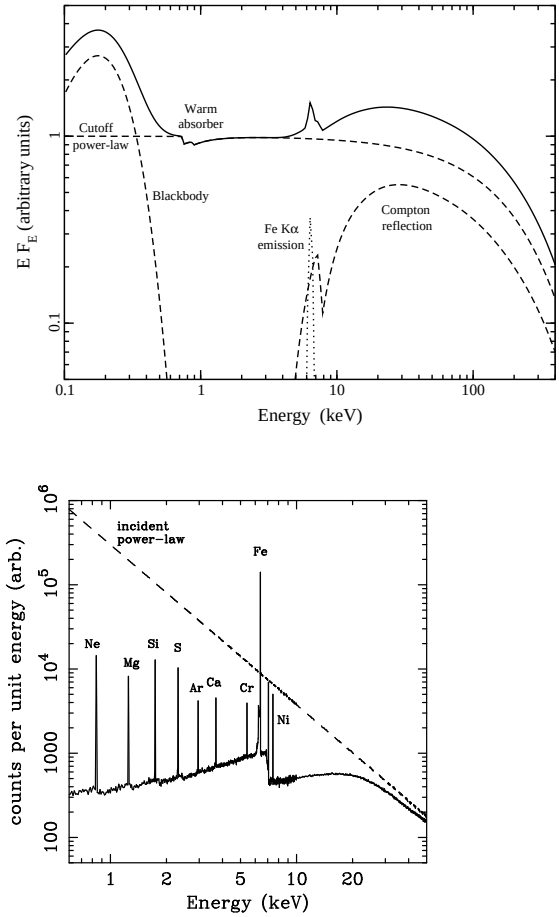

Figure 1.4: Top: A schematic representation of the intrinsic type-1 AGN spectrum with the main component between 0.1–400 keV. The primary continuum is the cutoff power-law component from Comptonization of the soft X-rays in a corona above the disc with a photon index of $\Gamma \sim 2$ and a cutoff energy $E_{cut} \sim 200$ keV. The soft quasi-thermal X-ray emission from the accretion disc (soft-excess) dominates below ~ 1 keV and is shown as a blackbody with a temperature of kT=45 eV. Two edges are shown at energies consistent with O VII and O VIII, portraying a warm absorber. A reflection continuum with the Compton hump at $E \geq 8$ keV and the Fe K_α emission line at 6.4 keV, arises naturally from reflection of the power-law continuum off an optically thick medium. The dashed lines represent the individual components, and the solid line is the combined spectrum. The effects of mild intrinsic cold absorption have been neglected. Figure taken from Gallo (2004).
Bottom: Monte Carlo simulations of the expected reflection spectrum when an incident power law (dashed-line) illuminates a slab of uniform density neutral matter with solar abundances. Figure from Fabian et al. (2000), and based on simulation from Reynolds (1996).

at fitting type-1 AGN spectra (especially of NLS1[6]) than models based on a thermal soft excess (e.g. Crummy et al. 2005). One of the main advantages of this models that together with reproducing the shape of AGN X-ray spectra, it explains why the soft excess is always at the same temperature.

A soft component in addition to the absorbed power law is often found in the X-ray spectra of Seyfert 2 galaxies as well (e.g. Turner et al. 1997). According the unified model, the direct continuum of the type-2 AGN is strongly obscured by a putative thick torus especially in the soft energies, however part of the nuclear emission can be scattered, e.g. by free electrons surrounding the broad-line region (Antonucci & Miller 1985; Awaki et al. 1991). Hence, the observed soft-excess in type-2 AGN can be ascribed to the nuclear radiation scattered by some diffuse ionized material/warm medium (the so-called 'warm mirror', e.g. Matt et al. 1996) or/and reflected by neutral material usually assumed to be produced by the far inner side of the obscuring torus. For Compton-thick sources, which are completely blocked by the large amount of absorption, the observed spectrum can be dominated only by this scattering/reflecting component. Another possibility, which was originally proposed for nearby Seyferts 1 NGC 4151 (Holt et al. 1980) and now widely used for type-2 AGN as well, is the partial covering scenario. This model consists of a power-law continuum obscured by cold uniform matter (in the form of the clouds) which covers fraction of the source allowing the direct emission leaking through the absorber. This model is numerically equivalent to the scattering model and in most cases we cannot distinguish between them.

However, soft X-ray emission in nearby type-2 Seyferts can also be extended due to other reasons. For example, XMM-Newton grating spectra for a few brightest nearby Sey2, for which such high resolution spectroscopic measurements have been possible, reveal that the soft X-ray band is dominated by line emission from highly ionized species due mainly to recombination and resonant scattering following photoionization and photoexcitation (e.g. NGC 4151; Schurch et al. 2004). This result implies that the soft X-ray excess observed in type-2 Seyferts is due, at least in some cases, to photoionization and fluorescence of a low temperature ($\sim$40,000 K) gas in the extended NLR, which is illuminated by the incident nuclear X-ray continuum. However, in some low-luminosity Seyfert 2s ($L_X \leq 10^{40}$ erg s^{-1}) the dominant contribution in the soft X-ray band can be due to collisionally ionized plasma during episodes of intense nuclear star formation. For example, Wilson et al. (1992), using ROSAT HRI observation of the NGC 1068, interpreted the soft part of the spectra as the thermal emission from a hot nuclear wind associated with the starburst component. Nowadays we cannot distinguish between these two models contributions, because the both nuclear starburst and AGN-driven photoionized extended sturctures on scales of the order of

[6]Narrow-line Seyfert 1 Galaxies (NLS1) are a subclass of Seyfert galaxies that show unusually narrow permitted lines. These objects are believed to be accreting close to the Eddington rate or at super-Eddington rates, and have smaller black hole masses for a given luminosity compared to other AGN. The NLS1 are highly variable in the X-ray band, have intrinsically softer X-ray spectra ($\Gamma \sim 2.5$) and stronger soft excess components compared to Seyfert 1 galaxies. However, the detailed spectral fitting of the soft excess in the NLS1 has so far been unable to distinguish between ionized reflection, warm absorber and partial covering models (Boller, priv. comm.).

several hundreds parsecs are common in nearby AGN.

Due to the neutral column density ($N_{\rm H}$) of our own Galaxy, which absorbs low-energy X-rays (E < 0.5 keV), all X-ray spectra of the extragalactic sources are absorbed by an amount of at least $\alpha(E) = e^{N_{\rm H}\sigma_E}$, where σ_E is the photoelectric absorption cross-section. Type-2 AGN have additional (intrinsic) absorption, as well as, some of type-1 AGN. For the former the absorption can be ascribed a to the dusty torus in the unified AGN model, while for the latter the detected absorption can be variable on various time scales (e.g. Abrassart & Czerny 2000), and can be intrinsic to the AGN or/and to host galaxy (e.g. possibly circumnuclear star burst, which can be important for type-2 AGN as well). The presence of the photoelectric absorbtion will modify the AGN spectrum (Fig. 1.4) at soft energies by an exponential cutoff below 1 keV depending on the absorbing column densities.

However, if 'standard' type-1 AGN have either no or little neutral absorbing gas, they often exhibit signs of thin ionised gas along the line-of-sight in the form of absorbing edges, most notably O VII K (0.739 keV) and O VIII K (0.871 keV) (e.g. Reynolds 1997). This is so-called *warm absorber* (Halpern 1984) has been studied with sensitive high-resolution spectrometers on Chandra and XMM-Newton, which revealed its complex structure with hundreds of absorption and emission lines from various species (including Unresolved Transition Array features due to iron absorption). Although, the exact location of the ionised gas is still unknown, more or less clear that this warm gas is photoionized by the primary X-ray continuum and most probably surrounding the central engine. Most of the lines appear blue shifted, indicating an outflow of material with estimated velocity in the order of hundreds to several thousand km s^{-1}. The warm absorber is thought to be an ionized line-driven wind (e.g. Proga, Stone & Kallman 2000), maybe evaporated off the inner edge of a dusty torus. In most of the cases detection of this component required the low flux states of the X-ray sources, otherweise the continuum level is so high that the emission component is diluted and generally not observed.

A schematic representation of the X-ray spectrum of a type-1 AGN is shown in Fig. 1.4. The observed spectrum is a combination of a primary power law component with the reflection and the soft-excess components. Reflection is represented by the reflection continuum (characterized by the 'Compton hump') and the narrow (i.e. emitted from a distant reflector such as the torus) Fe K$_\alpha$ line at 6.4 keV. Soft-excess is represented by the soft quasi-thermal X-ray emission from accretion disc (crudely approximated as a single blackbody spectrum). The type-2 AGN spectrum look similar, only the primary continuum is heavily absorbed by torus with a large column density in the line of sight.

Observed X-ray spectra of distant AGN

Due to the lack of statistics for distant and/or faint XRB AGN the detailed analysis with complicated models are quite limited. In most cases, a single (un)absorbed power law model having a photon index of $\sim$ 1.5–2 with a component representing the iron line is a good description of the (un)absorbed X-ray spectra in the 0.2–10 keV energy

range.

However, for the best quality spectra, which constitute a fraction of the detected sources, it is also possible to search for the other spectral components that can contribute to the 0.2–10 keV emission: soft excess, ionized absorption, the Fe K emission complex and Compton reflection hump (see Chapter 3).

1.4.1 Fe K_α emission

Irradiation of the dense disc material by hard X-rays gives rise to a characteristic reflection spectrum with fluorescent narrow K_α lines from the most abundant metals. If the incident spectrum has significant flux above 7.1 keV, then, as a result of its relatively high cosmic abundance and large fluorescent yield, the Fe K_α line at 6.4 keV is significant feature in the resulting emission from the illuminated surface (see Fig. 1.4).

The Fe K_α emission line at 6.4 keV is actually a combination of two lines at 6.404 and 6.391 keV, which produce an intrinsically narrow feature (1 eV; Pozdnyakov, Sobol & Sunyaev 1979). Hence, the deviation from a symmetric narrow line profile can be used to study the dynamics of the emitting region. If the reflection spectrum, and therefore the iron line, originates from the accretion disc, the observed line shape is distorted by Newtonian, special and general relativistic effects arising from motion in the concerned matter (Fabian et al. 1989, Laor 1991). In Fig. 1.5 a schematic illustration of the line altering effects is given.

Consider a narrow annulus in a disc viewed edge-on at some distance from the BH with one side of the disc approaching the observer, while the other side receding. In the simplest non-relativistic Newtonian case, each assumed radius on the disc produces a symmetric double-peaked line profile with the peaks corresponding to emission from the approaching (blue) and receding (red) sides of the disc, shifted to higher and lower energies, respectively, by the Doppler effect. If the emission region is closer to the BH, orbital velocities in the disc become relativistic ($\sim 0.3c$) and special relativistic effects become considerable. Relativistic beaming (i.e. flux boosting) enhances the blue peak with the respect to red one, and the transverse Doppler effect ('moving clocks run slowly') shifts the entire profile to lower energies. In the immediate vicinity of the central BH, where gravity becomes strong enough, the emission will suffer from gravitational redshifting which will broaden the line and further shift the overall line profile to lower energies. The disc inclination determines the maximum energy at which the line can be seen, mainly because of the angular dependence of relativistic beaming and of gravitational light bending effects. The resulting broad and skewed profile will be a combination of all these effects integrated over all radii on the accretion disc (bottom panel of Fig. 1.5). The physical picture is further complicated, because the relativistic line profile exhibits a dependence on several physical parameters, such as the inclination and ionization state of the disc, black hole spin, the disc emissivity profile etc (e.g. see Laor 1991); all these together will produce even more asymmetrical shape of the line. As example, in Fig. 1.6 the dependence of the line profile on the observer inclination i is shown.

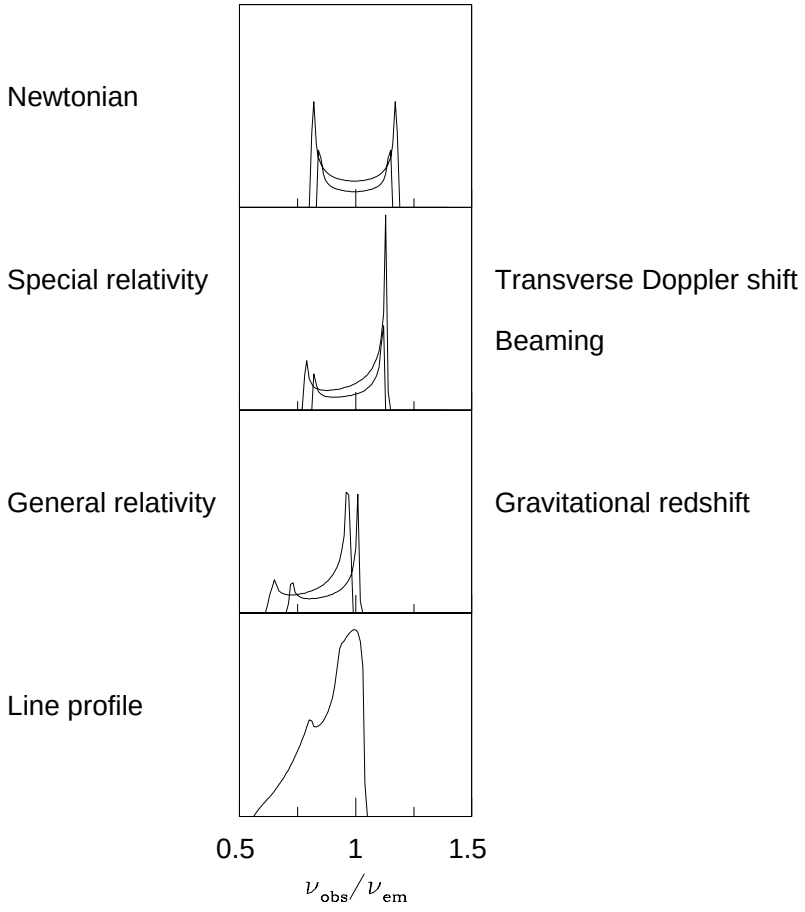

Figure 1.5: The asymmetrically broadened profile of an intrinsically narrow emission line is produced by the interplay of several mechanisms (see text for detail). Firstly, the contributions from two annuli on the non-relativistic Newtonian disc form a symmetric double-horned profile due to Keplerian motions (top panel). Special relativistic effects, specifically transverse Doppler shifting (making the profiles redder) and beaming (enhancing the blue peak with respect to the red), produce the redshifted, asymmetric profile (second panel). Gravitational redshifting reduces the blue peak strength, further broadens and shifts the overall profile to the red side (third panel). The predicted broad, skewed profile is a combination of all these effects summed over many annuli (fourth panel). Figure taken from Fabian et al. (2000).

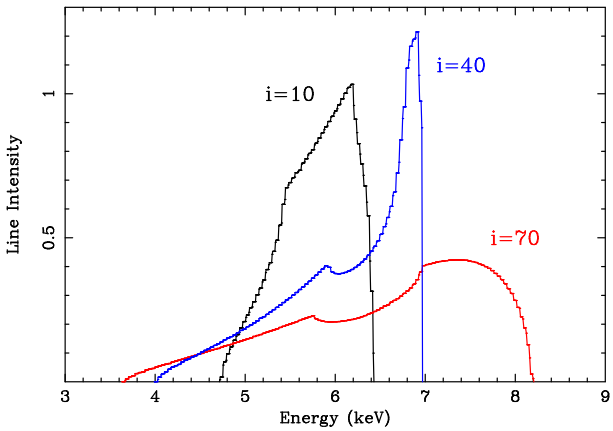

Figure 1.6: The direct dependence of the energy of the blue peak of the line on the observer inclination of axis the accretion disc i is shown. The three profiles have all the same parameters, but different observed inclination. Such strong dependence provides a quite robust tool to measure the inclination of the accretion disc in the observed spectra. Figure taken from Fabian & Miniutti (2005).

Nevertheless, the main conclusion from the discussion above is that we have strong theoretical foundation for relativistic iron line profile and, if we detect it, we can use it for better understanding the dynamics of the innermost accretion flow in accreting BHs and even of testing Einstein's theory of General Relativity.

The complex Fe line: observational evidences

Until now, the best-studied example of Seyfert 1 galaxy with relativistic Fe K_α line is MCG-6-30-15 at z=0.008. The relativistic iron feature has been discovered with ASCA (Tanaka et al. 1995) and confirmed with XMM-Newton (Wilms et al. 2001, Fabian et al. 2002). This broad (inferred Doppler velocities up to ∼c/3), distorted velocity profile with a sharp blue wing and a broad red tail is one of the most convincing confirmations of an accretion disc around a SMBH. The detailed physical modeling of this feature shows that the line emissivity comes in two parts: the blue part of the line arises from the outer accretion disk (radius >6 r_g, where $r_g = GM/c^2$ is the gravitational radius of the BH with mass M), but to account for the very extended (down to 4 keV) red tail displayed by the line a very concentrated emission at much lower radii ($\sim 2\ r_g$) is required, indicating a rapidly rotating Kerr black hole.

XMM-Newton and Chandra with their large collecting area at $\sim$ 6 keV compared to previous missions, and their improved spectral resolution (in particular with the gratings) are powerful tools for testing predictions from theoretical studies. Particularly, with the XMM-Newton observations the diversity of Fe line profiles could really be investigated and the derived information (centroid energy, intensity and profile) could be used for understanding the physics and dynamics of the region where the emission originates. The best long observations of individual AGN indicate that the iron K_α line is complex, best fitted using a relativistic iron line produced by an ac-

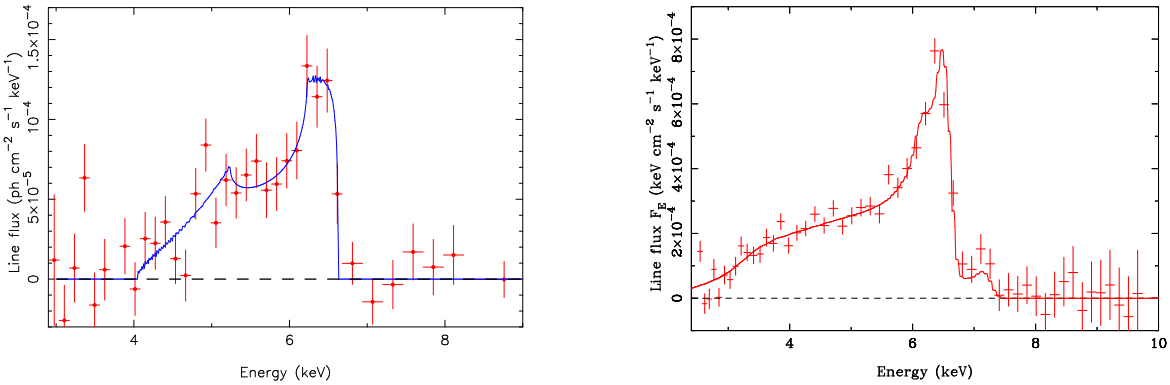

Figure 1.7: The line profile of iron K_α from Seyfert 1 galaxy MCG-6-30-15 observed by the ASCA satellite (left; Tanaka et al. 1995) and XMM-Newton (right; Fabian et al. 2002). The emission line is extremely broad, with a width indicating velocities of order one-third of the speed of light. There is a marked asymmetry towards energies lower than the rest-energy of the emission line (6.4 keV). This asymmetry is most likely caused by gravitational and relativistic-Doppler shifts near the black hole at the center of the galaxy. The ASCA observation is also the first detection of the peculiar double-horned relativistic profile, which can be produced by intense gravitational field.

cretion disc in both the Schwarzschild or Kerr metrics, variable on time-scales of few days. In general, for Seyfert 1 galaxies the equivalent width (EW) of the iron line is in order of 50–400 eV, while Seyfert 2 (especially Compton-thick Seyfert 2) show much stronger emission line with EW up to 1 keV. In general, the Seyfert 2 galaxies show more complex emission line structure than type-1 Seyfert (e.g. XMM-Newton, Chandra and ASCA observation of NGC 1068).

Observations of many Seyfert galaxies have shown a diversity in line shapes and that the profile of the iron line varies very much from source to source. The most recent evidence is even more controversial. Studies of the AGN with ASCA suggested that broad, low-ionization Fe K_α emission is common in AGN (Nandra et al. 1997; Reynolds 1997, Yaqoob et al. 2002), however, from these large number of AGN only a few of the detections have been confirmed with XMM-Newton and Chandra. In addition, only a small fraction of Seyfert galaxies seems to emit relativistic iron lines (e.g Balestra et al. 2004) and the line shapes observed with XMM-Newton and Chandra are more complicated. For example, it was noticed even with previous satellites that some luminous AGN showed narrow, neutral Fe line originating in a molecular torus (hypothesized to lie outside the broad line regions in AGN unification schemes), which only sometimes is also accompanied by a broad ionised line originating in the inner parts of an accretion disc. For example, the two famous cases showing both a narrow components at 6.4 keV and a broad component centered at 6.7 keV are Mkn 205 (Reeves et al. 2001) and NGC 5506 (Matt et al. 2001). Hence, it is still under discussion the significance of the presence broad component in the individual spectrum, especially these features are very difficult to model as an accurate determination of the continuum is required.

1.4.2 Fe line and XRB

Since the iron line is a common feature in the spectra of individual AGN, we expect to see its contribution in the integrated spectrum of all sources making the XRB. An important ingredient to the background synthesis models is the average X-ray spectrum of AGN, which at the moment has been largely taken from the local samples of Seyfert-1 and Seyfert-2 galaxies. The typical model includes at least two parameters: the slope of the AGN spectrum and the absorbing column. A possibility to detect a feature in the cosmic spectrum arising from the Fe line has been first studied by Schwartz (1988), where narrow Fe lines were assumed. However, the role of the fluorescent Fe line is still under discussion.

For the first time, a possible contribution of the iron line has been quantitatively estimated by Gilli et al. (1999) based on the XRB synthesis model of Comastri et al. (1995), and on the results obtained before Chandra and XMM-Newton. The calculation shows that the integrated emission appears as a broad bump extending from about 1 keV (depending on the maximum redshift assumed) up to 6.4 keV with an intensity of less than 5% above the XRB level. The bump reaches a maximum of $\sim$7% at around 2–3 keV (corresponding to the assumed redshift where evolution of the AGN luminosity function is stopped). Although such an estimate is model dependent, Gilli et al. (1999) concluded that it can be safely regarded as an upper limit to the total iron line contribution. In the XRB synthesis model worked out by Gandhi & Fabian (2003) based on the new redshift distribution obtained with Chandra and XMM-Newton, the iron line contribution turned out to reach its maximum at about 3.8 keV (corresponding to a typical redshift of 0.7) and the excess due to the iron line is of the order of 3%–4%. In all these models the narrow line as a basic profile is assumed.

Recent observations of the XRB spectrum however, do not have the required sensitivity to detect the iron line feature predicted by these models. Therefore, alternative methods have been proposed and applied in order to avoid the line smearing due to the large redshift range over which AGN spectra are summed, and the uncertainties present in the XRB spectrum. Brusa et al. (2005) made an analysis in narrow redshift bins, while Streblyanska et al. (2005) made a further improvement by shifting the individual spectra to the rest frame. While the first approach resulted in an iron line detection, the application of the second method had an advantage not only to detect the line feature, but also to see its intensity and relatively broad profile.

This detection of the relativistically broadened lines beyond the local universe requires the revision of the current XRB models.

1.5 The two deep XMM-Newton surveys

The Chandra Deep Field South (CDFS) and Lockman Hole (LH) fields are two well-studied fields in X-ray astronomy, because the Galaxy absorbing column densities in these directions are very low ($8.9\times\ 10^{19}$ cm^{-2} and $5.7\times\ 10^{19}$ cm^{-2}, respectively; Lockman et al. 1986) compared to the typical 2–3 $\times\ 10^{20}$ cm^{-2} at high latitudes (Elvis

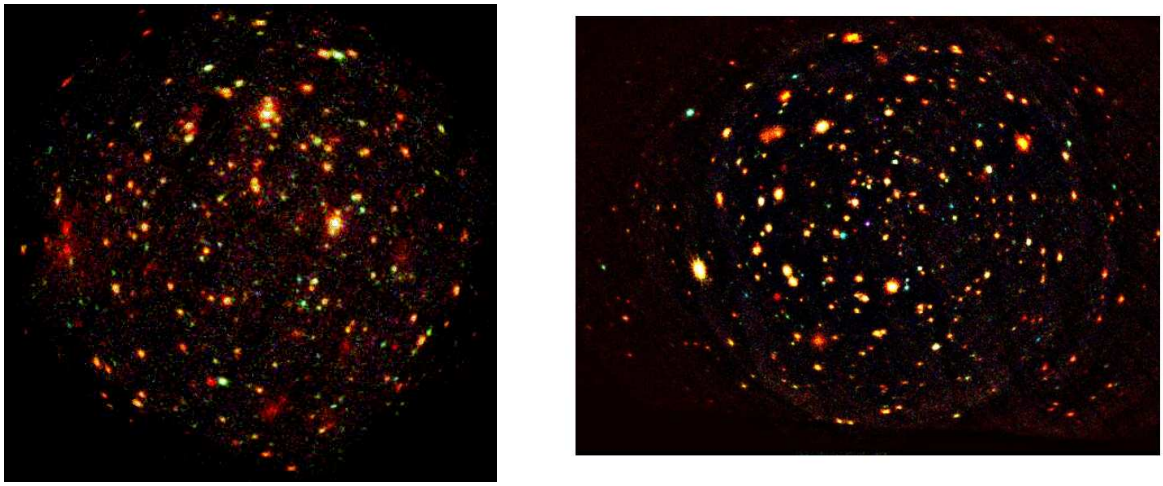

Figure 1.8: Left: The composite 370 ksec raw photon image of the Chandra Deep Field South. The image was obtained combining three energy bands: 0.5–2 keV, 2–4.5 keV, 4.5–10 keV (respectively red, green and blue). A few diffuse reddish (i.e. soft) sources, associated with groups of galaxies can be seen. Right: The similar image for 770 ksec observation of the Lockman Hole, the deepest XMM observation to date (Hasinger 2004). The fields subtend solid angles of 802 and 1556 arcmin^2, respectively. The numbers of detected sources are ∼360 and ∼550 for CDFS and LH, respectively.

et al. 1994). In the direction of both fields deep observations were carried out with the XMM-Newton (LH and CDFS) and Chandra (CDFS) satellites. The Lockman Hole was observed by XMM-Newton for 770 ksec, which is the deepest XMM-Newton observation to-date. Together, these datasets provide two deep reference fields for studies of distant normal and active galaxies, clusters of galaxies and even faint stars in our own Galaxy. Since these two fields are not only very important in the studies of XRB, but also the X-ray data obtained from both fields have been used in this dissertation, I provide a brief description of multiwavelength observations of these fields.

1.5.1 The Chandra Deep Field South Field

The *Chandra Deep Field South* field is one of the sky regions best studied at X-ray wavelengths via the Chandra and XMM-Newton satellites. This area had been studied intensively by means of a megasecond dataset from the Chandra Observatory (Giacconi et al. 2001, Giacconi et al. 2002, Rosati et al. 2002, Tozzi et al. 2001, 2005, Alexander et al. 2003). This field was observed also with XMM-Newton (370 ksec good exposure; this dissertation) and re-observed with Chandra (∼250 ksec in each 4 pointings; Lehmer et al. 2005). The Extended-CDFS consists of 4 pointings, which flank the existing 1Ms datasets, and covers ~ 0.3 deg^2. These observations are almost completely overlapping with the XMM-Newton observations, and appear as the second deepest wide survey after the Lockman Hole, which covers $\sim 30\%$ more area. These

three observations made the CDFS a unique field in the X-ray astronomy: we have not only the deep pencil-beam surveys which give us a sample of AGN at lower luminosities (although biased against more luminous sources), but in addition, we also have the shallow wide-survey, which provides more complete sample of AGN for various studies, e.g. the determination of their luminosity function. The CDFS has been extensively surveyed with the Very Large Telescope (VLT) (e.g. Le Fevre et al. 2004, Szokoly et al. 2004, Vanzella et al. 2005) in order to identify detected X-ray sources. In addition to the VLT data, some other ground-based observations are also available through different follow-ups (e.g. Renzini et al. 2003, Giavalisco et al. 2004, Wolf et al. 2004). All these together made the CDFS one of the best fields with available spectral and photometric redshift information. The main datasets with redshift information, which are relevant for this work, are Szokoly et al. (2004) (spectroscopic redshifts), and Zheng et al. (2004) and Mainieri et al. (2005) (photometric redshifts).

Existing deep observations from the ground-based facilities are supplemented with *Spitzer* infrared observations (e.g. Papovich et al. 2004, Lonsdale et al. 2003) and *HST Advanced Camera for Surveys* optical observations (GEMS and GOODS projects; Rix et al. 2004, Giavalisco et al. 2004). Radio observations have been made with the Australia Telescope Compact Array (ATCA; J. Afonso et al., in preparation) and the Very Large Array (Kellermann et al., in preparation).

1.5.2 Optical identification in the CDFS

Throughout this dissertation I mainly discuss spectral properties of different source classes in the CDFS field based on combined optical–X-ray classification scheme worked out by Szokoly et al. (2004). The authors reported on optical identification work in the CDFS, which, thanks to the efficiency of the ESO-VLT, has progressed to the faintest magnitudes among the deepest X-ray surveys.

The main optical classes based on the detection of high ionisation emission lines introduced for extragalactic sources are:

• BLAGN (Broad Line AGN) – objects with broad emission lines (FWHM $>$ 2000 km s^{-1}) like Mg II, and, at large redshifts, Ly$_\alpha$; assumed to be type-1 AGN or QSO

• HEX (High Excitation line galaxy) – objects with unresolved high ionisation lines, which are not found in the H II region (e.g. O III, He II), implying an optical type-2 classification

• LEX (Low Excitation Line galaxy) – objects with unresolved emission lines consistent with an H II region-type spectra, which do not reveal nuclear activity; classified as normal galaxies or low-luminosity AGN

• ABS – objects with typical galaxy absorption line spectrum.

More than 57% sources in the CDFS are LEX+ABS objects. But among the latter (optically dull), it should be noted that there is a large number of luminous X-ray sources, which could be hidden AGN. Because the optical classification scheme is failing in identifying an AGN in about 40% of the X-ray sources classified as LEX or ABS, the alternative X-ray classification, based on the source hardness ratio[7] (HR)

[7]The hardness ratio HR is defined as $HR = (H - S)/(H + S)$, where H and S correspond to

and observed X-ray luminosity (L_X), was proposed by Szokoly et al. (2004).

Following the unified AGN model, we can define two AGN classes by using the HR, a parameter sensitive to X-ray absorption, which can be measured even for faint objects. Unabsorbed sources have a HR < -0.2, independent of z. The scatter in this value is easily explained by introducing different slopes for the X-ray spectra, together with statistical errors associated with low number counts in the X-ray bands. The harder spectra (HR > -0.2) are fully consistent with absorbed power law models. Combining this approach with the observed high X-ray luminosity (more than 10^{42} erg s^{-1} in the 0.5–10 keV band) as a signature of the presence of an AGN activity (i.e. black hole), we can clearly distinguish type-1 and type-2 AGN. We can also use the X-ray luminosity (e.g. in the 0.5–10 keV band) to separate the fainter objects or AGN ($L_X < 10^{44}$ erg s^{-1}) from the brighter ones or QSO ($L_X \geq 10^{44}$ erg s^{-1}).

The proposed X-ray classification is more successful than the classical/optical one in revealing the presence of black hole activity, whatever the amount of dust obscuration from the central and/or external parts of the nuclear region. The optical classification may be more appropriate in studies that aim to extrapolate the classical Seyfert definition to faint AGN. However, it is important to note that the proposed X-ray classification might be misleading for some high-redshift objects: an increasing absorption makes the sources harder, while a higher redshift makes them softer. Consequently, some high-redshift absorbed/type-2 sources may be mistakenly identified as type-1.

Based on this approach, the large majority of optical counterparts in our survey turned out to be AGN, with some fraction of QSOs and galaxies. In addition, a few sources showed stellar spectra corresponding to the faint background Galactic stars.

1.5.3 The Lockman Hole Field

The *Lockman Hole* was chosen as the field for the deepest ROSAT and XMM-Newton survey ever, because of its absolutely lowest column density of interstellar absorption makes it an excellent window through which to observe distant sources at X-ray energies. Over the last 13 years it has become one of the best studied sky regions over a wide range of frequencies: optical imaging in different bands, deep NIR and IR observations and a VLA mosaique have been taken. In the X-ray band the LH was a reference field for every imaging X-ray satellite: ROSAT (207 ksec with the PSPC and 1.3 Ms with HRI; Hasinger et al. 1998), ASCA hard X-ray observation (260 ksec; Ishisaki et al. 2001), Beppo-SAX, Chandra, and finally XMM-Newton (∼800 ksec). Using a subset of XMM-Newton observations (taken in the performance verification phase (PV); ∼100 ksec), Hasinger et al. (2001) presented the source detection and properties of X-ray sources. Mainieri et al. (2002) conducted an X-ray spectral analysis of the objects detected in the field, using on the optical identification and classification scheme based on ROSAT survey (Schmidt et al. 1998, Lehmann et al. 2000, 2001). Recently, using the total 800 ksec dataset created from three observation epochs, Worsley et al. (2004), (2005) calculated the fraction of unresolved XRB in

counts in the harder and softer energy bands, respectively.

different energy bands, Brunner et al. (2006, in preparation), create the source catalog for the whole field, Szokoly et al. (2006, in preparation) give the spectroscopic identification, Mateos et al. (2005) performed a detailed analysis of the 123 brightest objects. Finally Streblyanska et al. (2005) (see also Chapter 4) have conducted a detailed study of the Fe K_α emission in the stacked spectra of type-1 and type-2 AGN. We found indications for broad relativistic lines in both type-1 and type-2 AGN.

Fig. 1.7 shows the CDFS and LH colour composite images of all XMM cameras combined in an X-ray 'real-colour' representation. The red, green and blue colours refer to the 0.5–2, 2–4.5, 4.5–10 keV images, respectively. There are several bright diffuse sources with red colours which are X-ray clusters of galaxies. In both images a population of obscured faint sources (green and blue objects), which has been postulated by the X-ray background population synthesis models, is clearly detected.

1.6 XMM-Newton observatory

As it was shown, the deep X-ray surveys are the most efficient ways to analyse the X-ray background sources. However, the efficiency of such studies is very dependent on the used facilities, in other words, on a space satellite. In the early 90s, only with very long ASCA/Beppo-SAX observations, with a broad energy response, it was possible to create samples for studies of the more or less high-z sources (AGN and clusters), but even these samples were inevitably biased toward intrinsically bright X-ray sources, and thus, mostly nearby or unabsorbed AGN. Hence, it was difficult to study the AGN evolution through redshifts and even to determine the contribution of the absorbed sources to the XRB. However, our understanding of the properties of bright and faint AGN at larger z, the role of the absorption in the XRB, the X-ray luminosity function for AGN at different redshifts, and other important issues improved fundamentally after using data taken by the advanced X-ray telescopes: *XMM-Newton* (ESA) and *Chandra* (NASA). With the launch of these two satellites the new era of the X-ray background study has begun.

Since the data used in this dissertation is mainly obtained with XMM-Newton, I provide a brief description of the instrument.

The *X-ray Multi-Mirror Mission*, *XMM-Newton*, a cornerstone mission of the ESA Horizon 2000 programme (Jansen et al. 2001, Ehle et al. 2004) was launched from Kourou (French Guyana) on 1999 December 10 into a highly eccentric 48 hour orbit. Six science instruments operate simultaneously on board the largest scientific satellite ever launched by ESA. Each of the three X-ray telescopes on board XMM-Newton has effective area of 1550 cm^2 at 1.5 keV and consists of 58 Wolter I mirrors with shells replicated from super-polished gold coated mandrels with diameters up to 70 cm. All these together made XMM-Newton the most sensitive focusing X-ray telescope to-date.

The primary scientific objective of XMM-Newton is to perform high throughput spectroscopy of cosmic X-ray sources over a broad band of energies ranging from 0.1 to 15 keV. The three telescopes focus in-coming X-ray photons onto three detectors of the European Photon Imaging Camera (EPIC), each capable of working in several

instrumental modes, and two Reflection Grating Spectrometers (RGS; den Herder et al. 2001). The sixth instrument is a 30 cm optical telescope OM (Optical Monitor, Mason et al. 2001) which collects data in the optical and near-UV regime, rendering it possible to conduct simultaneous optical and X-ray studies.
Two of the X-ray telescopes are identical, and contain a grating assembly in their light path which disperses about 40% of the light onto a linear strip of 9 charge-coupled devices (CCDs). The assemblies in each telescope make up the RGSs. About 44% of the light will reach the prime focus of the two telescopes undispersed, where a Metal-Oxide Semi-conductor (MOS1 and MOS2; Turner et al., 2001) camera is installed. Each of the MOS telescopes consists of 7 CCDs each 10.9 × 10.9 arcmin with energy resolutions of 5.7% at 1 keV. The third telescope collects all X-ray light directly to its prime focus, where the EPIC p-n-junction (pn) camera (Strüder et al. 2001) is mounted. The pn detector has 12 integrated back-illuminated CCDs each 13.6 × 4.4 arcmin, with energy resolutions of 6.7% at 1 keV. The sensitive FOV of pn and MOS detectors is about 30′ in diameter. More than 90% of the flux of on-axis point sources is collected on the pn CCD chip. The effective area, which reflects the ability of the mirror to collect radiation at different photon energies, is highest for pn detector. The two MOS cameras have lower effective areas than pn, because only part of the incoming radiation falls onto these detectors, which are partially obscured by the RGSs.

One of the critical parameters determining the quality of an X-ray mirror module is its ability to focus photons. One of XMM-Newton's major advantages is that the core of its on-axis point-spread function (PSF) is narrow and varies little over a wide energy range (0.1–4 keV); above 4 keV the PSF becomes only slightly more energy dependent. In general, the XMM-Newton mirrors are most efficient in the energy range from 0.1 to 10 keV, with a maximum at about 1.5 keV and pronounced edge near 2 keV (the Au M edge).

The advantages of XMM-Newton compared to high-resolution imaging of the Chandra satellite are: 1) wide energy band, 2) unprecedented sensitivity in the hard band and 3) large FOV ($\sim$ 2.5 times that of Chandra). All these together made XMM-Newton well suited for the spectroscopic study of very faint intrinsically absorbed X-ray sources and low surface brightness X-ray emission, both of which are very common in deep X-ray surveys.

Through this dissertation the pn and MOS instruments are used. A reliable pipeline procedure of data reduction is described in detail in the later chapters (Sections 2.2 & 3.2 for CDFS field, and Section 4.2 for LH field). Briefly, the key requirements for XMM-Newton spectroscopy analysis are a good background subtraction and accurate creation of the instrumental response files.

1.7 Outline of this dissertation

The high *XMM-Newton* throughput and effective area combined with the unique arcsec spatial resolution of the *Chandra* observatory and extensive optical identification follow-up, allow us not only to obtain a high-quality X-ray spectra, but also to investigate in detail the differences between the various X-ray source classes, which build up

the X-ray background and to make accurate comparison with previous discoveries. In this dissertation I present a complete analysis of the deep X-ray survey in the Chandra Deep Field South and explore the role of the fluorescent Fe line in the mean X-ray spectra using the results from the deep survey in the Lockman Hole field.

The XMM-Newton observation together with the three source catalogues used here are discussed in Chapter 2. In Chapter 3 I discussed the main results from the spectral fitting, in particular the differences in the spectral slope and absorption between two AGN classes, the importance of the additional components for the proper modeling of the spectral shape and the importance of the stacking technique for the analysis of the faint sources. In addition, I also discuss the results from the comparison between Chandra and XMM-Newton datasets showing the dependence between spectral slope and absorption in the assuming energy range for spectral fitting. The analysis of the Fe line profile from the mean X-ray spectra of type-1 and type-2 AGN together with the general information about XMM-Newton deep survey in the LH field is presented in Chapter 4. A summary of the results and discussion of future prospects is given in Chapter 5.

Throughout the dissertation, I will assume a flat cosmology with the following values for the Hubble constant and the cosmological parameters: $H_0 = 70$ km s^{-1} Mpc^{-1} and $\Omega_\Lambda = 0.7$ (Spergel et al. 2003). All errors correspond to the 90% confidence level for one interesting parameter ($\Delta\chi^2 = 2.706$).

Chapter 2

The Chandra Deep Field South

2.1 XMM-Newton observations

The Chandra Deep Field South (CDFS) field was observed with the XMM-Newton Observatory for a total of $\sim$ 500 ksec in July 2001 and January 2002 in guaranteed observation time (PI: J. Bergeron) but, due to high background conditions and flares, some data were lost and the exposure time for good quality observation added up to $\sim$370 ksec. The XMM-Newton dataset has some specific advantages compared to Chandra, in particular, the XMM cameras have a larger field-of-view allowing for the detection of a number of new point and diffuse sources just outside of the Chandra FOV. The EPIC instruments have unprecedented sensitivity in the both hard and soft X-ray band, and in the [5–10] keV band our dataset is comparable to the 1 Ms Chandra image. In addition, XMM-Newton with its high throughput is extremely sensitive to low surface brightness (i.e. diffuse) X-ray emission, where the superb angular resolution of Chandra does not figure. These properties make XMM pn/MOS very suitable instruments to investigate the ICM properties of distant clusters.

The observed field was centered on the sky position RA 3:32:28 and DEC -27:48:30 (J2000). The CDFS was selected for its low galactic neutral hydrogen column density $N_{\rm H} \sim 8.9 \times 10^{19}$ cm^{-2} (Dickey & Lockman 1990) and a lack of bright foreground stars and bright X-ray sources (Rosati et al. 2002). The total solid angle area covered by three cameras amounts to 0.223 deg^2. The EPIC-pn camera was operated in the extended full-frame mode, while the MOS1 and MOS2 were operated in the full-frame mode. The thin filter, which is usually employed in the observations of faint sources, was used for the all EPIC cameras. The CDFS dataset we used is the result of the coaddition of 8 individual exposures with aimpoints only a few arcsec from each other. The pointing direction was changed slightly during the observation in order to fill up the gaps between the CCD chips. The pn and MOS data were preprocessed by the *XMM-Newton Survey Scientist Consortium* with the XMM-Newton standard Science Analysis System (SAS, version 5.3.3) routines, using the latest calibration data.

2.2 X-ray source list

The Calibration Index Files appropriate for the time of observation have been generated using the SAS task `cifbuild`. After that, the raw pn and MOS Observation Data Files (ODF) were processed using the SAS tasks `epchain` and `emchain` to produce calibrated event lists. Finally, the time intervals with high background were removed (by selecting the good time intervals [GTIs]). We also removed the warm pixels. Only events with pattern 0–4 (single and double) for the pn and 0–12 for the MOS cameras were selected. Images and exposure maps were formed for each observation in three energy bands (0.5–2.0 keV, 2.0–4.5 keV and 4.5–10.0 keV) and used in our analysis. Finally, the merged images (pn+MOS) in the three energy bands were searched simultaneously for sources using the SAS tasks `emldetect` and `eboxdetect`. Source detections were accepted with likelihood[1] value above 10 (about 4σ) in the total 0.5–10 keV band for the creation of the new XMM-Newton source catalogue (see Section 2.6) and with likelihood value above 8 ($\sim 3.4\sigma$) for comparison with the Chandra results (Section 3.5). The corresponding flux limits in the 0.5–2 and 2–10 keV bands are 1×10^{-16} and 9×10^{-16} erg cm^{-2} s^{-1}, respectively.

Log N–Log S

The limiting sensitivity versus the sky coverage and the corresponding cumulative log N–log S distribution in the soft, hard and very hard bands are shown in Fig. 2.2 and Fig. 2.3, respectively. The area coverage, defined as the solid angle within which a source with a given X-ray flux can be detected with likelihood value above 8, was obtained from the sensitivity maps (indicating the expected minimum detectable source count rate at each point in the field of view) created by SAS task `esensmap` using the exposure and background maps of each energy band. In this way, the limiting flux in each band was calculated taking into account the vignetting factor (dependence of the effective area on the offset angle), exposure time and appropriate flux conversion factor (using power law spectrum with Γ=2). The sharp decrease at low fluxes determines our flux limit in the corresponding band. The faintest limiting sensitivity was achieved in the center of the CDFS.

The cumulative number counts $N(> S)$, defined as the number of sources per square degree brighter than flux S, was calculated in the standard way by accumulating the inverse of the area in which each detected source could have been detected. Count-rate-to-flux conversion factors corresponding to a power-law spectral index of $\Gamma = 1.4$ were used in order to be able to compare our results with published Chandra power-law fits to the number counts.

Our log N–log S relation is consistent with Chandra results, maybe somewhat steeper (due to the large FOV of the XMM cameras and therefore larger number of

[1]The likelihood represents the significance of the detection, normalized to two nominal degrees of freedom. The likelihood is defined as $L = -ln(p)$, where p is the probability that the observed source counts are due to random Poissonian fluctuations.

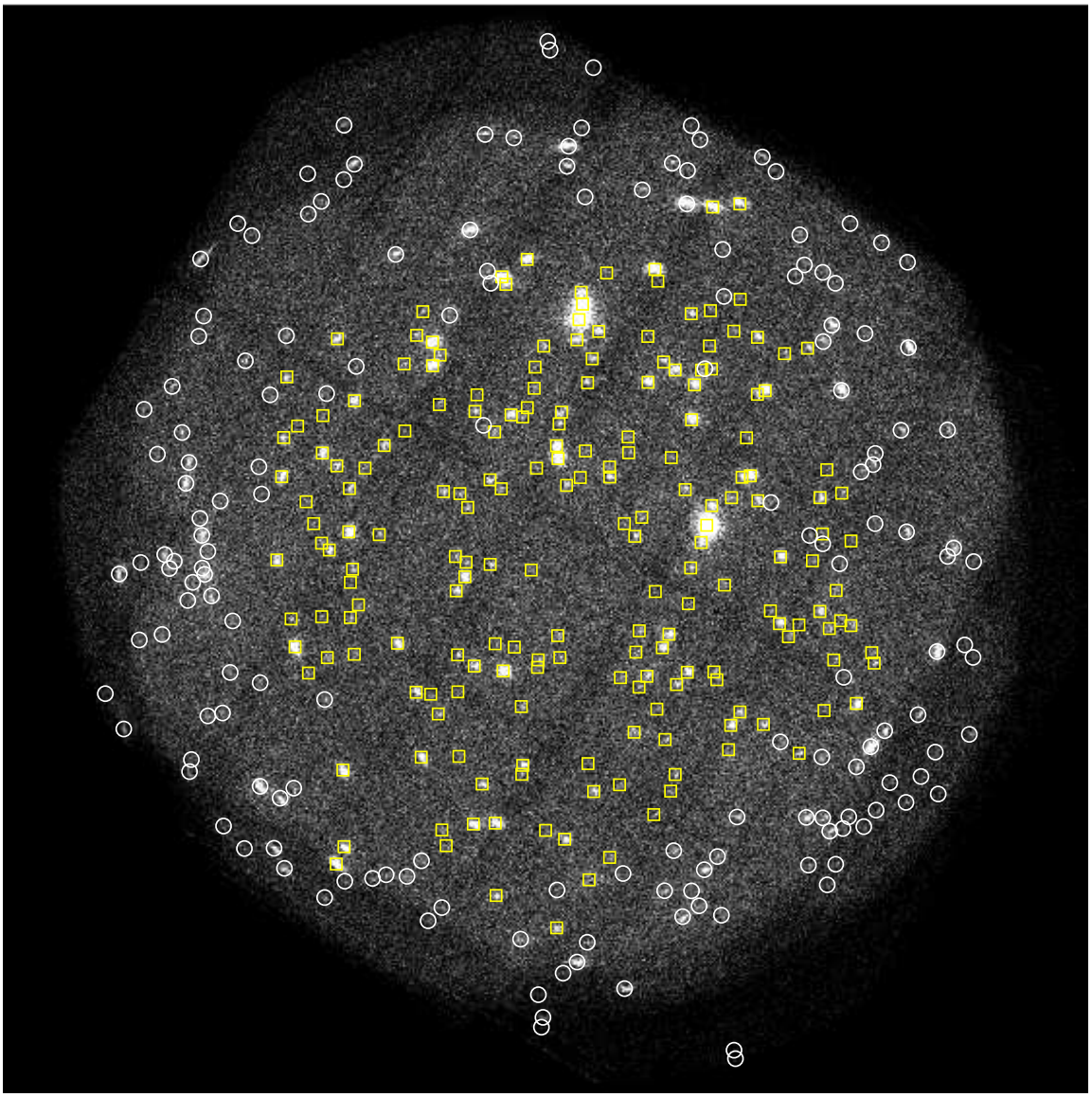

Figure 2.1: The 0.5-10 keV image of the CDFS field (pn+MOS1+MOS2) with overplotted positions of X-ray sources from the source catalog. We plotted 198 sources which overlap with the Chandra catalog as yellow boxes, and 165 new XMM sources as white circles. Some new XMM sources are also detected within the Chandra image.

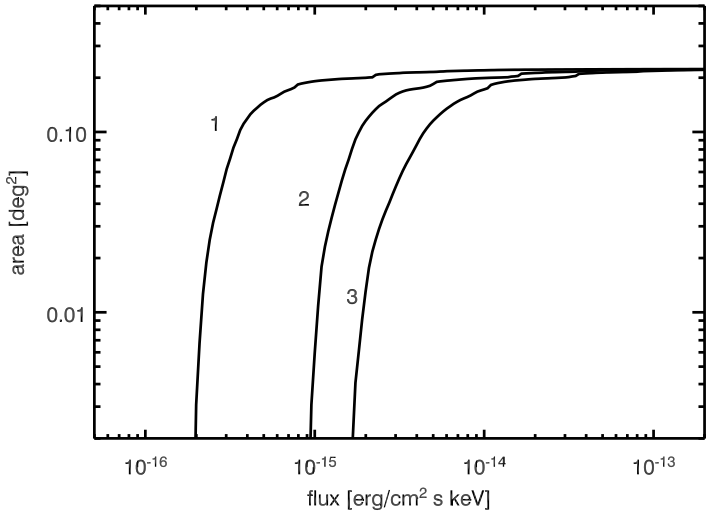

Figure 2.2: Effective survey area in each energy band as a function of detection sensitivity in the soft (1), hard (2) and very hard (3) bands.

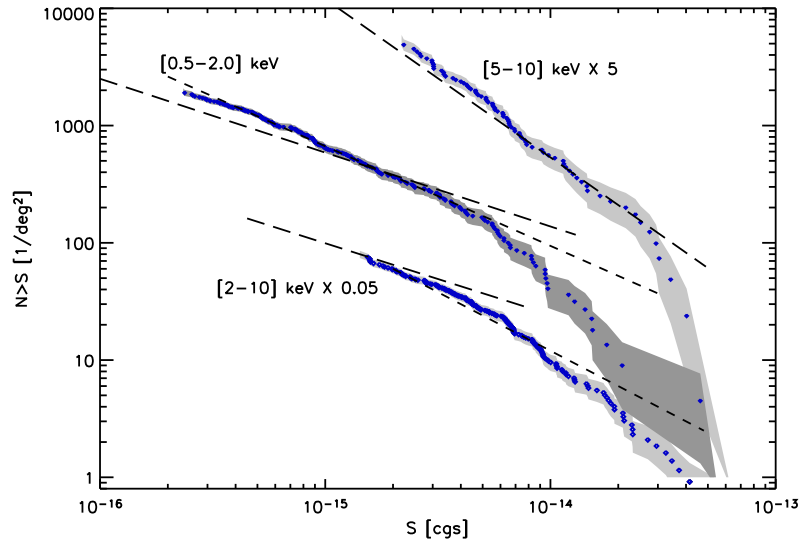

Figure 2.3: Logarithmic number counts in the energy bands 0.5–2.0 keV, 2.0–4.5 keV and 4.5–10.0 keV. The shaded areas indicate uncertainties due to the Poisson statistics (1 σ) and the choice of conversion factor (to be consistent with Chandra results we used Γ=1.4). The published power laws from the 1 Ms data sets are shown as a long (Rosati et al. 2002) and short (Giacconi et al. 2001) dashed lines.

Table 2.1: Energy conversion factors for different energy bands and different photon indices

Band[a]	ECF[b]	ECF[c]
0.5–2	11.496	11.949
2–4.5	1.3732	1.871
4.5–10	1.1783	1.3155

[a] Energy band in keV in which the flux is given
[b] Energy conversion factor in cts s^{-1} per 10^{-11} erg cm^{-2} s^{-1} for assumed photon index $\Gamma = 1.4$
[c] Energy conversion factor in cts s^{-1} per 10^{-11} erg cm^{-2} s^{-1} for assumed photon index $\Gamma = 2$

sources), and confirms a break in the slope compared to the quasi-Euclidean behaviour at brighter fluxes. As was shown by Hasinger et al. (1993) and Rosati et al. (2002), when the counts cover several orders of magnitude in flux, a single power law is no longer sufficient to obtain a good fit to the data; a double power law provides a good replacement to properly represent the bright-end and faint-end slopes.

The steeper slope in the very hard band with respect to the 2–10 keV number counts is mainly due to the hardening of the average spectrum at low fluxes, confirming the idea about the existence of a fainter and progressively harder population of sources that are likely to fill the remaining fraction of the hard X-ray background. Consistent with the models, most of the sources contributing to this band should be strongly absorbed AGN at relatively low redshifts.

2.2.1 Comparison between source catalogs from Chandra and XMM-Newton

We took advantage of the existing 1 Ms data from the Chandra observatory and made a direct comparison between our source list of 363 sources (likelihood value above 8) and a catalog of 346 sources from Giacconi et al. (2002). At first, we compared positions source-by-source for both catalogs using a matching radius of 6 arcsec. We have choosen our radius to be large enough to include possible errors in the position determination between the two satellites. However, we noticed that the XMM-Newton and Chandra positions were within $\sim$ 2 arcsec for the majority of the sources.

Taking into account the high angular resolution of the Chandra observatory, which allows us to separate close pairs of sources, we expect that XMM-Newton will be more affected by the source confusion and a fraction of nonresolved close AGN pairs will be significant. But only in a few cases (less than 0.5% of the total number of overlapping sources) we detect one XMM object when Chandra detects two.

As a result we found 198 XMM sources which overlap or coincide with sources from the Chandra dataset, including 6 cases where we have 'double' Chandra sources which were unresolved by XMM-Newton.

Chandra and XMM-Newton fluxes

The next step was a comparison of fluxes between the two datasets. The energy fluxes were computed separately in the soft (0.5–2 keV) and hard (2–10 keV) bands from the observed count rate. In order to make a direct comparison with the results from the Chandra 1 Ms data set, we use for the derivation the energy flux an energy conversion factor (ECF) consistent with the assumption in Giacconi et al. (2002) ($\Gamma = 1.4$; see Table. 2.1 for the energy conversion factors in the different bands). This number is appropriate for the measured average spectrum of all the sources in the 1 Ms dataset and is consistent with the unresolved XRB slope in the hard X-ray band. We quote the energy flux in the 2–10 keV band as extrapolated from the counts in the 2–4.5 keV band. In case of the 'double' Chandra sources we sum the fluxes in current band and use the summed flux for a comparison with XMM-Newton sources. The results in the soft and hard bands are shown in Fig. 2.4. In general, our order-of-magnitude agreement is reasonable, taking into account that we have data from two satellites with different sensitivities in soft and hard bands observing at different epochs. The fluxes in the soft band are tightly correlated with the exception of one outlier. This source is detected as extended object in both surveys, but it displays a higher soft flux in the XMM-Newton observation than in the Chandra. This is not surprising since this is an extended source detected at the edge of the Chandra observed field. On the other hand, such type of objects have a relatively low count rate per unit area, therefore extended sources in general appear to be brighter in the XMM-Newton observations than in Chandra due to XMM-Newton's larger collecting area.

In the 2–10 keV band towards fainter flux, there is a discrepancy of about 40% between the Chandra and XMM-Newton datasets, especially for sources which are situated in the CCD gaps or near the edge of the observed field. The rest of the inconsistent points may be explained by a higher uncertainty of the flux determination and error estimation in the hard band (i.e. some kind of a systematic effect of the source detection procedure), and also by possible variability of some of the AGN between the Chandra and XMM-Newton observation epochs. The latter explanation is quite probable for both bands in general, since variability within the Chandra observation is expected in as many as 90% of all AGN (see Paolillo et al. 2004).

The main conclusion from our analysis is that the differences between the instruments do not affect the source counts significantly at the currently achieved flux levels in the soft band. The same is true for the bright objects in the hard band, however a significant scatter exist for fainter objects.

2.2.2 Extended sources

From the optical identification (e.g. Szokoly et al. 2004) we know that the dominant population in the deep surveys is a mixture of obscured (type-2) and unobscured (type-1) AGN, with a small fraction of groups and clusters of galaxies. Nevertheless, these relatively rare objects like groups/clusters of galaxies contribute up to $\sim 10\%$ to the soft background at 10^{-14} erg cm^{-2} s^{-1} (Rosati et al. 1995), and the surface density of such extended X-ray sources is $\sim$ 100–260 deg^{-2} at limiting 0.5–2 keV flux of $\sim 3 \times$

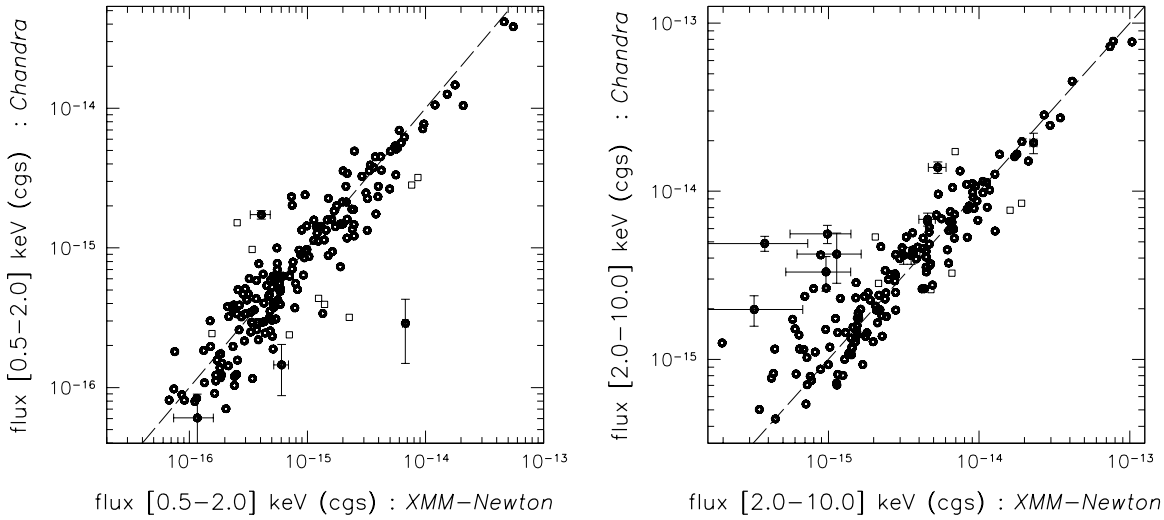

Figure 2.4: X-ray fluxes in the [0.5–2.0] and [2.0–10.0] keV: Chandra data (Giacconi et al. 2002) versus XMM-Newton results (source detection catalog). Open squares correspond to sources situated in CCD gaps or near an edge of observed field. In addition, several representative error bars are plotted. Used energy conversion factor corresponds to $\Gamma = 1.4$. *The dashed lines are lines of equal fluxes. In the soft band one prominent outlier corresponds to extended object 616 (Chandra ID).*

10^{-16} erg cm^{-2} s^{-1} (e.g. Rosati, Borgani & Norman 2002).

The 1 Ms Chandra survey probes the very faint end of their X-ray luminosity function and allows a detection of 19 extended objects, implying a surface density of extended sources in the range 50–100 deg^{-2} at the flux limit of 3 $\times 10^{-16}$ erg cm^{-2} s^{-1} in the 0.5–2 keV band (Rosati et al. 2002). With the help of the optical follow up these sources have been later associated with individual bright galaxies (z$\sim$0.1) or groups (z $\sim$ 0.5–1). The study of properties and number counts of groups at such high redshifts is one of the most sensitive tests of the cluster evolution and provides a basis for a comparison with future surveys aimed to find more massive clusters at similar redshifts.

In order to study such objects in our field, the SAS detection algorithms have been applied again to XMM-Newton images to search for extended sources. As a result, 15 extended objects with likelihood values above 10 were detected and cross correlated with 1 Ms catalog and optical spectroscopy results from Szokoly et al. (2004).

Of the 7 sources which have counterparts in the Chandra dataset, two can be associated with a close pair of Chandra sources that were not resolved by XMM-Newton. All these objects have optical identification except one source (Chandra XID 616). Most of detected sources are already known extended objects discovered in the 1 Ms data and can be associated with hot halos of galaxies (XMM ID: 3 and 4) and with groups and clusters (XMM ID: 2, 5, and 7). A few of these groups (XMM ID 2,

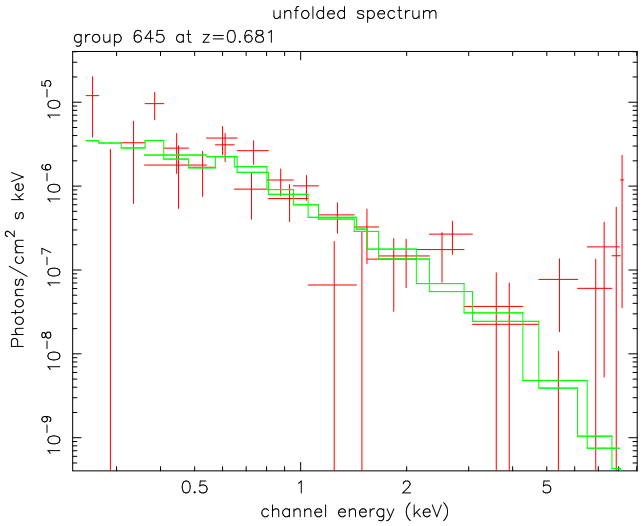

Figure 2.5: The unfolded `apec` *model spectrum of the bright extended object XID 645 spectroscopically identified as a group at $z = 0.681$. The two models (*`apec` *and* `mekal`*) gave consistent rest-frame values of the temperatures of about $2.4^{+0.7}_{-0.7}$ keV, and flux of 1.5 $\times 10^{-15}$ erg cm^{-2} s^{-1} and 6.4 $\times 10^{-16}$ erg cm^{-2} s^{-1} (in the 0.5–2 and 2–10 keV bands, respectively).*

7) were found to be associated with the large-scale structures reported by Gilli et al. (2003). Only one XMM-Newton object was spuriously detected as extended due to the presence of a close pair of bright AGN (XMM ID 1). The preliminary comparison of X-ray properties of sources which are common for both surveys shows that the extent detected by XMM-Newton is mostly larger (2–5 times) than that measured by Chandra.

As an example of the quality of XMM-Newton data, we extracted a spectrum of one of the bright extended objects (XMM ID 7, or 645 from Chandra) and fitted it with two optically thin thermal plasma models (`apec` and `mekal` in `XSPEC`). Both models gave consistent temperatures and fluxes (see Fig. 2.5).

The 8 new XMM-Newton extended sources have no spectroscopical identification yet. In the case of two new XMM sources (XMM ID: 8 and 13) their diffuse X-ray emission could be ascribed to thermal halos of nearby interacting galaxies, but the nature of the remaining 6 objects is still not clear.

In Table 2.2 we present complete information about the extended objects detected in our survey. Our cluster list is dominated by the low-mass clusters, with median redshift of 0.7. The mean surface brightness of these diffuse sources is as low as 10^{-15} ergs cm^{-2} s^{-1} arcmin^{-2}. From the number of the detected extended sources we estimated the cluster number density of 84 ± 22 clusters per square degrees at the 4×10^{-16} erg cm^{-2} s^{-1} flux level in the 0.5–2 keV band (Finoguenov, priv. comm.). Such cluster number density is among the highest known (e.g. Rosati, Borgani & Norman 2002) and is in agreement with other estimates at such flux levels.

A complete analysis of these extended objects and their properties will be presented in Finoguenov et al. (2006, in preparation). Our preliminary analysis shows that the

Table 2.2: Extended sources.

ID[a]	ID Chandra	RA (J2000)	Dec (J2000)	z	opt. class	E[b]	s. flux[c]	h. flux[d]
1	41 & 43	03:32:27.2	-27:41:45.5	0.667, 0.737	AGN II	5.9	2E-15	9E-15
2	594	03:32:09.4	-27:42:42.4	0.733	group	14.8	2E-15	3E-15
3	211	03:32:05.5	-27:54:42.6	0.679	galaxy	19.7	2E-15	–
4	116 & 103	03:32:29.4	-27:44:02.7	0.076, 0.215	galaxies	6.8	1E-15	2E-15
5	249	03:32:19.0	-27:54:09.6	0.964	group	8.3	1E-15	2E-15
6	616	03:32:25.5	-27:58:49.5	-	-	27.2	7E-15	1E-16
7	645	03:31:50.4	-27:49:36.4	0.681	group	28.1	7E-16	5E-16
8	-	03:33:20.8	-27:48:57.8	-	-	60.0	3E-14	1E-14
9	-	03:32:39.5	-27:39:58.3	-	-	57.4	1E-14	2E-14
10	-	03:32:10.8	-27:59:10.4	-	-	22.4	2E-15	–
11	-	03:32:45.4	-27:40:59.0	-	-	14.8	2E-15	–
12	-	03:32:31.4	-27:32:19.6	-	-	25.1	6E-15	3E-14
13	-	03:33:21.1	-27:47:23.7	-	-	27.9	3E-15	–
14	-	03:31:50.3	-27:39:57.9	-	-	14.5	2E-15	–
15	-	03:32:24.9	-27:33:09.4	-	-	38.7	8E-15	2E-14

[a] XMM-Newton unique ID
[b] Extent in arcsec (converted from image pixels: 1 image pixel = 3 arcsec)
[c] flux in (0.5-2 keV) band, cgs units
[d] flux in (2-10 keV) band, cgs units

X-ray luminosities ($L_X \sim 10^{41.5}$–10^{43} erg s^{-1}) and temperatures ($kT < 3$ keV) are in good agreement with previous findings from deep surveys for such bright sources.

2.2.3 New XMM-Newton sources

As one of the results of our analysis, we expected to detect new sources in the CDFS due to the larger field-of-view of the EPIC compared to the ACIS. Therefore we selected all sources with likelihood values above 10 and without Chandra counterparts. A final catalog of the 165 new XMM-Newton sources, including 8 new extended objects, has been created. Source variability is a good explanation for several moderately bright objects detected within the Chandra FOV.

Among the new sources 13 were only detected in the hard band and 46 only in the soft band. Some of the soft sources detected in the diffuse X-ray region surrounding the two prominent bright extended objects on the eastern edge of the observed field may be spurious due to source confusion. The rest of the 106 sources detected in all the bands.

To derive the energy flux from the observed count rate for the (0.5–2), (2–10) and (4.5–10) keV bands, we have assumed an energy conversion factor corresonding to a power law model with the $\Gamma = 2$, which is commonly used in the XMM-Newton data analysis, since it represents well the majority of the detected sources (see Table. 2.1 for the ECF in different bands). The energy fluxes were computed separately in the soft and hard bands with assumption that the flux in the 2–10 keV band is an extrapolation

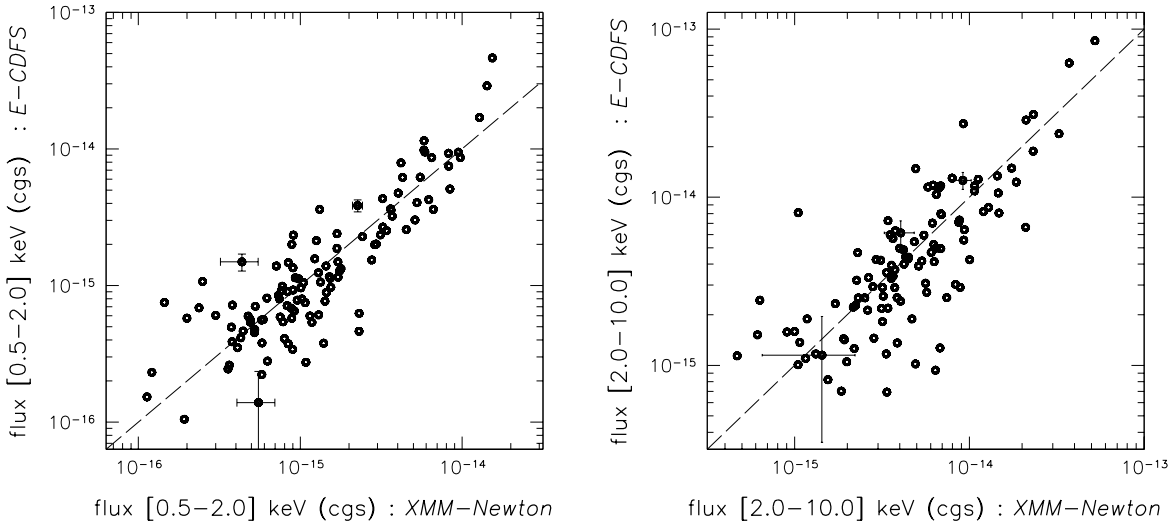

Figure 2.6: X-ray fluxes in the (0.5–2.0) and (2.0–10.0) keV: Extended-CDFS (Lehmer et al. 2005) versus XMM-Newton results (source detection catalog). Several representative error bars are plotted. The energy conversion factors correspond to $\Gamma = 1.4$. *The dashed lines are lines of equal fluxes.*

from the counts in the 2–4.5 keV band.

We also cross-correlated our new XMM sources with those from the Extended CDFS catalog (Lehmer et al. 2005) using a match radius of 6 arcsec. We found good agreement between source positions from the two datasets (similar to the results from the 1 Ms source catalog). In Fig. 2.6, we present a comparison between the soft and hard fluxes derived from these two catalogs for the 125 overlapping sources. In comparison with the 1 Ms catalog (Fig. 2.4), we observed a much larger scatter in the fluxes between the different datasets. This can be explained by a combination of three factors: 1) the large off-axis angle of the sources in both surveys affects the measured count rates and, as a result, the derived fluxes, 2) there could be source variability between the two different observation epochs, and 3) in our flux determination we assumed a spectral slope of Γ =1.4 for all sources, while Lehmer et al. (2005) determined spectral slope on a source-by-source basis, calculating the effective photon index from a band ratio (i.e. ratio of counts between the hard and soft band). While the Γ values range from 0.28 to 2.89, the average value is close to the Γ =1.4, therefore we decided to use this value instead of Γ =2. The same approach (deriving the effective photon index from a band ratio) was used by Alexander et al. (2003) for the creation of the CDFN and CDFS catalogs and flux calculations; comparison between their results and fluxes from catalog by Giacconi et al. (2002) shows a noticeable scatter in measured fluxes, especially in the hard band.

The catalogue of the new XMM-Newton X-ray sources (excluding the extended sources from Table 2.2) is given in Table 2.3. We report in the first column the unique

source number and in columns 2 and 3 the X-ray source coordinates (J2000). The X-ray flux is given in three different bands (0.5–2), (2–10) and (5–10) keV in columns 4, 5 and 6. The E-CDFS ID (if any) is presented in column 7. The last three columns show the available redshift information. New XMM sources have no spectroscopic identification yet, but a database with medium-band photometric redshifts from the Combo-17 catalog is available (Wolf et al. 2004). We crosscorelated this catalog with the new XMM sources and found 30 identifications. Most of our new objects are located at large off-axis angles, therefore we choose a radius of 6 arcsec for cross-identification. We expect to have at most one spurious identification out of 165 new XMM sources, for this search radius and up to R_{mag}=20. If the object is classified as a QSO in the Combo-17 catalog, we relax the limit to $R_{mag} \leq$20.

Fig. 2.1 shows the XMM image obtained in the full 0.5–10 keV band with the Chandra and additional new XMM source positions overplotted.

2.3 X-ray colour-colour diagrams

It is possible to derive an additional useful information about the nature of X-ray sources from X-ray colours represented by hardness ratios. The colour-colour diagrams are especially important when the signal-to-noise ratio is not high enough for spectral analysis and/or when optical identification is not available (e.g. Della Ceca et al. 1999, Hasinger et al. 2001).

From the count rates in our three energy band we calculated a hardness ratio for each source detected in our field using the standard formula $HR = (H - S)/(H + S)$, where H and S correspond to counts in the harder and softer energy bands, respectively. During our work we used 0.5–2, 2–4.5 and 4.5–10 keV energy bands.

Fig. 2.7 shows the X-ray colour-colour diagram with different symbols for various source classes identified in the CDFS superposed on spectral model[2] grids for absorbed power law spectra with different values of slopes and absorption. For clarity we plotted only sources with reasonably small errors in the HR (see caption). As already found by Hasinger et al. (2001) and della Ceca et al. (2004), type-1 AGN populate a narrow, relatively soft range in the diagram, consistent with a photon index of $\Gamma \sim 2$ and typically low apparent absorption column densities (log ($N_{\rm H}$) <21.5 cm^{-2}), while type-2 AGN scatter over a much wider area, and tend to have larger hardness ratios (especially in HR1), corresponding to larger intrinsic absorption values. A comparison of the source colours with the underlying model grids shows that the hardening is mainly due to apparent absorption column densities of $N_{\rm H}$ >21.5 cm^{-2} on top of relatively soft spectra and not due to intrinsically hard power law indices. Galaxies in their HR properties are closer to type-1 than to type-2 AGN, but in a few cases we detected quite hard objects. However, some of the sources (putative type-2 AGN) fall outside the grids for simple power law plus absorption models, showing quite hard colors in the hard bands, but hardness ratios consistent with unabsorbed sources in the soft band (HR2> 0.1 and HR1< −0.1, respectively). Colours of such sources are

[2]folded through the instrumental response of pn+MOS1+MOS2

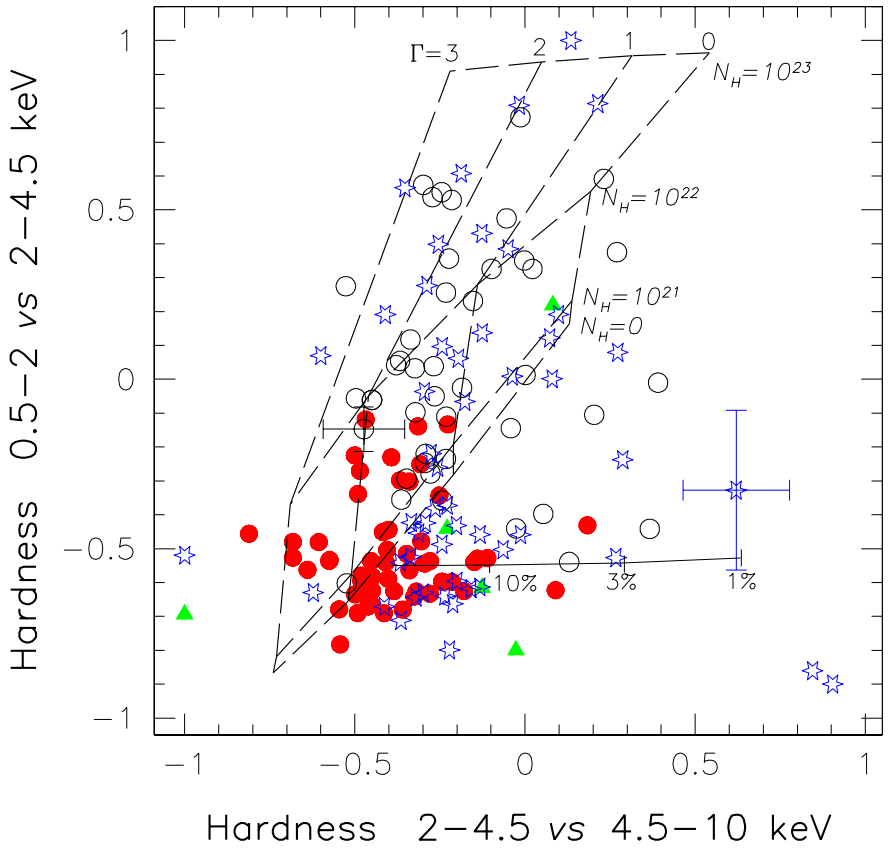

Figure 2.7: The X-ray colour-colour diagram for all identified sources in the CDFS. The symbols refer to different classes of objects: open black circles are type-2 AGN, filled red circles are type-1 AGN, and green triangles are galaxies and/or cluster/groups of galaxies. In addition, the new XMM-Newton sources, marked with stars, are overplotted. Two representative error bars are shown; for clarity only sources with HR errors less than 0.25 are plotted. The grid lines give the expected hardness ratios for two spectral models simulated using XSPEC: 1) power law models with photon indices Γ*=0, 1, 2, 3 and intrinsic neural hydrogen absorption (in the observed frame) of log* $N_{\rm H}$ *= 0 (or Galactic), 21, 22, 23 (dashed lines); 2) The reflection or leaky absorber model with* Γ *=1.7 and intrinsic absorption of* $N_{\rm H}$ *=*10^{24} *cm*$^{-2}$ *(solid line). The ticks along the line indicate the unabsorbed flux (in percentages).*

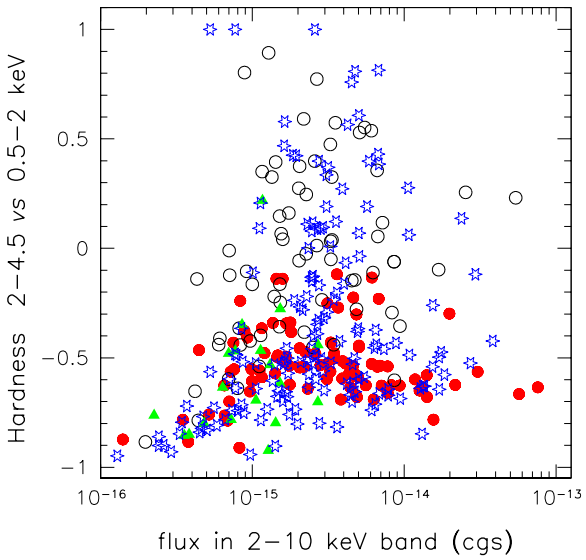

Figure 2.8: X-ray colour-flux diagram of all sources detected in CDFS field. The X-ray flux in the 2–10 keV band is plotted versus hardness ratio (2–4.5 keV vs 0.5–2 keV). The type-1 AGN are confined in the small region, as opposed to type-2 AGN which are spread over a much broader area with high hardness ratios. Symbols are as in Fig. 2.7.

consistent with the colours of heavily absorbed low redshift sources with some fraction (1–30%) of unabsorbed flux leaking out (solid line in Fig. 2.7). As was shown recently by Guainazzi, Matt & Perola (2005), bright, local Compton-thick Seyfert–2 galaxies populate the same area in the colour–colour diagram. This is probably due to the softening of intrinsically absorbed continua at higher redshifts, so that these objects shift to a different place in the colour–colour diagram.

By using significantly larger samples of AGN, like for example the COSMOS field (Hasinger et al. 2006, in preparation), all of these trends become even more obvious. Furthermore, the large solid angle coverage of the COSMOS field allows the identification and statistical study of these heavily absorbed sources with the soft components, which are probably the most absorbed objects in the field.

Analysis of the X-ray colour versus X-ray flux diagrams give possibility to see clear discrepancy between different classes of X-ray objects as well. In the Fig. 2.8 we present X-ray colour-flux diagram (HR 2–4.5 versus 0.5–2 keV as a function of the flux calculated in the 2–10 keV band) of all sources detected in our survey. In this diagram in some cases the HR and flux might be affected by source confusion, however it is clear that the type-1 AGN and most of the galaxies cluster around HR ~ -0.6, but the type-2 AGN show a large range of HR from -0.2 to $+1$ without any evident trend.

Such a marked separation between the two AGN population in the different types

of X-ray colour diagrams was already noticed in the deep survey in the Lockman Hole field (see Hasinger et al. 2001 and Mainieri et al. 2002) and explained well by differences in the absorption column density for the type-1 and type-2 AGN.

Since a large number of the X-ray sources in the CDFS have been identified spectroscopically, we can infer preliminary classifications of the new XMM sources based on their colour-colour and colour-flux diagrams. In Fig. 2.7 and Fig. 2.8 we overplotted our new X-ray catalog with previously identified CDFS sources. As was expected, the newly detected sources do not differ significantly in their HR properties from known samples and follow the same trend observed already in different surveys. The distribution of sources in both diagrams show that up to 70% of the new XMM objects overlap with the HR area corresponding to type-1 AGN. This result implies that most of the new XMM sources occupying this HR region are type-1 AGN, with a fraction of normal galaxies and low absorption type-2 AGN. Moreover, the main conclusion from our analysis is that the new X-ray sample is similar in general HR properties to previously identified CDFS sources, and most likely has an equal fraction of type-1 to type-2 AGN as well.

To test this, we selected two random objects, one from the 'type-1' and one from the 'type-2' region on the colour-colour diagram. We extracted and analysed spectra for these objects, which indicate that these classifications are indeed correct, showing the former as unabsorbed and the latter as absorbed AGN (see Fig. 2.9).

2.4 Conclusions

The 370 ksec XMM-Newton observation of the CDFS subtends a solid angle of 0.223 deg^2 and reach the flux limit of 1×10^{-16} and 9×10^{-16} erg cm^{-2} s^{-1} in the 0.5–2 and 2–10 keV bands, respectively. We detected 363 sources, from which 15 are extended,and 165 are new sources detected only with XMM. We compared the source positions and fluxes from our catalogue with the values catalogued from the Chandra observations of the same field (Giacconi et al. 2002 and Lehmer et al. 2005). We found an excellent agreement in the source position ($\sim$ 2 arcsec) and reasonable agreement in the derived flux values. The cumulative number counts in each energy band are consistent with previous Chandra 1 Ms results. In addition, we analysed colour-colour and colour-flux diagrams for our sources. Finnaly, in this chapter, we also presented source catalogs for extended and point objects in our field.

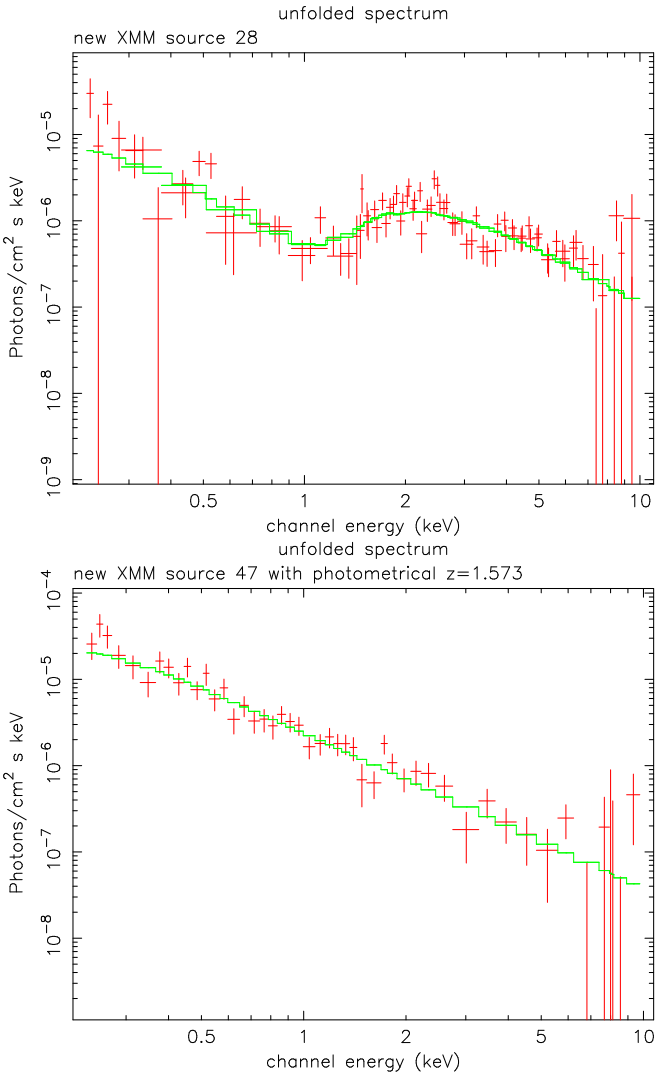

Figure 2.9: The two representative unfolded model spectra of the new detected XMM objects in the CDFS. For the new XMM sources we used the coordinates of the objects, RA and DEC from the source detection process. Top: XMM ID 28. This object has no redshift information and is located in the colour-colour diagram in the region where we expected to have absorbed objects. The most simple fit with absorbed power law shows that spectrum requires an additional component corresponding to the soft excess (modelled latter with a scattering or partial covering model `pcfabs`*). The spectral components (not corrected for redshift) are* $\Gamma = 2.09^{+0.07}_{-0.09}$ *and* $N_{\rm H} = 2.31^{+0.20}_{-0.19} \times 10^{22}$ *cm*$^{-2}$*. The covering fraction of the absorber was* $0.96^{+0.01}_{-0.01}$*. The model fluxes in the soft and hard bands are 2.81* $\times 10^{-15}$ *erg cm*$^{-2}$ *s*$^{-1}$ *and 2.58* $\times 10^{-14}$ *erg cm*$^{-2}$ *s*$^{-1}$*, respectively. The results of spectral analysis suggest what this object is type-2 AGN.*
Bottom: XMM ID 47. This object is outside MOS FOV and only the pn spectrum is available. Colour-colour diagrams suggested that this object most probably is unabsorbed type-1 AGN. This objects has a clear counterpart from Combo-17 (classified by them as a QSO) with $R_{mag} = 21.5$ *and* $z_{phot} = 1.573$*. The X-ray spectrum shows no absorption and* $\Gamma = 1.81^{+0.08}_{-0.08}$*. The fluxes are 5.26* $\times 10^{-15}$ *erg cm*$^{-2}$ *s*$^{-1}$ *and 8.35* $\times 10^{-15}$ *erg cm*$^{-2}$ *s*$^{-1}$ *(soft and hard band, respectively). Luminosities at given redshift in the soft and hard band are 6.22* $\times 10^{43}$ *erg s*$^{-1}$ *and 1.16* $\times 10^{44}$ *erg s*$^{-1}$*. All spectral properties correspond to type-1 QSO.*

Table 2.3: X-ray catalogue of the new XMM sources. We also give the corresponding ID numbers from the E-CDFS survey and the distance in arcsec from our X-ray source. For sources which have the optical counterparts from Combo-17 catalog (Wolf et al. 2004), we present the corresponding redshift (with errors), optical class and distance in arcsec from the X-ray source. Fluxes given in units of erg cm^{-2} s^{-1}.

XID	RA (J2000)	Dec (J2000)	Flux [0.5-2]	Flux [2-10]	Flux [5-10]	E-ID	dist	z_{phot}	class	dist
16	03:32:11.519	-27:37:27.64	1.4E-14	2.7E-14	1.9E-14	321	2.3	1.574 ±0.093	QSO	2.5
17	03:32:28.407	-27:35:38.38	1.5E-14	3.8E-14	2.7E-14	385	2.5	0.677 ±0.044	Galaxy	2.5
18	03:31:45.158	-27:54:36.59	9.2E-15	1.3E-14	1.0E-14	155	1.2	0.634 ±0.008	QSO	1.1
19	03:31:49.426	-27:43:20.89	6.0E-15	6.4E-15	4.3E-15	184	2.0			
20	03:31:35.704	-27:51:36.04	9.1E-15	1.3E-14	1.1E-14	96	1.7	1.630 ±0.010	QSO	1.5
28	03:32:42.464	-27:38:16.94	2.8E-15	2.4E-14	2.6E-14	437	2.4			
33	03:33:12.548	-27:55:51.83	6.2E-15	7.9E-15	4.6E-15	611	0.9			
39	03:33:23.087	-27:46:17.00	4.9E-15	1.1E-14	9.4E-15	681	1.7			
41	03:31:39.863	-27:41:59.74	4.1E-15	1.5E-14	1.3E-14	118	3.1			
43	03:32:27.176	-28:01:25.43	5.7E-15	7.8E-15	5.8E-15	381	1.3	0.539 ±0.014	Galaxy	1.3
46	03:31:50.815	-27:41:17.45	3.9E-15	2.8E-15	2.5E-15	192	2.6	0.649 ±0.008	QSO	2.6
47	03:33:32.653	-27:49:08.74	8.1E-15	1.5E-14	1.0E-14	728	1.6	1.573 ±0.005	QSO	1.6
53	03:33:09.684	-27:56:14.31	3.5E-15	4.4E-15	1.1E-15	596	0.4	2.540 ±0.008	QSO	0.4
58	03:33:20.833	-27:47:55.74	5.1E-15	9.7E-16	1.5E-15	669	0.2	0.138 ±0.005	Galaxy	0.3
59	03:32:20.370	-28:02:15.80	7.9E-15	9.4E-15	3.2E-15	358	1.0	1.635 ±0.013	QSO	1.4
61	03:33:20.436	-27:49:09.72	4.3E-15	1.4E-15	2.1E-16	664	1.9	0.139 ±0.005	Galaxy	2.2
63	03:33:20.930	-27:39:11.79	9.4E-15	1.4E-14	4.5E-15	670	2.0			
66	03:33:10.562	-27:57:49.34	5.3E-15	6.9E-15	6.3E-15	601	1.2	1.602 ±0.014	QSO	1.3
70	03:32:58.975	-27:36:12.41	6.4E-15	6.1E-15	2.2E-15	517	2.8	1.348 ±0.018	QSO	2.9
74	03:32:12.060	-27:59:59.28	2.2E-15	6.5E-15	5.8E-15	324	1.1			
78	03:32:53.068	-27:39:03.50	2.2E-15	4.7E-15	5.9E-15	493	1.9			
79	03:31:43.162	-27:54:06.26	9.4E-16	1.1E-14	8.3E-15	136	1.2			
83	03:33:22.648	-27:45:37.44	2.7E-15	6.4E-15	4.7E-15	677	2.1			
84	03:32:28.628	-27:36:16.48	1.5E-15	1.1E-14	1.0E-14	386	1.9			
87	03:31:51.009	-27:57:16.98	2.8E-15	4.2E-15	4.3E-15	193	1.2			
89	03:32:40.318	-27:35:16.15	3.0E-15	4.6E-15	5.0E-15	430	2.3	2.106 ±0.010	QSO	2.0
91	03:31:40.086	-27:47:48.97	1.6E-15	2.6E-15	2.5E-15	120	2.0			
92	03:31:33.338	-27:48:19.66	2.2E-15	3.0E-15	2.4E-15	85	1.5			
95	03:33:09.084	-27:58:27.46	3.5E-15	8.8E-15	8.3E-15	588	0.7	2.539 ±0.004	QSO	1.0
99	03:32:08.965	-27:58:30.22	4.7E-16	6.8E-15	8.8E-15	307	1.7			
100	03:33:19.459	-27:49:50.62	1.7E-15	4.9E-15	4.1E-15	659	1.9			
101	03:31:54.366	-27:56:50.85	1.5E-15	3.8E-15	2.9E-15	220	1.2			
102	03:33:26.140	-27:48:32.08	3.6E-15	4.7E-15	1.9E-15	702	2.7	0.616 ±0.113	QSO	2.3
103	03:32:32.065	-28:03:10.35	1.2E-14	1.7E-14	–	398	1.0	1.966 ±0.013	QSO	1.0
105	03:31:38.398	-27:53:35.77	2.3E-15	4.6E-15	2.9E-15	114	2.1			
114	03:32:26.547	-27:35:03.56	3.3E-15	5.5E-15	4.7E-15	376	1.7			
116	03:33:00.438	-27:34:58.42	4.0E-15	4.5E-15	1.2E-15	529	2.2			
124	03:31:34.257	-27:44:35.68	1.4E-15	1.7E-15	1.2E-15	90	2.8			
125	03:31:52.042	-27:41:48.51	1.0E-15	2.5E-15	2.7E-15	206	3.5			
127	03:33:25.454	-27:48:58.54	2.0E-15	1.9E-15	5.6E-16	698	3.8			
133	03:32:14.642	-27:59:10.14	1.1E-15	2.3E-15	5.8E-16	338	1.5			
134	03:33:22.647	-27:55:23.76	3.1E-15	7.4E-15	1.0E-14	678	1.8	1.647 ±0.013	QSO	1.9
135	03:32:00.763	-27:35:58.68	3.1E-15	5.0E-15	2.9E-15	254	2.3			
136	03:31:40.907	-27:44:36.46	6.9E-16	5.0E-15	1.8E-15	124	1.8			
138	03:31:47.208	-27:55:14.77	7.4E-16	4.1E-15	4.1E-15	166	1.8			
141	03:33:14.572	-27:42:24.88	4.2E-16	6.7E-15	7.4E-15	624	1.9			
142	03:32:13.611	-27:36:10.56	1.7E-15	2.4E-15	2.1E-15	333	3.9			
145	03:31:44.885	-27:45:41.71	9.7E-16	8.8E-16	5.9E-16	154	2.2			
146	03:32:39.987	-27:39:35.19	1.9E-16	4.2E-15	2.9E-15	427	2.0			
147	03:32:35.271	-28:00:42.05	1.4E-15	1.6E-15	1.5E-15	408	1.4			
149	03:31:52.009	-27:56:51.65	4.4E-16	3.6E-15	5.9E-15	201	3.4			
150	03:31:34.217	-27:48:35.42	7.5E-16	1.1E-15	1.2E-15	0				
151	03:31:46.583	-27:45:55.47	5.6E-16	2.3E-15	1.8E-15	162	2.8			
153	03:31:31.052	-27:54:12.85	1.7E-15	5.0E-15	3.0E-15	71	1.8			
154	03:32:09.700	-27:59:38.74	1.2E-15	2.9E-16	1.2E-16	312	1.0			
160	03:33:23.623	-27:44:40.68	1.3E-15	2.8E-15	1.1E-15	689	2.2			
162	03:32:32.285	-28:03:28.98	7.9E-15	1.7E-14	–	400	0.8	1.231 ±0.011	QSO	0.7

Table 2.3: Continued

XID	RA (J2000)	Dec (J2000)	Flux [0.5-2]	Flux [2-10]	Flux [5-10]	E-ID	dist	z_{phot}	class	dist
165	03:32:17.892	-27:37:01.12	8.9E-16	3.0E-15	2.4E-15	350	3.4			
166	03:33:24.775	-27:48:44.75	9.2E-16	2.5E-15	1.1E-15	694	1.6			
168	03:33:25.034	-27:43:13.14	1.1E-16	6.8E-15	1.5E-14	695	0.8			
169	03:32:04.276	-27:56:50.18	7.1E-16	1.4E-15	6.6E-16	275	2.3			
170	03:31:49.121	-27:57:11.88	1.5E-15	1.1E-15	–	180	0.1			
171	03:32:36.231	-27:35:22.57	8.5E-16	5.1E-15	3.9E-15	411	1.7			
172	03:31:52.159	-27:54:56.27	8.1E-16	4.5E-16	3.8E-16	208	1.6			
178	03:33:03.329	-27:59:22.86	1.6E-15	3.3E-15	5.3E-15	547	1.1			
179	03:33:29.047	-27:43:56.59	1.6E-15	2.9E-15	4.3E-15	715	2.3			
181	03:33:22.143	-27:49:24.83	1.0E-15	2.1E-15	–	675	2.1			
183	03:33:19.978	-27:48:26.24	8.6E-16	5.8E-16	–	0		0.138 ±0.006	Galaxy	4.3
185	03:31:40.100	-27:56:22.05	1.4E-15	2.4E-15	1.6E-15	121	1.1			
186	03:32:13.340	-27:57:54.23	3.3E-16	3.1E-15	1.8E-15	329	1.8			
188	03:33:20.014	-27:53:38.17	7.9E-17	4.8E-15	6.5E-15	662	2.7			
192	03:32:07.085	-27:58:05.22	3.8E-16	2.9E-15	2.5E-15	0				
194	03:33:16.807	-27:52:15.92	3.5E-16	3.9E-15	1.6E-15	637	0.5			
196	03:31:50.147	-27:58:19.57	3.9E-16	5.9E-15	4.9E-15	188	2.0			
198	03:33:08.709	-27:41:37.44	8.1E-16	1.6E-15	4.0E-15	585	1.2			
200	03:32:56.467	-27:58:46.72	8.6E-16	1.4E-15	3.0E-15	504	1.5	0.154 ±0.008	Galaxy	1.5
201	03:32:51.541	-27:58:42.77	7.1E-16	1.7E-15	1.0E-15	485	0.3			
203	03:31:30.546	-27:51:46.93	8.7E-16	4.0E-15	1.4E-15	67	3.2			
204	03:31:48.290	-27:56:49.63	8.7E-16	2.7E-15	2.2E-15	174	0.7			
205	03:31:54.053	-27:58:21.29	5.0E-16	3.3E-15	4.3E-15	219	1.6			
206	03:33:00.439	-27:58:51.89	1.3E-15	1.3E-15	1.5E-15	527	2.4			
209	03:33:02.963	-27:43:27.29	5.5E-16	7.8E-16	6.4E-16	0				
218	03:32:31.053	-27:32:36.02	6.1E-16	5.7E-15	9.9E-15	0				
220	03:31:46.134	-27:57:08.23	1.3E-15	2.5E-15	3.9E-16	158	0.7			
222	03:33:11.041	-27:43:29.53	7.5E-16	1.3E-16	2.1E-16	604	0.4			
224	03:32:25.720	-28:00:47.97	6.0E-16	2.2E-15	1.9E-15	372	1.4			
225	03:31:54.732	-27:39:23.13	5.0E-16	2.5E-15	–	224	0.5			
227	03:32:04.479	-28:04:28.52	5.6E-15	3.6E-15	9.8E-15	276	3.4			
231	03:32:20.601	-27:58:37.50	6.3E-16	3.3E-16	–	0		0.136 ±0.005	Galaxy	1.4
232	03:33:12.518	-27:52:35.33	–	2.6E-15	4.8E-15	612	3.7			
237	03:33:17.911	-27:53:32.70	7.2E-16	2.4E-16	1.4E-15	650	3.9			
239	03:32:46.548	-27:59:42.10	3.7E-16	2.3E-15	3.9E-15	459	0.5			
240	03:32:26.044	-27:37:14.53	5.1E-16	2.5E-15	–	373	2.6			
241	03:33:17.792	-27:57:07.05	1.1E-15	1.5E-15	2.1E-15	648	1.6			
242	03:31:58.088	-27:54:27.70	3.6E-16	3.7E-16	2.2E-15	0				
244	03:33:22.856	-27:49:59.21	8.9E-16	4.2E-17	–	0				
245	03:31:35.918	-27:54:46.60	8.5E-16	3.6E-15	4.3E-15	97	3.6			
246	03:33:22.379	-27:55:00.94	5.6E-16	2.1E-15	4.5E-15	676	5.3			
250	03:31:55.402	-27:38:26.15	8.0E-16	8.5E-16	1.8E-15	227	2.9			
251	03:31:44.376	-27:56:36.87	8.8E-16	3.1E-15	2.4E-15	150	1.6			
252	03:33:20.514	-27:40:59.87	8.5E-16	6.6E-16	4.8E-15	665	2.6			
253	03:31:52.121	-27:39:37.29	2.4E-16	3.1E-15	2.5E-15	207	2.0			
256	03:32:49.457	-27:58:13.32	2.9E-16	2.3E-15	9.5E-16	473	0.6			
257	03:32:29.177	-28:01:46.55	1.9E-16	5.0E-15	4.9E-15	388	1.6			
265	03:33:16.437	-27:50:38.15	5.7E-16	4.7E-16	–	634	3.2	0.090 ±0.035	Galaxy	1.6
267	03:33:03.705	-27:37:22.86	8.7E-16	3.4E-15	2.6E-15	551	2.2			
268	03:33:12.288	-27:46:37.60	4.4E-16	7.1E-16	–	0				
270	03:33:32.047	-27:54:02.73	6.8E-15	–	–	0				
271	03:33:26.537	-27:51:03.66	5.2E-16	2.5E-15	–	0				
272	03:31:40.016	-27:39:17.85	9.8E-16	1.7E-15	4.2E-15	119	0.8	2.179 ±0.078	QSO	0.6
275	03:31:49.032	-27:52:25.11	3.4E-16	7.7E-16	–	179	3.7			
278	03:33:05.555	-27:37:46.93	7.5E-16	4.6E-16	1.1E-15	561	3.3			
279	03:31:43.731	-27:38:40.89	8.0E-16	1.7E-15	3.6E-15	0				
280	03:31:42.423	-27:55:44.71	6.0E-16	2.7E-15	2.0E-15	131	3.3			
281	03:31:44.580	-27:45:20.54	–	7.7E-16	5.0E-15	152	1.6	0.232 ±0.020	Galaxy	1.5
282	03:31:35.488	-27:56:06.05	1.3E-15	1.7E-15	4.2E-15	95	2.5			
283	03:33:18.195	-27:46:50.66	6.8E-16	–	1.2E-16	0				
284	03:32:10.907	-27:34:59.16	8.5E-16	5.0E-16	1.1E-15	0				
285	03:33:03.301	-27:53:07.40	4.3E-16	8.7E-16	1.3E-15	546	0.8			
286	03:31:51.358	-27:58:58.63	3.7E-16	2.8E-15	5.5E-15	195	3.4			

Table 2.3: : Continued

XID	RA (J2000)	Dec (J2000)	Flux [0.5-2]	Flux [2-10]	Flux [5-10]	E-ID	dist	z_{phot}	class	dist
288	03:33:34.677	-27:52:55.57	8.4E-16	2.7E-15	1.7E-14	0				
289	03:33:29.570	-27:48:47.17	8.1E-16	1.6E-15	8.0E-16	717	2.8			
290	03:31:58.797	-27:36:26.07	9.7E-17	4.5E-15	7.4E-15	248	5.7			
291	03:33:15.629	-27:38:04.76	1.2E-15	2.6E-15	2.4E-16	629	2.9			
295	03:32:48.512	-28:00:07.16	1.0E-15	–	–	467	0.4			
296	03:31:49.644	-27:48:49.74	4.5E-16	–	–	0				
298	03:33:27.159	-27:45:21.71	4.8E-16	1.9E-15	4.9E-15	705	4.0			
302	03:33:07.732	-27:55:55.39	1.9E-16	2.8E-15	8.1E-16	578	0.2			
303	03:33:21.225	-27:41:38.18	7.7E-16	7.3E-16	–	674	1.0			
304	03:31:30.482	-27:48:45.31	5.0E-16	2.4E-16	4.1E-15	0				
308	03:33:05.630	-27:36:30.38	9.6E-16	2.7E-15	3.4E-15	0				
309	03:33:29.795	-27:51:13.88	3.3E-16	2.5E-15	6.1E-15	718	4.2			
310	03:33:14.807	-27:57:49.74	1.2E-15	1.5E-15	1.8E-15	625	0.8	2.790 ±0.012	QSO	1.0
312	03:32:11.426	-27:36:24.26	3.1E-16	2.5E-15	7.3E-16	0				
314	03:33:00.486	-27:36:41.51	8.5E-16	8.0E-16	–	0		0.271 ±0.019	Galaxy	1.1
316	03:32:04.683	-28:04:12.48	2.6E-15	6.6E-15	1.3E-14	0				
317	03:32:54.518	-27:58:39.73	1.2E-16	1.9E-15	3.9E-15	499	4.3			
319	03:33:13.610	-27:38:27.52	2.3E-16	3.2E-15	5.4E-15	616	5.1			
321	03:32:09.661	-27:35:25.85	7.7E-16	2.6E-16	7.4E-15	0				
322	03:32:32.720	-28:02:27.33	1.6E-15	–	–	0		0.145 ±0.004	Galaxy	4.0
324	03:33:12.661	-27:45:45.87	4.1E-16	–	2.7E-16	614	1.7	0.242 ±0.005	Galaxy	1.5
327	03:31:56.046	-27:39:44.82	4.7E-16	3.5E-16	2.9E-16	230	2.3			
328	03:32:06.410	-27:38:54.01	4.6E-16	–	–	296	4.3			
329	03:31:52.067	-27:48:12.03	1.5E-16	1.1E-15	1.7E-15	0				
330	03:31:48.231	-27:38:04.67	5.3E-16	1.1E-15	2.9E-15	175	2.5			
331	03:32:58.735	-27:42:35.80	2.0E-16	1.0E-15	2.6E-15	0		0.307 ±0.021	Galaxy	1.0
332	03:31:37.963	-27:55:32.97	5.6E-16	5.6E-16	7.4E-15	109	1.9			
333	03:31:31.740	-27:51:23.30	3.6E-16	2.7E-15	2.4E-15	75	1.6			
334	03:31:59.478	-27:46:53.76	2.6E-16	2.6E-17	2.9E-16	0				
335	03:31:53.936	-27:47:56.25	1.2E-16	1.1E-15	3.6E-16	0				
336	03:32:40.556	-27:44:27.63	–	5.3E-16	2.2E-15	0				
337	03:32:06.502	-27:59:56.51	1.3E-16	2.0E-15	1.5E-15	294	2.2			
338	03:31:46.066	-27:41:33.00	9.3E-17	1.6E-15	3.4E-15	0				
339	03:32:06.217	-27:40:23.12	3.6E-16	7.9E-16	2.0E-15	291	0.8			
340	03:32:30.049	-27:59:08.79	6.9E-17	1.6E-15	–	0				
341	03:31:44.588	-27:47:33.66	2.0E-16	–	3.1E-15	0				
342	03:32:08.930	-27:42:40.25	2.2E-15	1.9E-15	2.7E-15	0				

Chapter 3

Analysis of source spectra in the CDFS

3.1 Introduction

As was intensively discussed above, the XRB is largely due to accretion onto supermassive black holes in the center of AGN, integrated over cosmic time. Since the XRB is mostly associated with point sources, the general interest has moved to accurately constrain the physical and evolutionary properties of different classes of X-ray sources. To this aim, statistically significant samples of AGN that cover a range of redshift and luminosity from the deep and shallow surveys have been formed. This information makes the data an invaluable resource for revealing physical and evolutionary properties of AGN, and finally can be used to investigate, whether the unified model holds. Analysis of the Lockman Hole data (e.g. Mainieri et al. 2002) has also confirmed the idea that X-ray spectroscopy of a large number of sources could be very powerful method with XMM-Newton.

The CDFS sample of AGN, which we were able to create using the XMM-Newton observation, is very representative among deep surveys, allowing studies of not only the bright objects that can be detected with shallow surveys as well, but also very faint, mainly distant and obscured sources, which contribute most to the X-ray background. Among these faint obscured objects we can detected the type-2 QSO (highly obscured and luminous sources), Compton-thick objects and starburst/normal galaxies.

3.2 X-ray sample and spectra extraction

The possibility to obtain a reliable spectral fit depends on the quality of the X-ray spectrum (on the signal-to-noise ratio), which is in turn related to the total number of source photons. Therefore we used only spectra with raw number of counts larger than 100 (pn detector) in the total 0.2–10 keV band. Adding the MOS photons (starting from 80 counts for two detectors) allows us to have, finally, spectra with a minimum of ~ 200 counts for a reasonably reliable fit. With this approach, we selected a sample of 127 X-ray sources with spectroscopic or photometric identification. Fig. 3.1 shows the distribution of the pn+MOS counts for the sources in our sample.

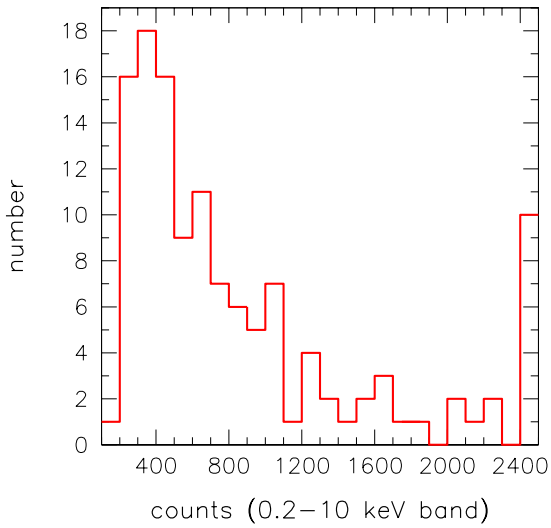

Figure 3.1: The distribution of counts (pn+MOS) in the 0.2–10 keV band for the sources in our sample. The last bin contains 10 objects with total number of counts greater than 2400: 7 objects have 4000>N>2400 counts and the 3 brightest quasars have 11281, 18767 and 27738 counts, respectively.

The spectroscopic identification from VLT follow up is presented in detail in Szokoly et al. (2004) for a total of 161 X-ray sources (out of 349). The authors used not only the optical classification based on the detection of high ionization emission lines for the determination of different source classes, but also made use of a combined classification scheme based on the optical spectrum and the X-ray properties (X-ray luminosity L_X and hardness ratio HR). We discussed this work in the Section 1.5.2. The photometric redshift information for 342 X-ray objects is presented in Zheng et al. (2004), and for some analysed sources in Mainieri et al. (2005). Zheng et al. (2004) have also extended the combined classification scheme to the rest of the objects.

In the following we will refer to type-1 (objects with broad emission lines) and type-2 (objects with high ionization narrow emission lines) AGN using the combined X-ray – optical spectroscopic classification scheme from Zheng et al. (2004). In several independent studies of spectral parameters, we also separated our objects into AGN and QSO classes using the criteria from Szokoly et al. (2004) ($L_X < 10^{44}$ erg s^{-1} and $L_X > 10^{44}$ erg s^{-1}, respectively).

Objects classified as a galaxies show in their optical spectra either unresolved emission lines consistent with H II regions or only absorption lines. These objects are star forming galaxies or Narrow Emission Line Galaxies mostly, however such optical appearance does not exclude the presence of low-luminosity AGN among these objects. Therefore we constrain our galaxy sample to objects with luminosities $L_X > 10^{42}$ erg s^{-1} in the 0.5–10 keV band in order to avoid normal galaxies and include in the analysis hidden AGN.

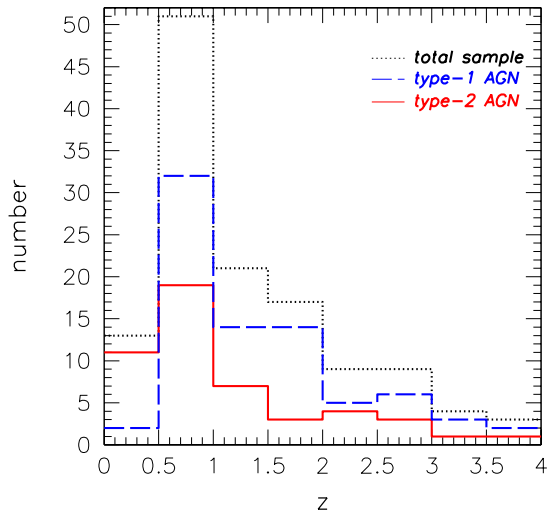

Figure 3.2: The redshift distribution of the X-ray sources in our sample. The solid and dashed lines correspond to the type-2 and type-1 AGN, respectively. The upper dotted line shows the distribution for the total sample of 127 sources. Most of the type-1 AGN, just as type-2 AGN, have z below 1 and constitute 40% of all the sources.

Finally, our complete sample includes 78 type-1 objects (including 28 type-1 QSOs), 39 type-2 objects (including 11 type-2 QSOs) and 10 galaxies.

The z distribution of the sources in our sample peaks at redshifts below 1 (Fig. 3.2), and thus the sample is representative, confirming the already remarked disagreement between the prediction from X-ray background population synthesis models (Gilli et al. 2001), with a maximum around $z \sim 1.5$, and the recent observations. Such a discrepancy was already noted for the 100 ksec observation of the Lockman Hole with XMM-Newton (Mainieri et al. 2002) and for the 1 Msec Chandra survey of the CDFS (Rosati et al. 2002).

Spectral extraction

We use an automated procedure to extract individual X-ray spectra. The `evselect` tool is used to extract the spectrum and background region, which is defined as an annulus around the source, after masking out nearby objects. We extracted the spectra of each source for pn, MOS1 and MOS2 detectors, using only events with pattern 0–4 (single and double) for the pn and 0–12 for the MOS cameras. For objects which overlap with the catalog from the 1 Ms Chandra data, positions of objects refer to Giacconi et al. (2002). In this way we are consistent with previous results and can make comparisons in spectral properties with these datasets.

All spectra have been extracted in the 0.2–10 keV band where EPIC is best calibrated. Events with nominal energy < 0.2 keV were excluded because the EPIC

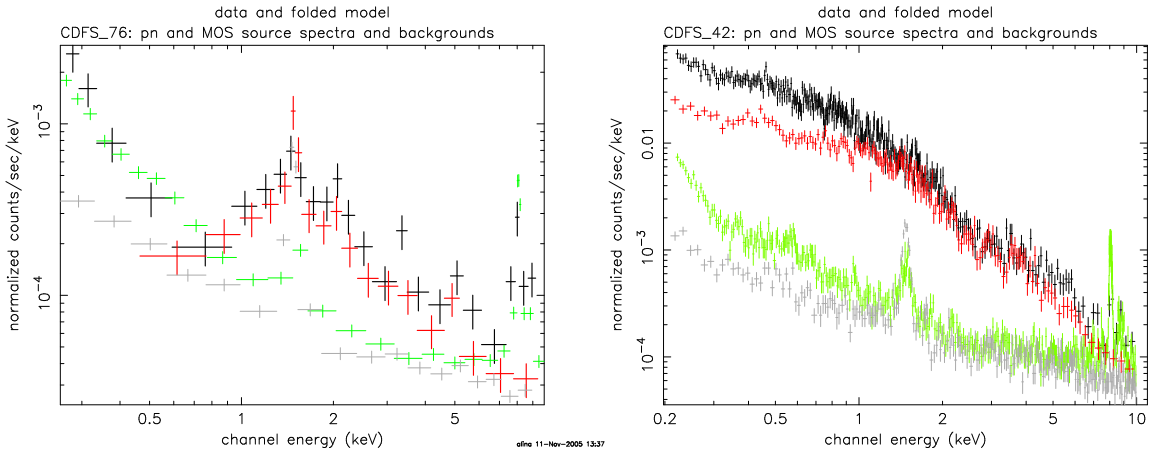

Figure 3.3: Two examples of the spectra (souce plus background, and background only) for absorbed (left) and unabsorbed (right) sources in our sample. The spectra were rebinned for display purposes. The pn and merged MOS1 and MOS2 spectra (the black and red upper points, respectively) are above the background level (shown as the green and grey points) in the analysed energy range (0.2–10 keV) for the unabsorbed object, and affected mostly only at high energies (∼ 10 keV). However, for the absorbed source the flux is strongly suppressed below 1 keV, and therefore no significant count rate above the background level was detected.

responses are uncertain at such low energies. The latest canned EPIC response matrices for our filter and mode are used for the analysis of the pn spectra (Haberl, priv. comm.), while for MOS spectra we created these files manually with the SAS task `rmfgen`. We applied the spectral correction for vignetting, taking into account that the vignetting function is energy dependent above 5 keV for the XMM-Newton mirror system which is particularly important for our objects at large off-axis angles. We create for this purpose ancillary response files (`arf`) for each of our sources using the SAS task `arfgen`.

To improve statistics, MOS1 and MOS2 source spectra were combined by summing the counts from the channels with the same nominal energy range using task `mathpha`. Background spectra were summed in the same fashion. Using the standard `FTOOLS` tasks `addarf` and `addrmf` we combined the calibration files weighting them for the exposure time of the individual detectors.

Such an approach allowed us to measure the time-average spectral properties (i.e. the flux and spectral shape), ignoring possible time variability of a source. To illustrate the quality of our spectra, in Fig. 3.3 we present two pn and merged MOS source spectra and backgrounds for unabsorbed and absorbed sources with ∼ 20000 and 800 counts in our sample.

Before spectral fitting, all spectra are binned (using the `grppha` tool) with a minimum of 20 counts per bin in order to be able to apply the χ^2 minimization technique. In this process, the background count rate is rescaled with the ratio of the source and background extraction areas.

3.3 Spectral analysis and models

We use `XSPEC` (v11.3), the X-ray spectral fitting package (Arnaud 1996), for the spectral analysis. pn and MOS data were fitted simultaneously with an appropriate model. During our analysis it was found that several objects required different pn and MOS normalisation and offsets in measured fluxes are higher than 25%. The same effect was also detected in the analysis of the Lockman Hole field sources (see Mateos et al. 2005) and is interpreted as changes in flux of the sources during the observations. This interpretation is in agreement with the study of the source variability in the CDFS during the Chandra observation (Paolillo et al. 2004). The main result from an analysis of 11 individual observations was the detection of significant variability in more than 50% of the AGN population. In the case of XMM-Newton, due to the difference in the FOV and in the position of the gaps for the pn and MOS detectors, the time averaged spectra may be also different, especially for bright variable sources whose variability is on a short timescale.

The weak signal of the faintest sources limits our ability to perform a model fit keeping all the spectral parameters free. The fits to most faint sources (less than 250 total counts) starts to be affected by to the poor statistics and as a result we obtain a large spread in all spectral parameters and sometimes even nonphysical values for the spectral slope. To avoid any possible bias introduced by the low statistics, we decided to freeze the slope of the faintest sources to the canonical value of $\Gamma = 1.8$. This value is commonly used in the analysis of the faintest objects and, from deep XMM and Chandra surveys, appears as the average value for bright/moderate objects (e.g. Mainieri et al. 2002, Mateos et al. 2005, Tozzi et al. 2005). If we freeze the power law, then we can focus on the remaining parameters, in particular the intrinsic absorption.

During our analysis, we used the F-test to measure the significance of the detection of a spectral component in the source emission. We assigned a confidence level threshold of 95% for additional components.

Initially, we fit the data with a model consisting of a power law with an intrinsic absorption component at source redshift (`zwabs`), with an additional photoelectric absorption component (`wabs`) that was fixed at the Galactic column density of 8.9×10^{19} cm^{-2} (`wabs*zwabs(po)`).

From our model fits, we computed the slope of a power law spectrum (photon index Γ), the intrinsic rest-frame column density $N_{\rm H}$, and the X-ray flux and luminosity in the 0.5–2 and 2–10 keV bands. For absorbed sources, the rest-frame luminosities have been corrected for the absorption setting to zero the $N_{\rm H}$ value in the `XSPEC` best fit model.

However, there are other spectral components that can also contribute significantly to the emission in the 0.2–10 keV energy band and, therefore, for some sources, the absorbed power law model gives a poor fit. In these cases, we introduce additional components to model: a soft excess and/or the Fe K_α complex. For the sources that required additional components, we selected the best fit model as the one that gave a significant fit improvement over the simple power law model. For this purpose we

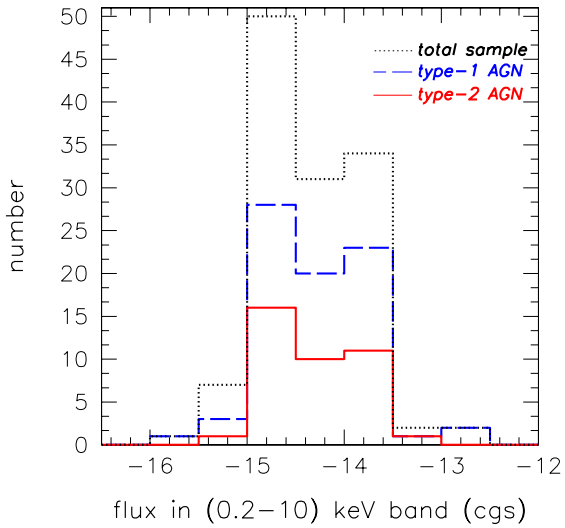

Figure 3.4: Histograms of 0.2–10 keV fluxes obtained from the best fit model (Sec. 3.3) for the whole sample of the sources and for the type-1 and type-2 AGN independently.

used the F-test, taking into account the improvement in the χ^2 value and the number of the new parameters introduced.

The usual model (see discussion in Section 1.4) for fitting a soft excess is a scattering or partial covering model. We used the `XSPEC` model `zpcfabs` which introduces in our fit a new free parameter that varies between 0 and 1: the covering fraction of the absorber. This model consists of the sum of two power law components having the same spectral index but different normalisations and absorptions. One power law is absorbed by the Galactic column density only and the other is absorbed by a high intrinsic column density (a free parameter during the fit procedure). Alternatively, it is also possible to construct the same model using the sum of two power laws with the slopes linked together (as was done in the analysis of the Chandra sources by Tozzi et al. 2005), and the resulting spectral parameters do not differ significantly from the `zpcfabs` model (Sec. 3.6).

In the cases where partial covering model was not sufficient, we used instead the blackbody model `bb` (as was necessary for three type-1 AGN). This component adds to the fit two free parameters, the temperature (in keV) and normalisation of the blackbody.

An additional component `zgauss` corresponding to the Fe K_α emission line complex also has been introduced in our analysis. Due to the poor statistics of our data, we need to fix the energy of the line to 6.4 keV (corresponding to the neutral iron line emission), with a fixed width of 0.

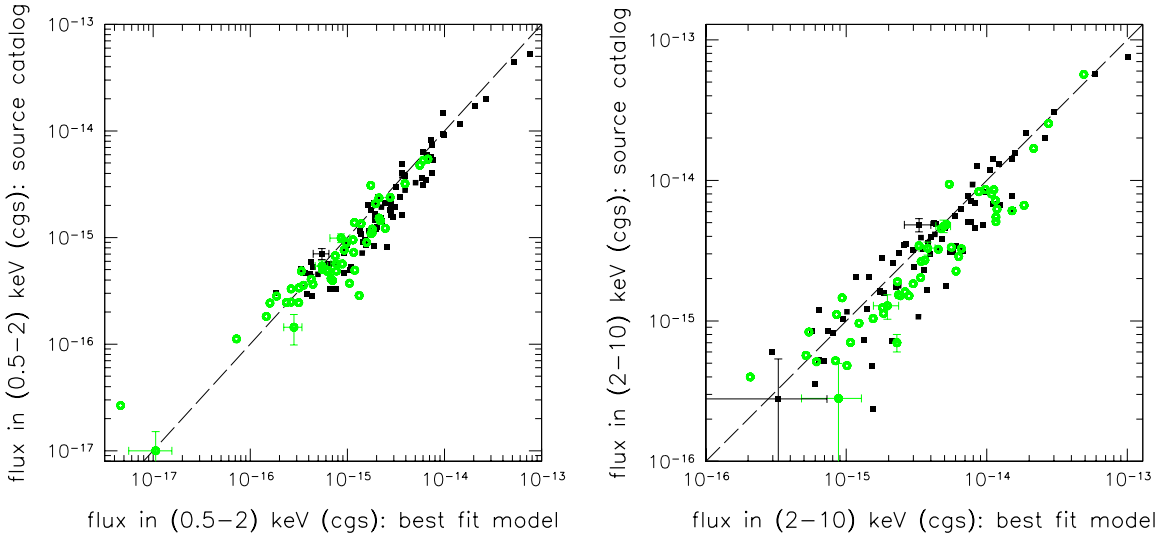

Figure 3.5: X-ray flux in the [0.5–2] and [2–10] keV: The energy fluxes computed from the observed count rate (using an energy conversion factor assuming $\Gamma = 2$) versus flux derived from the best fit model. The dashed lines are lines of equal fluxes. The black and green circles correspond to the type-1 and type-2 AGN, respectively.

3.4 Spectral parameters

The spectral analysis was performed for the sample with known redshifts, which leads to proper values of Γ and $N_{\rm H}$ in the source rest-frame. For the complete results from the analysis see Table 3.1.

In Fig. 3.4 we show the distribution in the 0.2–10 keV flux obtained from the best fit model of all the objects in our sample. We note that the two AGN types have similar flux distribution in this energy range. We conclude that our sample is not biased towards high or low flux objects, and therfore represents well both AGN classes.

We have also compared the best fit model fluxes (Table 3.1) with the catalogued values (Section 2.2). The result of this comparison is shown in Fig. 3.5. Since the catalogued fluxes were calculated assuming the same spectral slope and absorption for all sources, we would expect to see much larger scatter of points in Fig. 3.5. However, the best fit model fluxes, calculated by using the intrinsic photon index for each source, are in good agreement with the catalogued values in the soft band. That means that the power law model with a slope of Γ =2 is a good approximation for the majority of our sources, and that the influence from additional spectral components (e.g. soft excess) to the measured flux are small. However, we observed a systematic shift for type-2 AGN's hard band fluxes towards the lower values of the measured best-fit fluxes. This effect is explained by in general lower Γ (<2) for type-2 AGN at high energies due to absorption. Assuming Γ =2 for the ECF as a result overestimates the the real

source fluxes. We notice that this trend disappears when we assume lower values for the power law slope (e.g. $\Gamma = 1.4$) in calculating the catalogued fluxes.

3.4.1 Photon index

We not only want to investigate the differences between type-1 and type-2 objects, but we would also like to compare the intrinsic differences between the AGN and QSO classes. To do so, we calculated three separate arithmetic mean values for the slope: one for the AGN alone, one for the QSO alone and a third value for the combined group. In the following text, the first number presented is the combined value, with the values for the individual AGN and QSO populations presented in parentheses (AGN/QSO).

If we consider only type-1 objects with the free power law slopes, the resulting parameter for our sample of 70 sources (43 type-1 AGN and 27 type-1 QSOs) will be: Γ =1.90 (1.89/1.91). The sample of 29 type-2 objects (22 type-2 AGN and 7 type-2 QSOs) shows Γ= 1.76 (1.73/1.85). If we choose the same objects from the Chandra dataset (Tozzi et al. 2005), we obtain the following results: type-1 object have Γ= 1.81 (1.78/1.85), while type-2 objects have Γ=1.51 (1.42/1.68).

As these numbers indicate, the average photon index of identified type-2 AGN appears to be harder than that of the type-1 AGN in the Chandra and XMM surveys. The significance of this apparent effect (that type-2 AGN appear to be flatter on average than type-1 AGN) is still under discussion, since other effects may or may not contribute significantly enough to influence these values. Recent analysis of the brightest objects in the deep XMM survey on the Lockman Hole field (Mateos et al. 2005) shows the same difference between the mean spectral slopes of type-1 and type-2 AGN (1.89 ± 0.03 and 1.71 ± 0.03, respectively), implying that the significance of Γ being different for these two classes of AGN is 4σ. However, the estimation of the intrinsic dispersion of Γ in both types of AGN, using a Maximum Likelihood analysis, gave a significance for type-2 AGN being on average flatter than type-1 AGN of only 1.62σ. Therefore, using even the best quality data, we cannot reach any strong conclusion. The main difficulty for such a study is that we need proper measurements of absorption in the source spectrum, because the measured AGN continuum is most affected by this spectral component. If $N_{\rm H}$ is not very significant, the signature of absorption will be at lower energies ($<$ 1 keV), where we still have some calibration uncertainties and, in general, there are often not enough counts for a proper $N_{\rm H}$ detection (especially for faint objects). Another problem, that if we have low absorbed type-2 AGN[1] at high redshifts, the signature of the absorption will be shifted to even lower energies, outside the energy range of the detector. All of these issues combined result in the detected values of $N_{\rm H}$ tending to be lower than the real ones, and then, the flatter Γ of the fitted spectra.

[1]Note, that in some of the faint sources, the low absorption and/or flatter power law slope could be an indication of a scattering component in the type-2 AGN spectrum. The low count statistics would prevent us to detect this component, even if it would be present. As a result, a simple powerlaw fit will underestimate the intrinsic $N_{\rm H}$ and give a flatter spectral slope.

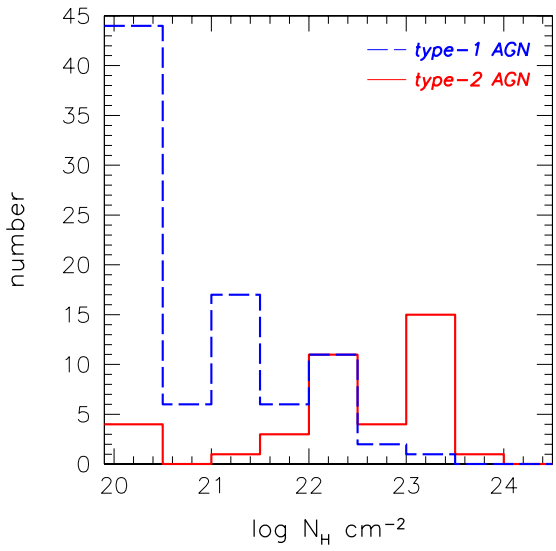

Figure 3.6: The observed distribution of absorption ($N_{\rm H}$) for the whole sample of sources. We observed the clear tendency of type-1 AGN to have a low value of absorption ($\sim$ 70% have $N_{\rm H} < 10^{21}$ cm^{-2}) in opposite to type-2 AGN which appear to be 90% absorbed.

This conclusion is supported by the results from our analysis of the brightest objects in our sample, the type-1 QSOs, and the most absorbed type-2 QSOs. We use these two groups for comparison, because the first group contains those with the best measurements of the spectral slope and the second the best $N_{\rm H}$ measurements. These give us the best overall measurements for the spectral slope without and with absorption. From this, we obtain average values of Γ for type-1 and type-2 QSOs that are quite close to each other (i.e. 1.91/1.85). .

3.4.2 X-ray absorption

We detected absorption ($N_{\rm H} \geq 10^{22}$ cm^{-2}) in 47 objects out of 127 (35%), including 14 type-1 and 31 type-2 AGN. Fig. 3.6 shows how the distributions of the intrinsic $N_{\rm H}$ values in type-1 and type-2 AGN differ. The classical and obscured AGN populations show clearly different mean values of absorption: the measured column densities in almost all absorbed type-1 AGN are between 10^{21}–10^{22} cm^{-2}, while type-2 AGN have a much wider distribution of values, with a peak about 10^{23} cm^{-2}. As was expected, the type-2 AGN in general are more absorbed than type-1 AGN, which is in good agreement with the unified model of AGN. There is a number of absorbed type-1 and unabsorbed type-2 AGN ($\sim$ 18% and $\sim$ 8% from the total number of type-1 and type-2 AGN, respectively, or about 13% of the overall sample), contradicting this model. However, some of these sources could be spuriously detected as absorbed/unabsorbed, due to the influence of background contamination, or misleadingly classified as type-

1/type-2 on the basis of their photometric properties. On the other hand, the sources with secure identification (i.e. those with better statistics, and probably no influence of the background contamination) may be explained by a difference in the physical conditions surrounding the emission regions. All these issues are going to be discussed in detail in the following subsections.

Unobscured type-2 AGN

The unabsorbed type-2 AGN/Seyferts have already been detected in X-ray observations with several X-ray satellites (e.g. Pappa et al. 2001, Panessa & Bassani 2002, Georgantopoulos & Zezas 2003, Mateos et al. 2005). If the statistics are good and no absorption is observed, then one of the good explanations for these low-luminosity sources that they are Compton-thick. If intrinsic absorption of these sources exceeds 10^{24} cm^{-2}, the optical depth for Compton scattering equals unity and the direct nuclear emission is completely blocked in both the soft and hard bands. In the cases of intrinsically bright AGN, the radiation component reflected by the cold medium, usually assumed to be produced by the far inner side of the putative obscuring torus, is strong enough, and the observed spectra will be dominated by scattered radiation without any apparent absorption.

This hypothesis was tested for the complete sample of the sources in our field by Tozzi et al. (2005). They have created a sample of 14 Compton-thick candidates (due to the weakness of the objects we have only two overlapping sources, type-2 QSO XID 202 and one of our low absorbed type-2 AGN XID 545) using the appropriate models and simulations. In our sample we found 3 unabsorbed type-2 AGN. However, only in one case we have enough statistics to confirm this result. Two other sources show indications for unabsorbed spectra, but due to the low statistics there could also be other explanations (e.g. background contamination). We also modelled our 3 type-2 AGN with `pexrav` model (Magdziarz & Zdziarski 1995) freezing all the parameters to the default, looking for the evidence that the observed spectrum is dominated by a Compton-reflection continuum, but the likelihood of this model was comparable to that of the unabsorbed power law.

Another powerful diagnostics of the nature of our objects will be comparison of the X-ray flux in the 2–10 keV band with the optical [O III]λ5007[2] emission line flux. The obtained ratio (transmission parameter) T (i.e., $T = F_X/F_{[OIII]}$) could be used to test the nuclear X-ray obscuration, due to the fact that previous studies (e.g. Bassani et al. 1999) have shown that objects with $T \leq 0.1$ are invariably Compton-thick, whereas objects with $T \geq 1$ are almost only Compton-thin/unobscured. In addition, Bassani et al. (1999) show a diagram of the EW of the iron line versus the T, which can be used to identify Compton-thick sources. However, we do not know the value of $F_{[OIII]}$ for our sources due to their high redshift (i.e. the line is shifted in the NIR region of the spectrum). In addition, we do not see any indication of a strong Fe K$_\alpha$ line, which, due to the strongly suppressed primary radiation, must be present in Compton-thick

[2][OIII] λ5007 has been frequently used as an isotropic indication of the intrinsic brightness of the sources.

sources, and in general has EW up to ∼1000 eV. Therefore, we do not find compelling evidence that these sources are Compton-thick, although the [OIII] flux needs to be measured to reach a firm conclusion.

Due to this ambiguity, it is impossible to make any strong conclusion about the origin of our unabsorbed type-2 sources. However, it is possible that the existence of this unusual type of object is the real complexity of the AGN continuum, as already indicated in detailed studies of brighter sources (e.g. Turner et al. 2000).

Obscured type-1 AGN

While the unabsorbed type-2 AGN are still quite rare objects (one or two objects per sample), the fraction of absorbed type-1 AGN is much larger. We have found 14 sources classified as type-1 AGN in our sample, using the combined classification scheme from Szokoly et al. (2004). However, we found a clear evidence for absorption in the X-ray spectra of these sources, which is more commonly detected in type-2 objects ($\sim 10^{22}$ cm^{-2}). Most of these sources have $L_X \sim 10^{44}$ ergs s^{-1}. Moreover, our sample contains 8 sources (XID 18, 61, 62, 72, 159, 209, 506, 517) which have the absorption and luminosity values that fall within the standard type-2 QSO region. However, most of these sources have photometric identification only and were classified as type-1 object using their hardness ratio properties and/or the results from multiband optical/IR images. So far, we have secure spectroscopic identifications only for 3 sources (XID 62, 68, 91), all of which are classified as BLAGN objects at z>2.5. Although, one of these sources is a BAL QSO, for which an absorption of the order of 10^{22} cm^{-2} is expected, the rest of the objects also show the similar absorption column, which is unusual for this optical type. The fraction of these absorbed sources is small (9%) comparing to the total number of detected BLAGN (32), but it becomes significant when compared with with the total number of the high-z BLAGN (z>2) in our sample (9 sources). However, our sample is statistically insignificant, and hence, it does not allow us to make a strong conclusion at this point. To study this question in detail is only possible when the results from the existing deep surveys are combined with recently conducted wide area surveys (e.g. COSMOS), which contain many more objects needed for statistical studies.

For example, similar examples of 'absorbed' type-1 AGN have been detected in several large scale surveys with XMM-Newton and Chandra. These surveys, which contain statistically significant samples of sources (e.g. Mainieri et al. 2002, Page et al. 2003, Brusa et al. 2003, Perola et al. 2004, Silverman et al. 2005 etc), have confirmed previous results obtained with the ASCA and BeppoSAX missions. Some of the luminous AGN, detected in these surveys, show both strong intrinsic X-ray absorption ($N_H > 10^{22}$ cm^{-2}) and broad optical emission lines at z > 1. The authors have found that around 6–10% of the X-ray selected BLAGN with $L_X > 10^{44}$ ergs s^{-1} have $N_H > 10^{22}$ cm^{-2}, supporting the previous evidence of a decoupling between optical and X-ray properties at high luminosities and redhifts.

This mismatch between the optical and X-ray classifications can be explained by a gas-to-dust ratio and/or the chemical composition significantly different from that of

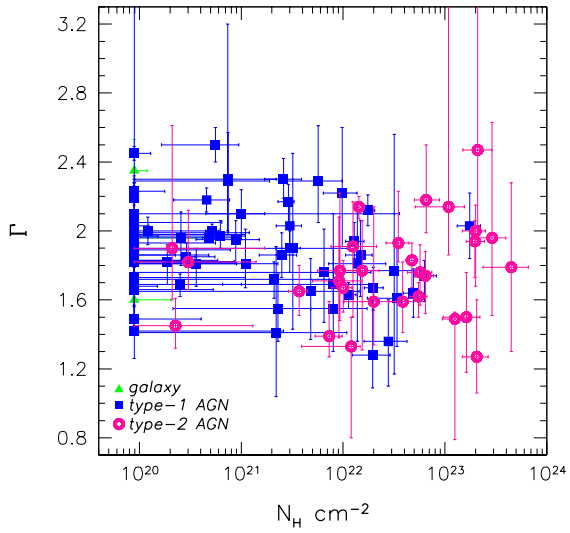

Figure 3.7: The rest-frame power law photon index Γ *vs.* $N_{\rm H}$ *for the analysed sample. Solid blue squares and open magenta circles refer to type-1 and type-2 AGN, respectively. Triangles show the galaxies.* Γ *for identified objects range from 1.4 to 2.5, with the majority of the sources clustering around 1.9.*

the Galactic interstellar gas (Maiolino et al. 2001, Akiyama et al. 2000). Briefly, for some of AGN, the nuclear extinction estimated in optical light is significantly smaller than that derived from the X-ray spectrum, because the former is caused by dust, while the latter by gas phase metals. This suggests that a dust-to-gas ratio is much smaller than the standard value obtained in the Galaxy. Indeed, recent results from an ASCA survey of an X-ray selected sample of QSO (Watanabe et al. 2004) show that for all QSOs with the absorption $N_{\rm H} > 10^{22}$ cm^{-2}, the values of dust-to-gas ratios in the circumnuclear gas are smaller than the Galactic value by a factor of $\sim$5 to $\sim$100. This could be the reason that up to $\sim$ 30% of the UV selected known QSOs show type-2 nature in X-rays. The substantial variance in the dust-to-gas ratio may be ascribed to the depletion of small grains due to the coagulation/sublimation by AGN radiation (Maiolino, Marconi, & Oliva 2001), or, alternatively, to a geometrical separation with respect to the line-of-sight between the patchy X-ray absorbing gas and dust in front of the broad line region (Weingartner & Murray 2002).

Other explanations of the absorbed type-1 AGN assume specific conditions around the black hole or intrinsic properties of the sources. For example, one of the possible explanations is that X-ray absorption occurs very close to the central engine where dust just sublimates and therefore the optical spectrum is unaffected by the surrounding material. The absorption by the host galaxy or circumnuclar starburts could also affect the X-ray regime.

Finally, from a purely empirical side, one should not forget that variability may also

play a role. One of the most convincing cases for such an interpretation is NGC 4151, which is characterized by a fairly dense and variable X-ray absorbing column. This object displayed an impressive difference in the width of the permitted lines, from very broad to very narrow. The observed line width change correlated with the changes in brightness, but without any evident correlation with the amount of absorption (Ulrich 2000, and references therein; Perola et al. 2004).

However, none of these hypotheses gives an obvious answer to the question of why the anomalous cases appear to be more common at QSO luminosities. These observed larger values of $N_{\rm H}$ could be, at least partly, explained by a selection effect, due to high redshifts of these QSOs. However, these absorbed type-1 AGN were discovered already in several deep/shallow surveys, in addition to normally detected unabsorbed type-1 QSO, and have the same statistical spectral quality. Moreover, the fraction of these absorbed sources seems to be approximately the same (about 10%) in all of these surveys. These results seem to affect, not only the understanding of physical conditions in a circumnuclear region, but also the view of the unified scheme of AGN. This suggests that the unified scheme may require at least the relaxations of the basic assumptions. One of the implications may also be that there is a real and quite sizable ($\sim$10 % from the total number of type-1 AGN) population of sources that show type-1 properties in optical/UV regime, but displays the type-2 nature in X-ray.

We find no real correlation between Γ and the intrinsic absorption column $N_{\rm H}$ density (Fig. 3.7). As was discussed in the Sec. 3.4.1, the slight systematic correlation between absorption and lower values of the continuum is mostly an systematic effect of the low statistic of our data. Taking into consideration this fact, our results confirm the idea that the clear separation between the two AGN populations is mostly due to differences in the absorption column density, not in Γ. Excluding several peculiar cases discussed above, our results are broadly consistent with the unified scheme of AGN, which links classifications based on optical spectra and properties of the X-ray spectra.

3.4.3 Dependence of Γ and $N_{\rm H}$ on the flux, luminosity and redshift

We also study a possible dependence between spectral slope and absorption on one side and redshift, flux and luminosity on the other (Fig. 3.8 – Fig. 3.11).

In order to study the dependence of $N_{\rm H}$ on X-ray flux, in Fig. 3.8 we plot the detected values of absorption as a function of the soft (0.5–2 keV) and hard (2–10 keV) fluxes. There is an obvious correlation between the absorption and the observed soft flux (especially for faint objects), unlike with the hard band fluxes. When we correct 0.5–2 keV fluxes for the effect of absorption (because the absorbed column affects the measured flux mainly in the soft band), the artificial effects that most absorbed objects have the faintest fluxes disappears. We also study the dependence between Γ and fluxes and do not find any correlation, however we again find that type-2 AGN tend to have Γ slightly lower that type-1 AGN at all flux levels.

Fig. 3.9 shows how the absorption varies with unabsorbed luminosity in the total 0.5–10 keV band. The apparent paucity of low luminosity absorbed sources is due to

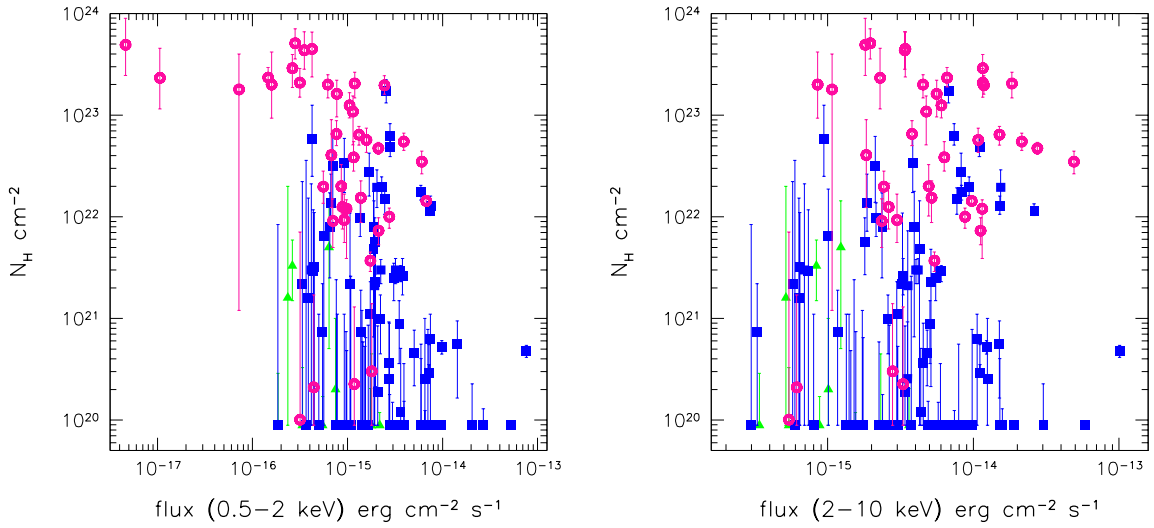

Figure 3.8: Dependence of rest-frame $N_{\rm H}$ values for sources in our sample on the 0.5–2 and 2–10 keV fluxes. Symbols are as in Fig. 3.7. The distribution of absorbing column densities does not seem to vary with hard fluxes, but shows an obvious trend in the soft band (fainter and/or more distant objects appear to be more absorbed).

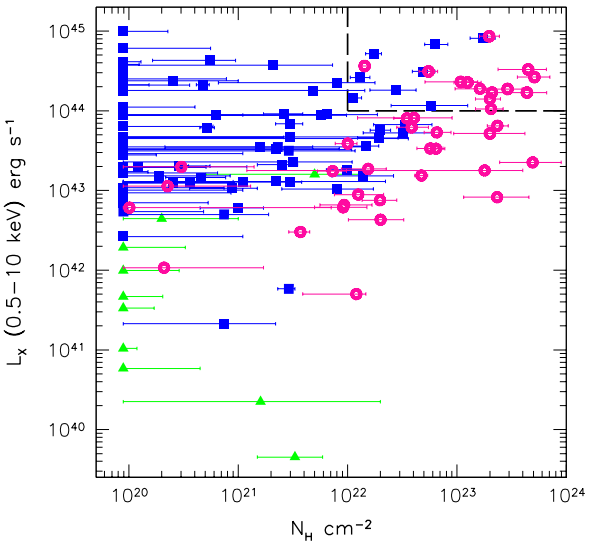

Figure 3.9: Unabsorbed rest-frame luminosity in the 0.5–10 keV bands plotted versus the detected absorption. Symbols are as in Fig. 3.7. Objects in the upper right corners, outlined by the dashed lines, are type-2 QSO (defined as sources with $L_{\rm X} > 10^{44}$ ergs s^{-1} in the 0.5–10 keV band and $N_{\rm H} > 10^{22}$ cm^{-2}).

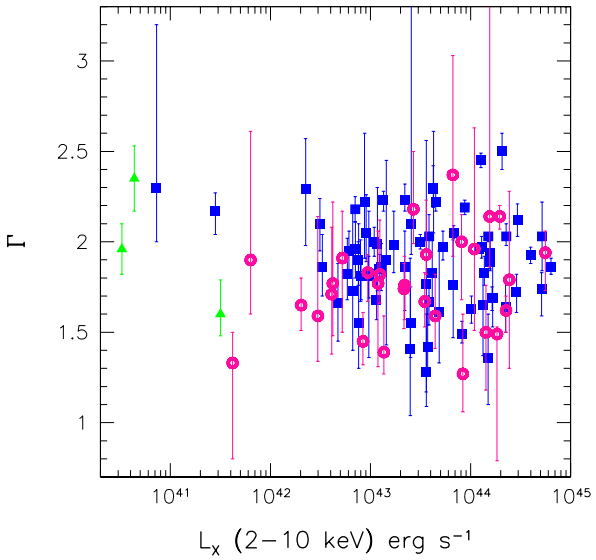

Figure 3.10: The best fit value of power law slopes Γ versus unabsorbed hard rest-frame luminosities L_X. Symbols are as in Fig. 3.7.

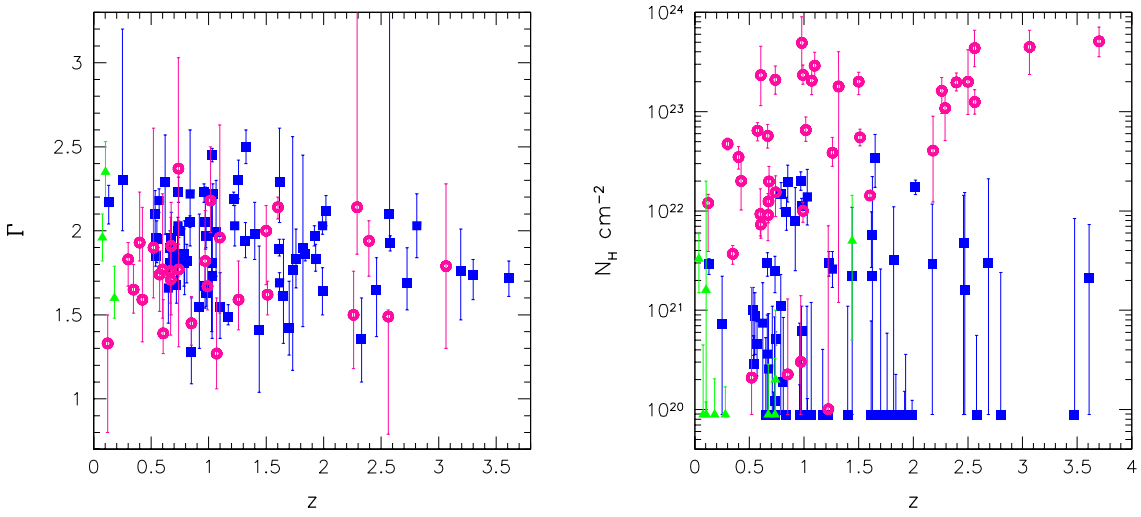

Figure 3.11: Spectral slopes and rest-frame absorption N_H as a function of redshift. Symbols are as in Fig. 3.7.

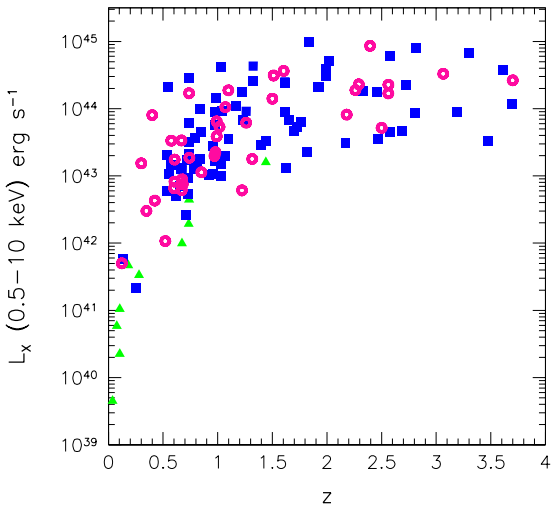

Figure 3.12: The rest-frame luminosity (corrected for absorption) in the 0.5–10 keV band versus redshift. Symbols are as in Fig. 3.6.

the fact that our sample is flux and count-rate limited. There seems also to be an apparent trend of increasing $N_{\rm H}$ with luminosity for type-1 AGN. However, this could be due to the influence of other reasons. At least partly, it could be due to our reduced sensitivity to the absorbing column at higher redshifts, and the fact that the rest-frame soft X-rays, which are the most susceptible to absorption, are redshifted out of the XMM-Newton bandpass. Analysis of the complete sample from the Chandra dataset shows the same trend, but due to the large number of sources it was possible to check the correlation inside several independent subsamples of the sources using Spearman's rank correlation coefficient. As a result, it was found no strong correlation between intrinsic absorption and intrinsic luminosity.

In addition, in Fig. 3.9 we outlined by dashed lines the positions of type-2 QSO, by definition the objects with the highest values of the absorption ($N_{\rm H} > 10^{22}$ cm^{-2}) and luminosity ($L_{\rm X} > 10^{44}$ ergs s^{-1}). For a spectral slope of $\Gamma = 1.8$, a total luminosity of 10^{44} ergs s^{-1} in the 0.5–10 keV band corresponds to 3.9×10^{43} ergs s^{-1} and 6.1×10^{43} ergs s^{-1} in the 0.5–2 and 2–10 keV bands, respectively. Using these criteria, we found 21 type-2 QSO in our sample, while Tozzi et al. (2005) found the number of type-2 QSO in the total CDFS sample is about 54 (including some of the Compton-thick sources). Such selection criteria have been used by Tozzi et al. (2005) for reconsidering the X-ray classification scheme from Szokoly et al. (2004), in order to use the intrinsic luminosities (as opposed to the observed ones) and intrinsic absorption (as opposed to the hardness ratio). However, one of the disadvantages of such an approach is that the selection effect could affect the classification.

In Fig. 3.10 we plotted the spectral slope as a function of the hard X-ray luminosity. The dependence between Γ and the luminosity in the soft band looks quite similar: we

do not see any evident correlation between these two parameters. Also, we do not see evidence for evolution of Γ or $N_{\rm H}$ with redshift (Fig. 3.11). The slight trend that the AGN at high z seem to be more absorbed than the local ones can be partly explained as selection effect due to the incompleteness of our sample at higher redshifts (and the fact that it is easier to detect highly absorbed sources at high z). The similar effect leads to an apparent lack of highly absorbed sources at z$<$ 0.5 as well. The low luminosity absorbed sources at low redshift are difficult to detect due to strongly suppressed flux and, as consequence, low count rate; hence, only the intrinsically more luminous, but rarer, sources can be detected at the particular assumed count rate threshold. This leads to a decrease of detection probability due to the small volume probed at low z.

Fig. 3.12 shows the rest-frame luminosity (corrected for absorption) in the total 0.5–10 keV band as a function of redshift. The luminosities of both types of AGN appear to be evenly distributed between 10^{42} to 10^{45} erg s^{-1} without any obvious trend.

3.4.4 Fe line

The most prominent emission line that we expect to detect in our spectra is the iron line at 6.4 keV (rest frame energy for neutral Fe K$_\alpha$ line) or/and at 6.7 keV (the Fe K$_\alpha$ line from the ionised plasma). To model the Fe line we used a Gaussian line profile with fixed centroid energy at 6.4 keV. With the quality of our spectra we are limited to using a Gaussian instead of more physical models to fit the shape of the line, e.g. in order to search for a relativistic profile.

With the selected significance of 95% for an additional component, we detected the unresolved neutral iron line in 7 sources, which corresponds to 6% of the total number of sources (XID: 39, 41, 42, 49, 56, 206, and 539). One of the sources (XID 41) shows the line with the assigned significance level, but only in the MOS spectrum, while its pn spectrum alone gave 85% significance level for the additional line component. Therefore fitting the two spectra together reduced the significance of the line. However, a clear detection in the MOS spectrum together with an additional evidence from the Chandra spectrum allowed us to conclude that this source required the line in the spectrum.

We show one of these 7 sources in the Fig. 3.13. The average equivalent width of the detected lines was about 300 eV, with a range between 35 eV up to 2 keV.

A similar analysis was done with the Chandra dataset using a larger number of sources, and with 90% significance for the line component. In addition to our 7, Tozzi et al. (2005) detected 18 new sources. Using these 25 objects (8% of the total number of sources), it was shown that there was no obvious correlation between the equivalent width and intrinsic absorption.

Our findings are in a good agreement with the results from other deep surveys. For example, from the 123 bright sources in the Lockman Hole field, 7% show significant Fe K$_\alpha$ emission features with equivalent widths in the range 220–1460 eV (Mateos et al. 2005). A similar value of $\sim$ 7% and the EW range (100–1300 eV) has been

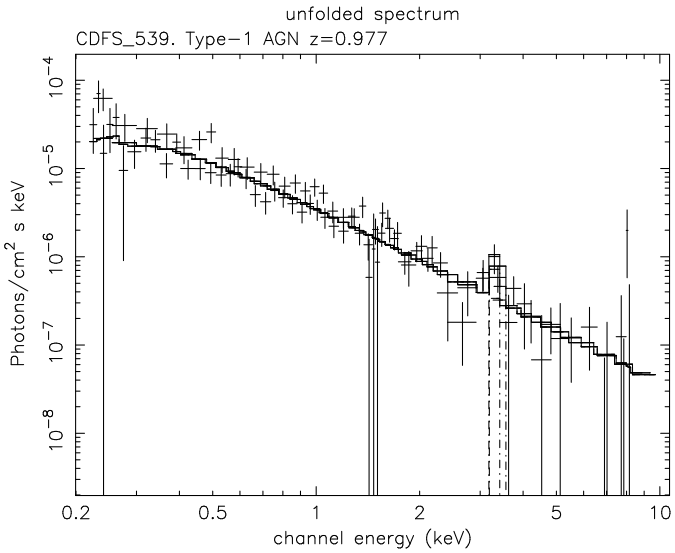

Figure 3.13: An example of unfolded spectra of the type-1 AGN (XID 539) with the detected Fe K_α line (EW $\sim$ 270 eV).

obtained from an analysis of the bright 136 sources in Chandra Deep Field North as well (Bauer et al. 2003).

3.4.5 Soft excess

Analysis of the soft component is very important in terms of properly modeling of the absorption and the power law slope. For some of our type-2 AGN, the detection of $N_{\rm H}$ and spectral shape were only significant after taking into account the soft excess as a spectral component.

We found a clear soft component in 7 type-2 AGN and 4 type-1 AGN (corresponding spectra are presented in Fig. 3.14), although the origin of this component is believed to be different for the two AGN classes (see an extensive discussion in Section 1.4). For the analysis of type-2 AGN (XID: 10, 29, 35, 41, 66, 70, 145) we used a scattering or partial covering model (nuclear radiation scattered by warm medium/leaking through the absorber), implying that only part of the X-ray emission from the inner most region of the AGN is absorbed. The average covering fraction of the absorber is 0.91$\pm$ 0.05 (the maximum and minimum values being 0.96 and 0.85), implying that the scattering fraction in these sources range between 15%–4 %. This result is in agreement with the results from other surveys, which indicate, that the soft excess is very common for type-2 AGN (e.g. Turner at al. 1997).

The soft excess, as a dominant feature in the emission below 1 keV, is seen in typical Seyfert 1s as well (e.g. Turner & Pounds 1989). The best model for this component is a blackbody, with the most obvious conclusion being that it is thermal emission from accretion disk (however, other interpretations are also possible). Except one source (one of the brightest QSO in our field, XID 42), the measured temperature is in good agreement with this interpretation. The obtained rest-frame temperatures

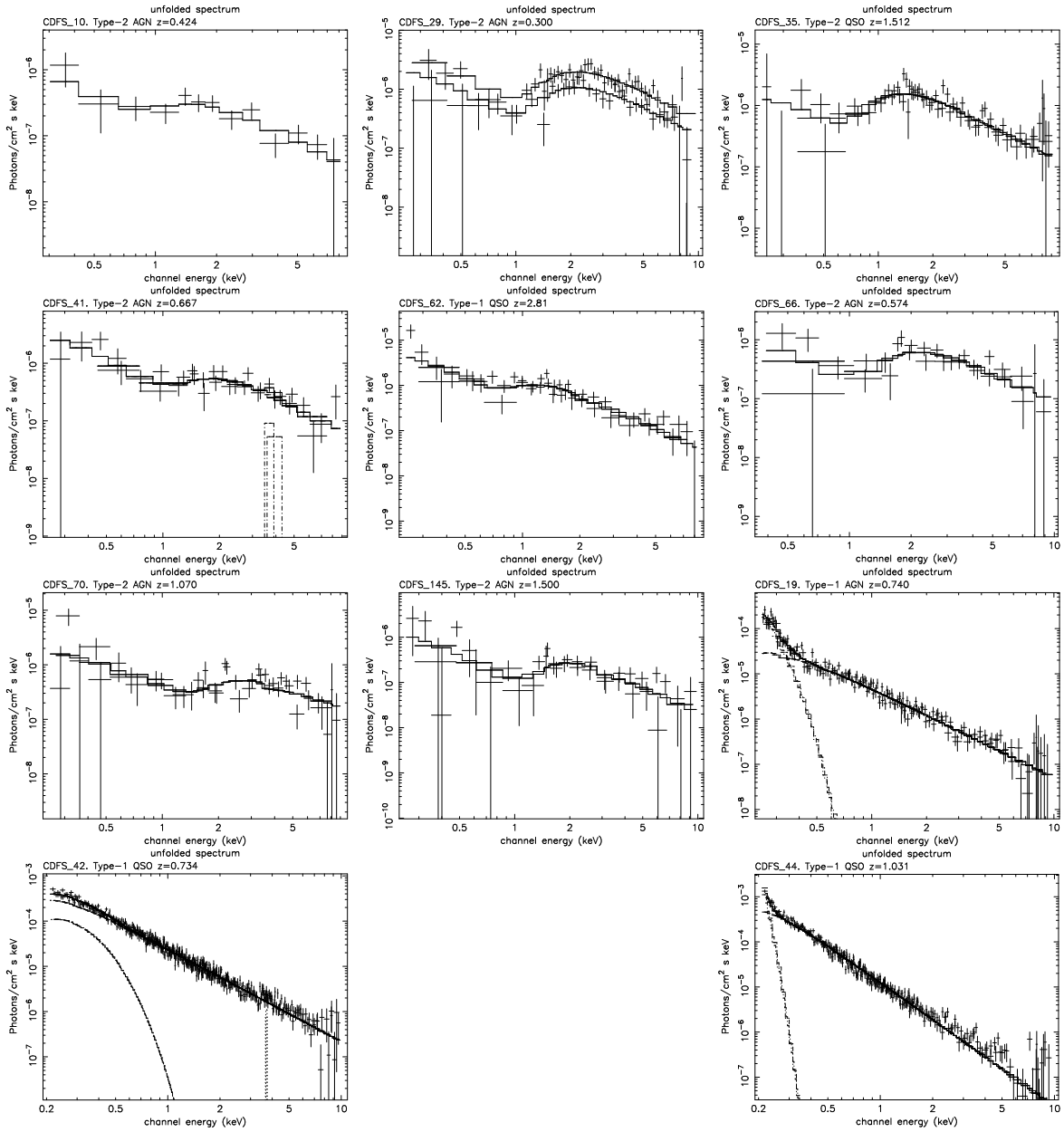

Figure 3.14: The unfolded spectra and best fit model for the sources in our sample where we detected a soft excess. The 7 type-2 AGN and one type-1 QSO have been fitted with a scattering or partial covering model. The last three sources are type-1 AGN with the soft component represented by a black body model. Note that two of these sources (XID: 41 and 42) have an additional feature at high energies corresponding to a neutral iron line (EW $\sim$ 300 eV and 35 eV, respectively).

of the black body emission were kT =$0.051^{+0.001}_{-0.003}$ keV (XID 19), $0.11^{+0.02}_{-0.01}$ keV (XID 42) and $0.021^{+0.001}_{-0.001}$ keV (XID 44).

However, one of the type-1 QSOs (XID 62), optically classified as a BAL QSO at z =2.81, shows not only the absorption in X-rays (see discussion in Section 3.4.2), but also a clear soft component which we modelled with a scattering or partial covering model mainly used for the type-2 AGN. The obtained covering fraction of the absorber is 0.87 $\pm$ 0.05.

3.4.6 Representative X-ray spectra

In the Fig. 3.15 we show 8 spectra/footnotein the form of "unfolded" count spectrum, determined by multiplying the measured count spectrum by the ratio of the best-fit model photon spectrum to the best-fit model count spectrum representative of the different classes of objects in our sample. The two spectra of type-1 AGN and QSO are classical examples of unabsorbed objects in our survey, which are fitted well, generally, with Γ about 1.8–2.2 and $N_{\rm H}$ consistent with the Galactic value (8.9×10^{19} cm^{-2}). Such spectra are also common for galaxies which are mostly unabsorbed or low absorbed objects but with different values of power law slope. As was already discussed, type 2 objects in most of the cases required an absorbed power law, especially type-2 QSO as most heavily absorbed sources known so far. The two spectra of the atypical AGN are represented by absorbed type-1 QSO and unabsorbed type-2 AGN. In these cases the spectroscopic classification turns out opposite to the X-ray classification, when the latter is based on the X-ray obscuration. Finally, for completeness, we presented a typical soft X-ray spectrum of the foreground late-type star detected in the deep surveys. Such sources do not show significant emission above 2 keV and can be fitted with models consistent with the hot thermal emission (e.g. `XSPEC` models `apec, mekal`). The models yield typical temperatures between 0.5 and 0.7 keV and low Fe abundance of 0.04–0.1 solar.

3.5 X-ray stacking analysis

Deep sensitive X-ray observations provide a powerful method to overcome the effect of gas absorption in highly obscured and/or faint AGN. However, some of the distant and highly obscured objects (e.g. type-2 QSOs) appear very faint even in the deepest X-ray observations and, even if they could be detected, they would be too faint for detailed analysis. In such situation, by 'stacking analysis' technique we can obtain the useful information about average properties of such classes of objects. This method turned out to be particularly efficient even beyond the effective limiting flux of the X-ray observations, reaching equivalent total exposures from 10 to 100 times the nominal ones and pushing the X-ray detection more than two orders of magnitude deeper (e.g. Chandra analysis of the Chandra Deep Field South and North; Brandt et al. 2001, Hornschemeier et al. 2002, Nandra et al. 2002). Nowadays, the stacking analysis is widely applied in X-ray astronomy for determining mean properties of the objects regardless of detection status (e.g. Green et al. 1995, Della Ceca et al. 1999). By

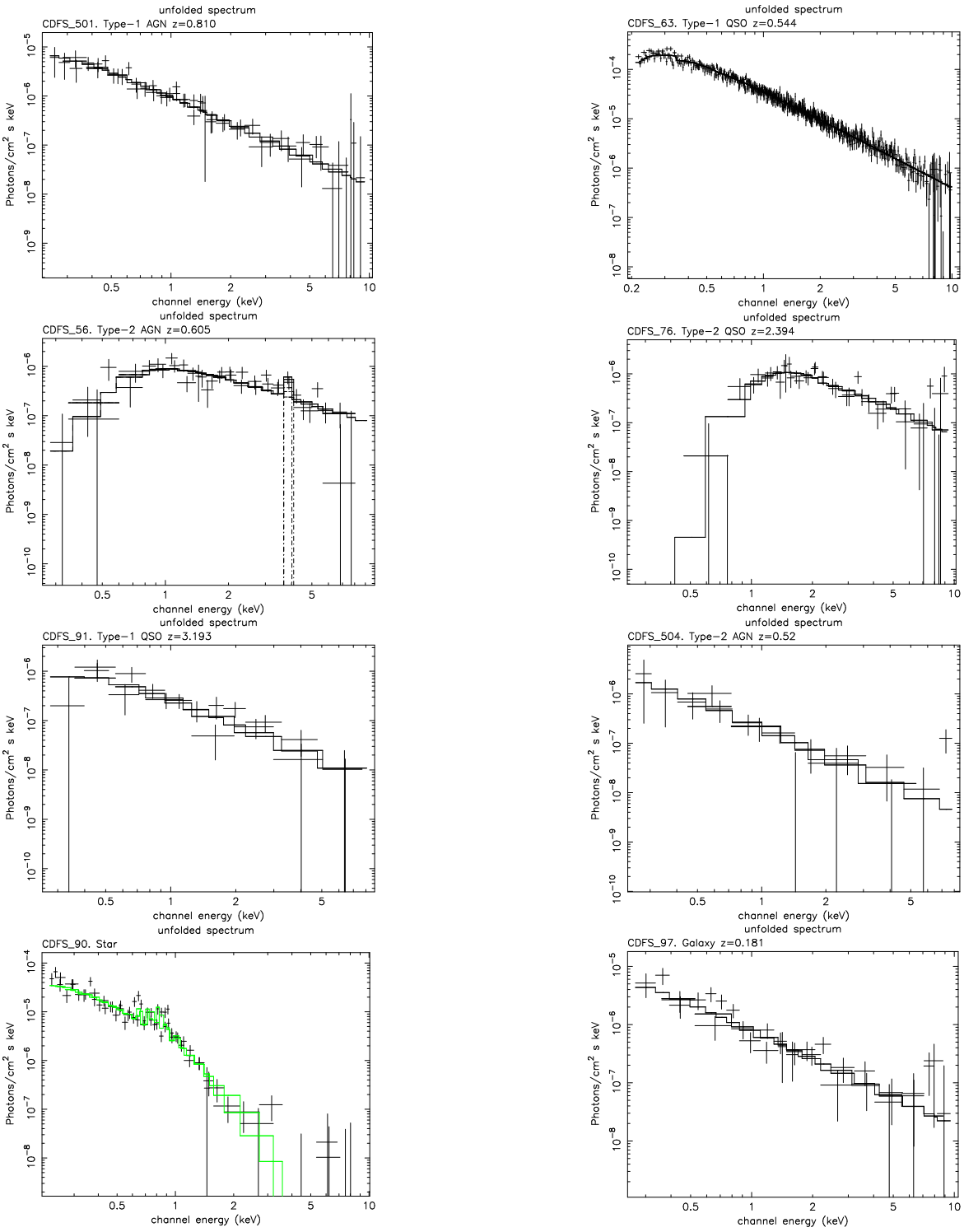

Figure 3.15: The unfolded model X-ray spectra representative of the different classes of objects in the CDFS. Again, the source numbers refer to the Chandra catalogue (Giacconi et al. 2002). From top to the bottom: unabsorbed type-1 objects (type-1 AGN and the brightest type-1 QSO); absorbed type-2 objects (type-2 AGN with clear Fe line (EW $\sim$ 567 eV, see for details Sect. 3.4.4) and type-2 QSO); atypical objects in the sample (type-1 QSO with the signature of absorption of the order of 10^{22} cm^{-2}, and unabsorbed type-2 AGN); M-type star (with `apec` *best fit model with temperature $kT = 0.50^{+0.04}_{-0.02}$ keV) and a galaxy.*

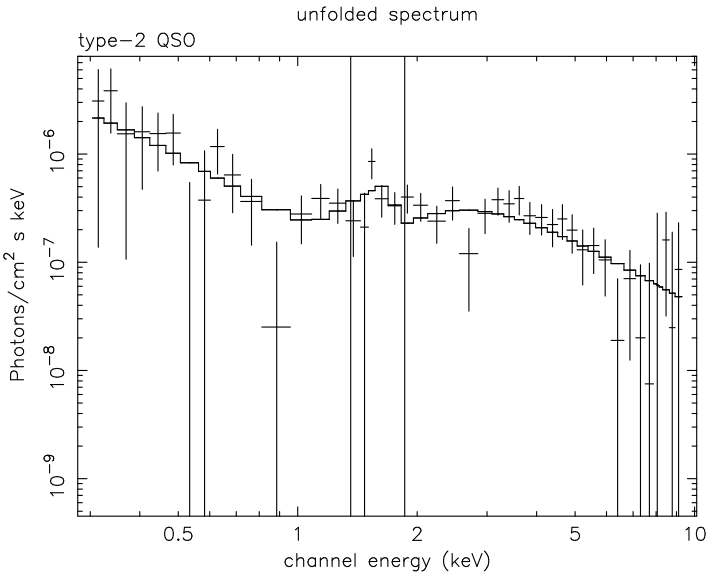

Figure 3.16: Integrated X-ray spectrum for the most distant type-2 QSOs (z_{int} = 3.081); unfolded scattering model. Two vertical lines show a position of a possible bump due to the shifted Fe line. The iron line is smeared between 1.35–1.86 keV (observed frame) due to the spread in source redshifts (z range from 2.56 to 3.77).

adding together X-ray photons from well-defined classes of objects, it is possible to determine their mean X-ray properties; by removing known, bright X-ray sources from the sample it is also possible to investigate the mean properties of sources too weak to be individually detected (e.g. Brandt et al. 2001, Nandra et al. 2002).

In order to study the average X-ray properties of the objects in the CDFS, we grouped sources according to their class (e.g. type-2 QSO), or by particular flux range, and produced the integrated spectra.

3.5.1 Type-2 QSOs

A class of highly luminous and obscured type-2 AGN, so called type-2 QSOs, has been firstly detected in deepest radio surveys (the so called radio galaxies). The first examples of the long-sought radio quiet part of these objects have been detected in two deep Chandra fields (Norman et al. 2002, Stern et al. 2002) and in the XMM-Newton deep survey in the Lockman Hole field (Lehmann et al. 2002). Studies of type-2 QSOs are very important not only for better understanding of the AGN evolution at high z, but also for the X-ray background population-synthesis models. However, a detection of such objects requires deep X-ray observations, but in most cases they are still too faint for individual analysis.

In our field, at z >2.5, there are six type-2 QSOs (XID 27, 54, 57, 112, 202, 263), the most famous of which is XID 202, described in detail by Norman et al. (2002). All these objects have narrow Ly$_\alpha$ and CIV emission, $HR > -0.2$, and faint optical magnitudes $R \geq 24.0$ (Szokoly et al. 2004).

We extracted a combined spectrum for the type-2 QSOs described above using the

SAS task `evselect`. We choose several source free areas around our objects to get the background spectrum. As in the case of the individual spectra, we used the `rmf` (latest pn canned response matrix) and `arf` (created with the SAS task `arfgen`) response files to account for the filter, mode and telescope vignetting. The stacked spectrum was grouped to have at least 40 total counts per bin.

For the first time this high quality integrated spectrum of the most distant type-2 QSOs shows an absorption with a clear soft component, which we fit by a scattering/partial covering model, assuming an average redshift for these objects of $z_{int} = 3.081$. The result is shown in Fig. 3.16. An additional feature, a clear hump at energy 1.35–1.86 kev in the observed frame, is clearly seen in our spectrum as well. The most plausible explanation of this feature is a smeared iron line, because the redshifts of the individual sources are in a broad range of 2.56 to 3.77.

Our spectrum is well fitted ($\chi^2_\nu = 0.88$) by a scattering or partial covering model with $N_{\rm H} = 9^{+2}_{-1} \times 10^{23}$ cm^{-2}, $\Gamma = 2.14^{+0.15}_{-0.12}$ and a covering fraction of the absorber of $0.96^{+0.02}_{-0.04}$. It has unabsorbed luminosities of $L_X = 6.5 \times 10^{44}$ erg s^{-1} and $L_X = 1.2 \times 10^{45}$ erg s^{-1} in the 0.5–2 and 2–10 keV bands, respectively.

The clear detection of the soft component in the stacked spectrum of the most distant type-2 QSO could have profound consequences for the unified model of AGN, because a similar soft component has already been observed in type-2 AGN at different redshifts. This result also implies that for the distant (z > 2.5) type-2 QSO the soft component might be required.

This result is very important considering an intrinsic difference in the internal properties (such as variability) of in unabsorbed and absorbed sources in the CDFS. As it is shown by Paolillo et al. (2004), the variable and nonvariable sources represent two distinct populations in terms of their absorption, and in general unabsorbed sources are more variable than absorbed ones. The detection of a soft component in the spectra of the most distant type-2 QSO has been used by Paolillo et al. (2004) as supporting evidence of a new model which explains this observed correlation between variability and absorption in the CDFS sources. Briefly, the X-ray observed emission is due to two main components: a highly variable one that originates near the central engine, and a reflected one produced by material distributed over a large region, which dilutes the intrinsic variability of the primary component. When the central engine is observed directly, i.e., through low column densities, the first component dominates the total flux and thus the variability. In high-$N_{\rm H}$ sources, instead, the primary component is highly absorbed. Then, if the reflecting material is distributed at large distances from the central BH or in a geometrical configuration such that it is relatively unaffected by the obscuring material (e.g., the molecular torus in the classic unification scheme), the scattered component will represent an increasingly large fraction of the observed emission, thus accounting for the lower variability. In conclusion, the lack of variability in hard, absorbed sources is due to an increased contribution of reflected X-ray to the total flux.

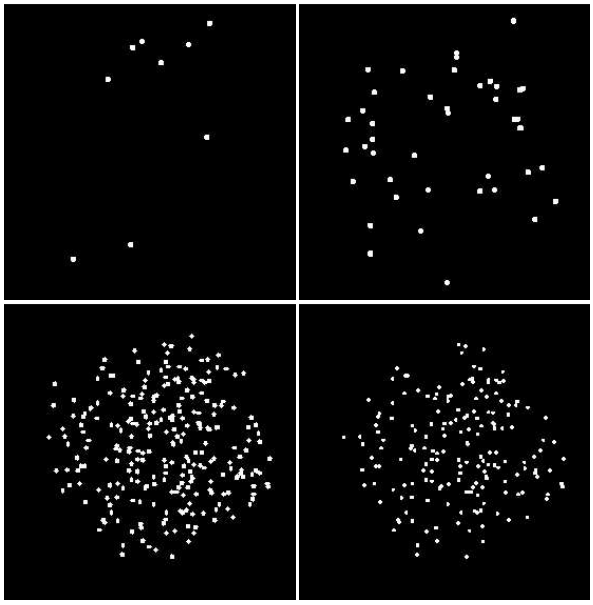

Figure 3.17: The mask region files for the stacked spectra. Four panels represent the masks for bright, medium, faint and very faint source subsamples (see Section 3.5.2 for details). The white circles denote the extraction zones.

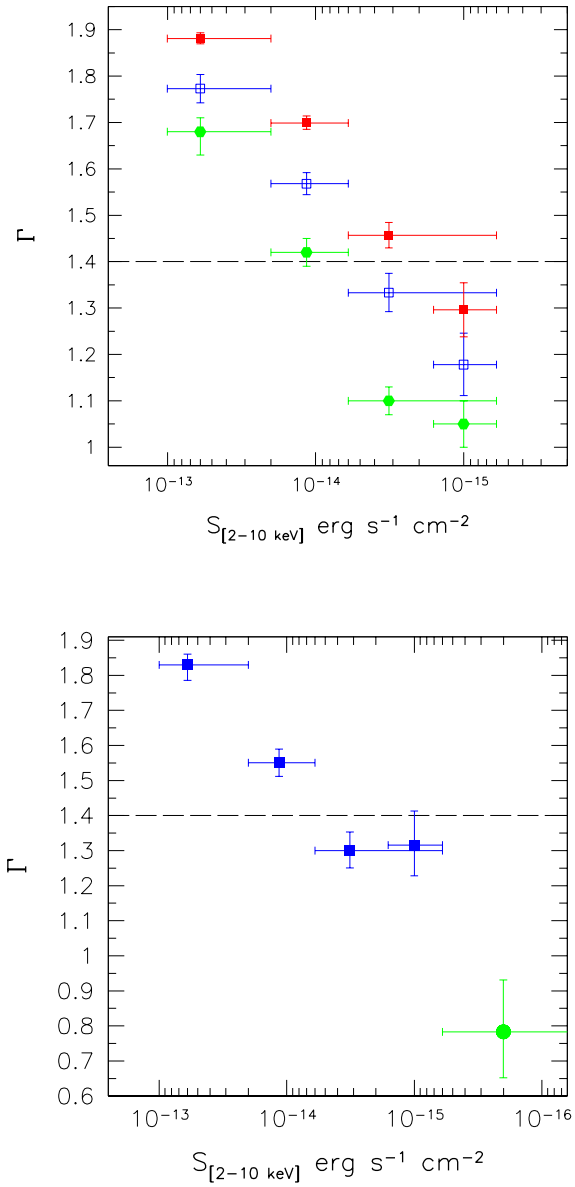

Figure 3.18: The average power law indices of the stacked spectra of the bright, medium, faint and very faint subsamples of the sources detected in the 2–10 keV band. The upper and lower plots show the values obtained using different methods for modeling of sky and instrumental backgrounds (see text for details). Top: estimating the background using the source-free area in both XMM-Newton and Chandra data. Filled hexagons refer to the 1 Ms Chandra exposure of the CDFS (Rosati et al. 2002). XMM-Newton data were fitted in the two energy bands: 1–8 keV (open squares) for comparison with results from the Chandra data set and 0.4–8 keV to include soft band (filled square). Errors on Γ refer to the 90% confidence level. The local absorption has been fixed to the Galactic value of 8.9 $\times 10^{19}$ cm^{-2}. The line corresponds to the average Γ for the background. Bottom: The average Γ, obtained by fitting the XMM spectra in the 1–8 keV for the same subsamples (blue points) using a modelling of the sky and intrumental backgrounds with spectral components, as described in the text. The green point shows the spectrum of the unresolved XRB, obtained with the same method.

3.5.2 Spectral index as a function of flux

It was previously shown from ROSAT data of the Lockman Hole (Hasinger et al. 1993) and later confirmed using the Chandra megasecond observation of the CDFS (Tozzi et al. 2001 and Rosati et al. 2002), that in both the hard (2–10 keV) and the soft (0.5–2 keV) bands the fraction of hard sources increases towards lower fluxes. To understand how the spectrum of the XRB is built up at different flux levels, Rosati et al. (2002) defined four subsamples according to the source flux in the 2–10 keV band: bright (S$>$ 2 $\times 10^{-14}$ erg cm^{-2} s^{-1}), medium (2 $\times 10^{-14}$ $>$ S $>$ 6 $\times 10^{-15}$ erg cm^{-2} s^{-1}), faint (S $<$ 6 $\times 10^{-15}$ erg cm^{-2} s^{-1}), and very faint (S $<$ 2 $\times 10^{-15}$ erg cm^{-2} s^{-1}). Each of these subsamples was modeled with an absorbed power law in the 1 to 10 keV energy range with the local absorption fixed to the Galactic value. They found a trend of hardening in the stacked spectra (decrease in $\langle\Gamma\rangle$) with decreasing X-ray flux in the hard (2–10 keV) band. In order to investigate the behaviour of the spectral shape as a function of the hard flux in the XMM-Newton data, we repeated the spectral extraction for the same source subsamples as in Rosati et al. (2002), using the masks shown in Fig. 3.17. We assumed that the fluxes from the XMM-Newton and Chandra data sets are equal, as was discussed and shown previously in Sec. 2.2.1. Two methods for subtracting the background were applied, either the using of the source-free area, or a spectral modelling of the background components. The first approach allowed us to be closer to the Chandra fitting strategy and to make a comparison with values in the soft and hard bands, while the second approach could be used also to investigate properties of the unresolved faint source population, in addition.

The source-free area for the background accumulation has been defined as a left-over area after excising 25″ circles around the position of each Chandra source. In the background subtraction we have renormalized the source-free spectrum to the detector area. In the second approach we used filter wheel closed observation to measure the internal/particle background. This background is accumulated at the same position as the source and normalized according to the observation time. Following Finoguenov et al. (2003), Zhang et al. (2004) and Snowden et al. (2004), two spectral components accounting for the Galactic foreground and soft proton component are added. Both of them are absent in the filter wheel closed data. The galactic component could be efficiently modelled by a thermal plasma emission of $\sim$ 0.2 keV temperature and is dominated by the Milky Way Halo. The soft proton component is modelled by a power law, which is not folded through the telescope effective area, which leads to appreciable differences in the power law model of the source. Technically, to apply such a modelling within XSPEC v.11.3, the telescope characteristics are all be stored in the auxilary response file (`arf`).

After subtracting the background and applying the response files (`rmf` and `arf`), we fit the spectra in `XSPEC` using the two step correction model (`wabs(apec+powerlaw)+powerlaw/b`). We know, that both the soft proton and the galactic components disscused above dominate at energies below 1 keV and to reduce the systematics associated with modeling of these components, we perform a two step approach to the spectral fitting. As a first step in the spectral analysis, we use

the 0.3–7.5 keV range for determination of the soft galactic emission parameters (i.e. temperature and normalisation). Allowing the temperature to change and using a fixed solar abundance, we obtained a temperature of 0.2 keV for the Milky Way Halo component. Secondly, we fix the background components and use a 1–7.5 keV energy band. Throughout the analysis we always exclude the energies contaminated by the Al K_α line (1.4–1.6 keV).

Using the first method of the background subtraction, we fitted our data in the two energy bands: 1–8 keV (for comparison with results from the Chandra dataset) and 0.4–8 keV (extending the spectral analysis towards the softer energies). The Chandra energy range nominally extends until 10 keV, but in reality it loses sensitivity above 7 keV, therefore for correct comparison we exclude energy bins above 8 keV. The result is shown in Fig. 3.18 (upper plot).

The best-fit slopes for bright, medium, faint and very faint subsamples obtained using the 1–8 keV band are 1.77 ± 0.03, 1.57 ± 0.02, 1.33 ± 0.04, and 1.18 ± 0.03, respectively. A similar analysis, but using the 0.4–8 keV band yields the slope values of 1.82 ± 0.01, 1.70 ± 0.01, 1.46 ± 0.03, and 1.30 ± 0.06, respectively.

The second method using the 1.0–8.0 keV band results in the slope values of $1.83^{+0.03}_{-0.04}$, $1.55^{+0.04}_{-0.04}$, $1.30^{+0.05}_{-0.05}$, and $1.32^{+0.10}_{-0.09}$, respectively. The source-free spectrum can also be modelled and yields $\Gamma = 0.78^{+0.15}_{-0.13}$ (see the lower panel in Fig. 3.18). Further details are given in the next subsection.

Both methods gave comparable values of the average spectral slope in the 1–8 keV range and unambiguously indicate a hardening of Γ towards lower fluxes. The trends are apparent in Fig. 3.18 where our results are compared to the corresponding results from the Chandra data set.

The average value of Γ obtained from the stacked technique is lower than the average value derived from individual sources. This result, most probably, connects not with an intrinsically harder power law but is caused by washing out of the signature of absorption column density. This effect has also been noticed by Mainieri et al. (2002) and is shown to be driven by averaging the spectra, which are intrincically absorbed at different redshifts.

We detect a significant hardening of the average spectral slope going to lower fluxes. However, we also notice, by using the first method, a regular increase in $\langle\Gamma\rangle$ with decreasing flux for different subsamples of fluxes in comparison with Chandra results. This is especially clear for low flux subsamples. Moreover we can see a discrepancy of the values within our own data set, if we fit the spectra in the different energy bands (including and excluding the soft band). However, both treatments indicate a clear evolution with decreasing flux for the combined integral spectra of faint objects.

One of the main conclusions, (i.e. that we detect a change in the value of the power law slope when soft band photons are included), is important, considering the comparison between Chandra and XMM-Newton datasets (next section). The main difference between the two fitting strategies is that in XMM-Newton we include the softest energy band, while in Chandra this component is not included. This can explain the observed difference between our results for the same source.

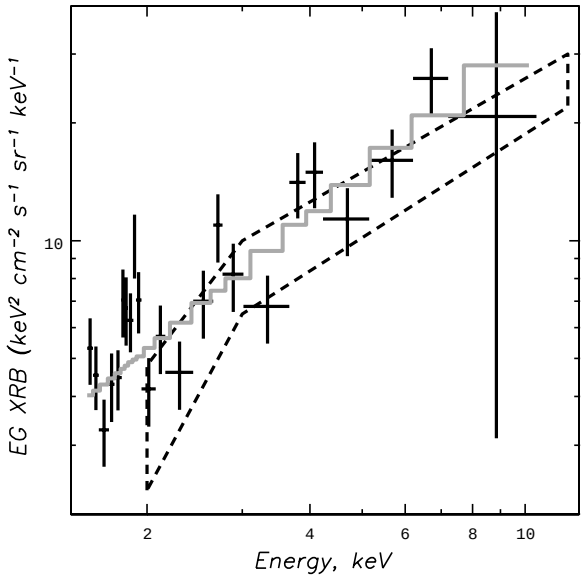

Figure 3.19: The spectrum of the unresolved X-ray background in the CDFS. The points represent EPIC pn data extracted in the area devoid of sources detected by either Chandra or XMM. Gray line represents the power law approximation of the points, of index 0.8±0.15. Dashed area represents a similar result obtained by Worsley et al. (2004).

3.5.3 Spectral properties of the unresolved Cosmic X-ray background

The stability of the quiescent level of the EPIC pn background (Freyberg et al. 2003)[3] allows to carry out a study of the unresolved X-ray background spectrum. We remove all the sources, detected by Chandra and XMM-Newton down to an unprecendented flux limits of 5.5×10^{-17} and 4.5×10^{-16} ergs s^{-1} cm^2 in the soft and hard, respectively, using 25″ circles, which results in $< 20\%$ residual flux contamination due to XMM XRT PSF.

We select two annuli for the residual spectrum estimation. The first is within 6.7′ radius from the CDFS center, the second extends to 13′. The instrumental background is subtracted using the accumulation obtained with the filter wheel in the closed position after applying similar light curve cleaning criteria. One can double-check the background subtraction by looking into the performance for the outermost radial bin, where background dominates due to the vignetting and also use the energies above 12 keV. Both those tests showed a satisfactory level of the background subtraction.

Fig. 3.19 shows the resulting spectrum for the central region, where the source removal is possible to fainter fluxes. An approximation of the residual spectrum with a power law yields the following parameters:
the power law photon index of $0.8^{+0.1}_{-0.2}$ with 2.5±0.5 keV^2 cm^{-2} s^{-1} sr^{-1} keV^{-1}. As is

[3]Additional information about spectral and temporal properties of the internal background of the XMM-Newton EPIC pn Camera and spatial distribution of the internal background fluorescence lines see at: `ftp://ftp.xray.mpe.mpg.de/people/mjf/public/mfreyberg-WA2-16.ps.gz`
`ftp://ftp.xray.mpe.mpg.de/people/mjf/public/mfreyberg-WA2-7.ps.gz`

shown in Fig. 3.19, this is in a very good agreement with the results of Worsley et al. (2004), where construction of the residual CXB spectrum used the total CXB spectrum, as obtained by EPIC MOS (De Luca & Molendi 2004) removing the contribution from the sources resolved in the deep XMM pointing in the Lockman Hole.

Our characteristics for the residual flux in the outer ring are 1.1 ± 0.1 for the photon index and normalisation at 1 keV of 4.8 ± 1.2 keV^2 cm^{-2} s^{-1} sr^{-1} keV^{-1}. Compared to the inner radius, the residual XRB flux in the outer radius is larger, while in the same time the power law slope is softer. This is due to lower limit on source detection and subsequent removal on one hand and a softening of the source spectra with increasing flux on the other, as is studied elsewhere in this chapter.

3.6 Comparison between XMM and Chandra

In Sec. 2.2.1 we show the simplest test for the differences between Chandra and XMM-Newton datasets. The results from the direct comparison between the two source catalogs show that, basically, source fluxes are the same except for extended and some fainter objects. Therefore all possible discrepancy in the results from the model fits concerns mostly the differences in strategy of spectral analysis (proper calibration, using models and energy range etc). Among the relevant differences between our analyses, is that for the Chandra datasets fits were performed in the 0.6–7 keV energy range using Cash statistics, while we used the 0.2–10 keV range and χ^2 minimisation. In order to study in more detail how these differences affect the correlation between spectral parameters detected by Chandra and XMM-Newton, we selected the same 127 sources from Tozzi et al. (2005) that we used in our XMM-Newton analysis. The main parameters which we correlated were fluxes, luminosities, power law slopes and absorption columns. The results are presented in Fig. 3.20 – Fig. 3.24.

As was already shown in Fig. 2.4, we have a quite good agreement in fluxes derived from our source detection procedure assuming a constant Γ=1.4 for all sources independent of the real nature of the object. Now we plotted the fluxes obtained from the best fit models (sometimes different in the Chandra and XMM analysis). Our agreement is still very good, except for several sources. The next important parameter is spectral index Γ (Fig. 3.21). We can see systematic differences between values, even taking into account larger values of the error bars. The detailed study of the power law distribution for the analysed sources (Fig. 3.22) shows that the difference between the XMM-Newton and Chandra values is significant. XMM-Newton has not only a larger value for the mean Γ (1.86 in contrast to 1.75 for Chandra), but also higher values for the power law slopes in general, and somewhat larger dispersion than Chandra. The correlation between values for the absorption is in agreement only for the absorbed sources (above 10^{22} cm^{-2}), except for the three type-2 sources fitted in Chandra analysis with `pexrav` model. We achieved a good agreement for the unabsorbed luminosity in the hard band down to the fainter luminosities and only three Compton-thick sources appear as outliers. In the soft band the correlation is worse because the absorption in this band plays an important role, and this has caused this disagreement in the absorbed values and, as a result, the discrepancy in the soft

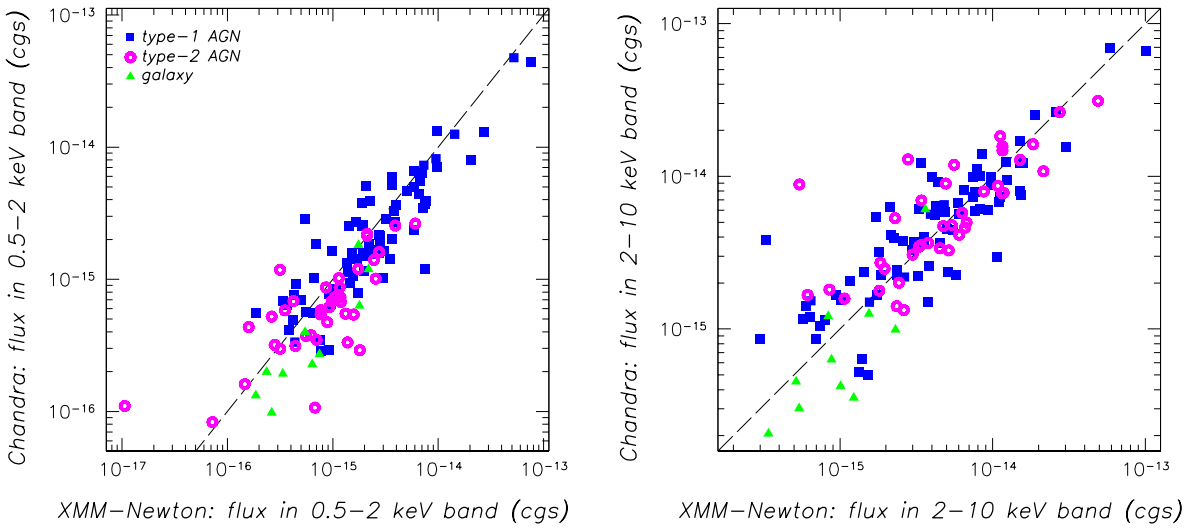

Figure 3.20: Direct comparison between XMM-Newton and Chandra fluxes in the soft and hard bands derived from the best fit model for the sample of 127 sources. Solid blue squares and open magenta circles refer to type-1 and type-2 AGN, respectively. Triangles show the galaxies.

band luminosity.

The most obvious explanation for the observed trends is that, due to the slightly smaller energy range in general, and in particular, due to the missing softer energies (<0.6 keV), Chandra's energy range appears not to be idealy suited to look for absorption. As a result, the absorption column values determined from Chandra data tend to be higher and subsecquently the power law slopes lower. However, for highly absorbed sources this difference must be negligible, because the soft band flux of these objects is highly absorbed and not present in the XMM-Newton data.

To study the relationship between $N_{\rm H}$ and Γ we divided our sources into four subsamples, using the detected intrinsic absorption value as a criterion: the unabsorbed sources (less than 10^{21} cm^{-2}), moderately absorbed (10^{21}–10^{22} cm^{-2}), absorbed (10^{22}–10^{23} cm^{-2}), and highly absorbed sources (more than 10^{23} cm^{-2}). We created the power low slope histograms for each of these subsamples and show it in Fig. 3.23.

The figure clearly shows that we still have different mean values for spectral slopes for Chandra and XMM-Newton data in all four subsamples. However, this difference is less apparent for the samples of the absorbed and highly absorbed sources (lower panels of Fig. 3.23). In addition, the dispersion of the detected Γ values is much higher for the sample of highly absorbed sources and no evident peak is found, indicating that this sample is less homogeneous and may include different types of sources.

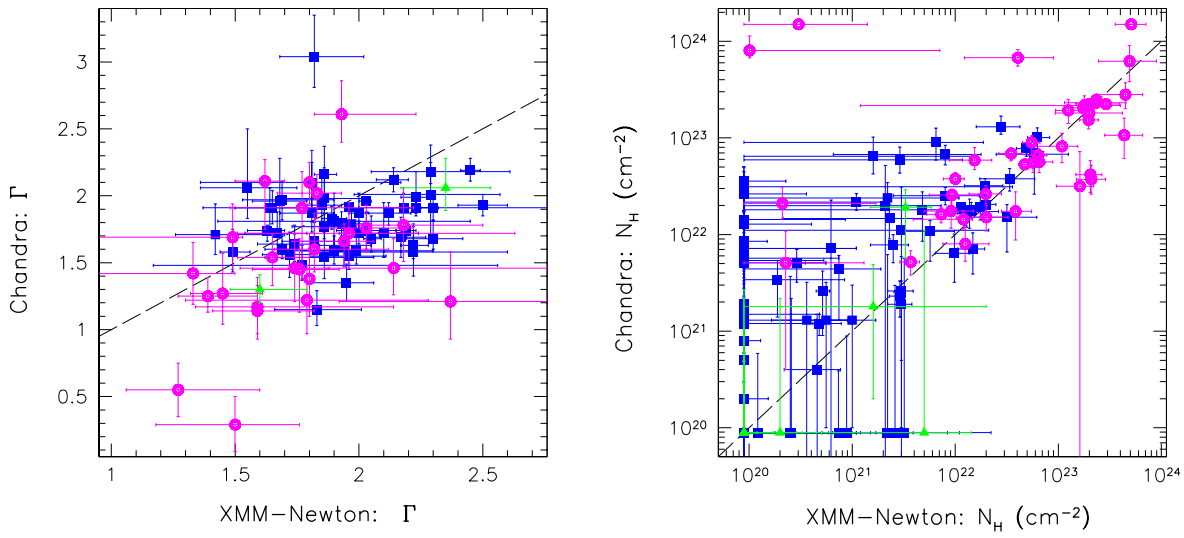

Figure 3.21: Comparisons between XMM-Newton and Chandra values for Γ *and* $N_{\rm H}$*. Symbol are as in Fig. 3.20*

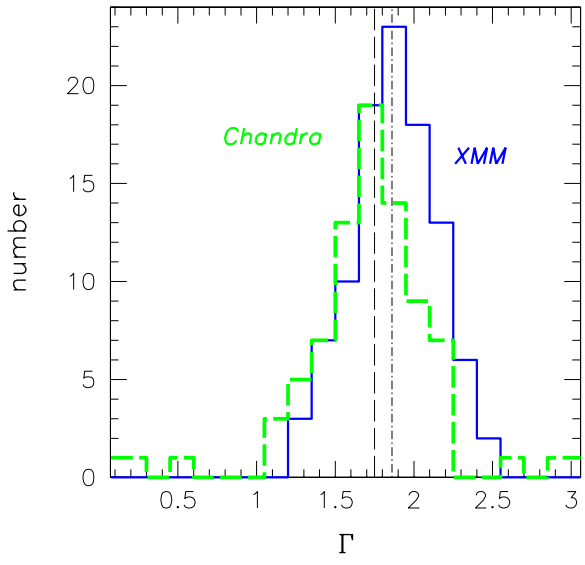

Figure 3.22: The power law slope distributions for the same sample of sources using Chandra and XMM-Newton data. The two vertical lines refer to the weighted mean value $\langle\Gamma\rangle$ *for Chandra and XMM data sets (1.75±0.02 and 1.86±0.03, respectively).*

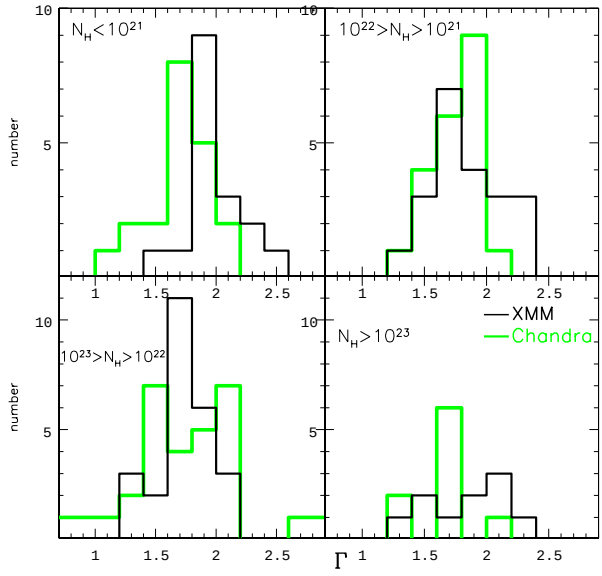

Figure 3.23: The dependence between the power law slope values and the observed column densities. See text for details.

3.6.1 Type-1 AGN

The comparison between the absorption values in the two datasets clearly shows that a systematic trend exists i.e. type-1 AGN in Chandra have larger $N_{\rm H}$ values than in XMM-Newton data. Moreover, we have several BLAGNs which seem to show some non-negligible absorption (of the order of 10^{22} cm^{-2}) in the Chandra analysis, and systematically lower values in XMM.

We decided to study one of these sources in detail. We selected the best quality high-z BLAGN XID 24 (z=3.61). In order to make a direct comparison, we decided to use the same fitting strategy (χ^2 minimization technique) and the same energy range (0.2–10 keV and 0.5–6 keV) for both Chandra and XMM-Newton spectra. We rebinned all spectra in order to have a minimum of 20 counts per bin. We found that, depending on the energy range used, even XMM-Newton values change from $\Gamma = 1.72^{+0.10}_{-0.11}$ and $N_{\rm H} = 0.21^{+0.52}_{-0.20} \times 10^{22}$ cm^{-2} (0.2–10 keV) to $1.77^{+0.16}_{-0.17}$ $N_{\rm H} = 0.91^{+1.47}_{-0.90} \times 10^{22}$ cm^{-2} (0.5–6 keV). Using our method of fitting, we found that Chandra spectrum has $\Gamma = 1.42^{+0.15}_{-0.15}$ and $N_{\rm H} = 0.88^{+1.90}_{-0.87} \times 10^{22}$ cm^{-2} in the 0.5–6 keV energy range (Tozzi et al. (2005) found using Cash statistics $\Gamma = 1.56^{+0.17}_{-0.17}$ and $N_{\rm H} = 1.99^{+3.20}_{-2.02} \times 10^{22}$ cm^{-2}). Interestingly, the simultaneous fitting of the Chandra and XMM-Newton spectra in the 0.5–6 keV range shows the lower values of absorption ($N_{\rm H} = 0.3^{+1.36}_{-0.29} \times 10^{22}$ cm^{-2}, $\Gamma = 1.56^{+0.12}_{-0.09}$).

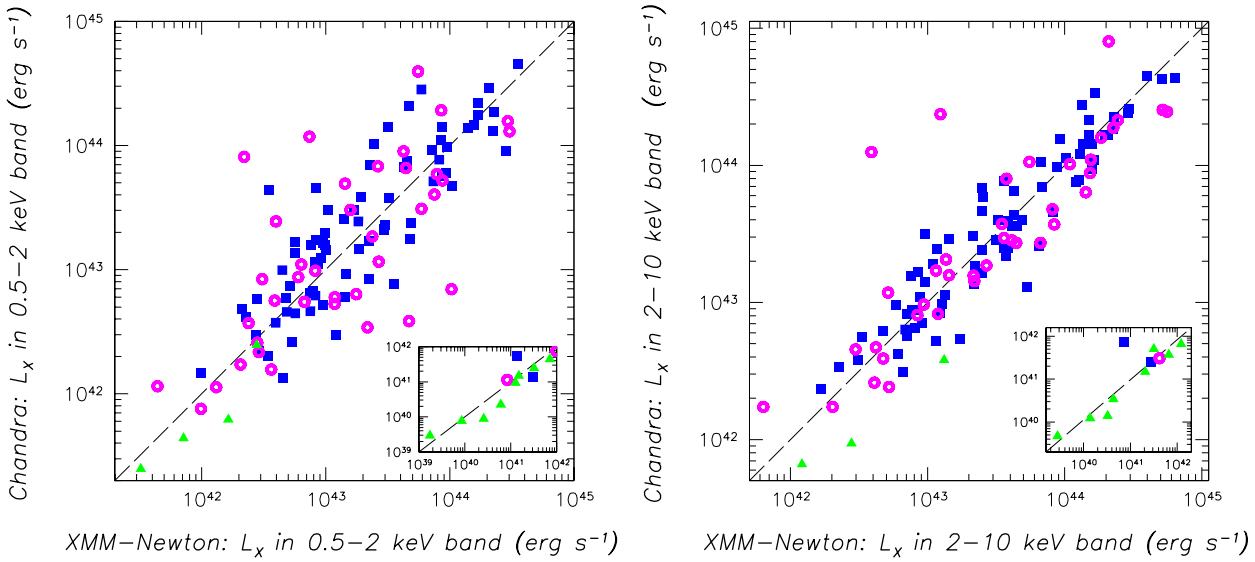

Figure 3.24: Comparison between XMM-Newton and Chandra values for unabsorbed luminosities in the soft and hard bands. The inserts show the L_X in the range below 10^{42} erg s^{-1}.

3.6.2 Type-2 AGN

For highly absorbed sources (typically the type-2 AGN) we have, in general, a good agreement between XMM and Chandra values for different parameters. As already discussed, this is probably due to the fact that the absorption can be detected in the same energy range for both satellites, as the flux detected in the softest band covered only by XMM is not detected for this type of objects.

As in the case of our XMM-Newton analysis of the type-2 AGN, some sources from the Chandra datasets require an additional component for fitting the soft excess. Such sources were fitted with a scattering model constructed as the sum of two power laws (`pow + zwabs pow`), where the slopes of the two power laws were linked together. Such a combination is equivalent to the `XSPEC` model `pcfabs` which we used in our analysis, except for the restriction that the intrinsic normalization of the soft component must be less than 10% of the intrinsic normalization of the main power law. This high upper limit excludes some Chandra sources with lower covering fraction (e.g. as a source XID 70, with the soft component in XMM spectrum, and in Chandra as well, however with normalization larger than 10%), but at the same time helps to avoid a false detection.

From 8 objects (XID: 29, 51, 145, 147, 151, 259, 260, 268), which show the soft component in the Chandra analysis, two were not included in our analysis due to their weakness, and three have poor statistics in XMM-Newton data for fitting using such a complicated model. Therefore we can confirm the detection of the soft component in two objects (XID 29 and 145) only. In our analysis of the source XID 51 the scattering or partial covering model shows the same reduced chi-squared as the simple absorbed

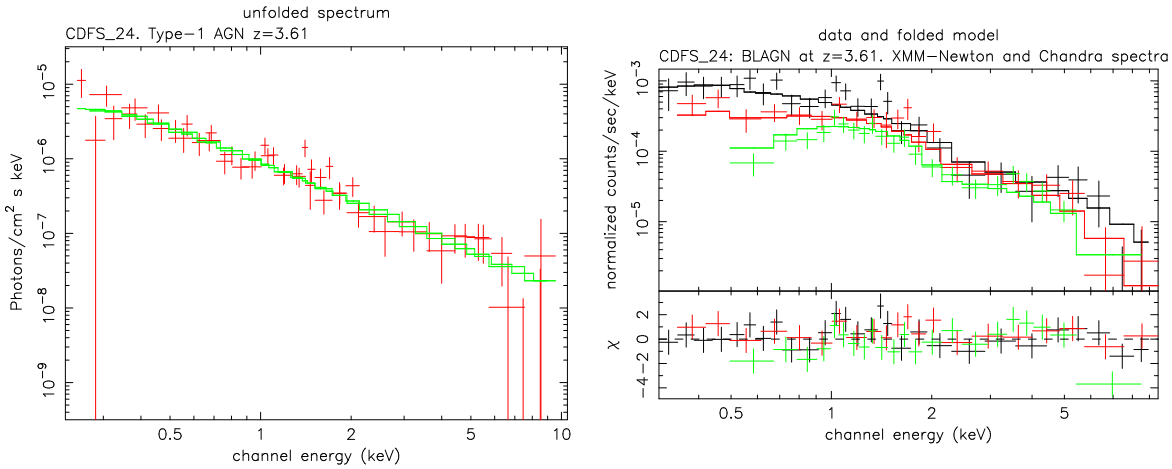

Figure 3.25: Source XID 24 classified as Type-1 QSO (BLAGN) at z=3.61. Left: The unfolded X-ray spectra (pn and merged MOS) and the best fit model – unabsorbed power law. Right: XMM-Newton (shown in black and red, for pn and MOS respectively) and Chandra (green) spectra of the source. Due to the smaller energy range, the Chandra spectrum appears to be more absorbed than that of XMM-Newton. Chandra spectrum courtesy of P. Tozzi.

power law.

3.6.3 Galaxies and low-luminosity AGN

The analysis of most faint objects in both surveys identified as galaxies, is particularly suitable for testing how good is the agreement beteween the two satellites. As was defined above, galaxies are objects with typical luminosities in the range between 10^{41}–10^{42} erg s^{-1}, implying that these objects are either low-luminosity AGN or star forming galaxies.

With XMM it was possible to extract and analyze 10 sources in the redshift range between 0.038 (bright ULX galaxy 247) and 1.44.

Due to the lack of statistics for these faint objects we need to fix the spectral slope in order to get information for the rest of spectral parameters. In three cases (out of 10) we were able to fit the slope of the power law too and the XMM value were in general $\sim$ 15% higher than the corresponding Chandra number. For the rest of the sources we used a fixed $\Gamma = 1.8$ as was done for the Chandra objects. The absorptions, fluxes and luminosities were in good agreement between the two datasets.

3.6.4 Brief summary from the comparison

From the presented analysis the most important conclusion is, that for the proper analysis of the less absorbed sources we really need to have a soft part of the spectrum in order to properly model the absorption and to obtain realistic power law slopes. Only in this way we can classify our sources as absorbed or unabsorbed. Due to the limiting energy band for the Chandra analysis (start from 0.6 keV, and sufficient

sensitivity - from 1 keV), the sources with low values of absorption appear different in the Chandra and XMM analysis (i.e they are fitted using different values of Γ and $N_{\rm H}$). This is particularly important for the spectra with good statistics and high signal-to-noise ratio because the spectra obtained with both satellites show small errors and believable values for the parameters. However, the detected differences are simply due to the fact that we see two different parts of the spectra. A typical example of such a discrepancy is discussed in the type-1 subsection, where we show that depending on the used energy range we can obtaine an order of magnitude difference for the absorption and a significant difference in the power law slope.

3.7 Conclusions

In this Chapter we presented the results of a detailed X-ray spectral analysis of the sample of 127 sources from the XMM-Newton deep survey in the CDFS. Using optical source identification and redshift information, we explored both the physical properties of individual sources, and the general properties of two AGN classes. For each of our sources we performed a spectral fitting with different models in order to investigate the complexity of AGN spectra, for example soft excess, iron line, absorption edge, etc. We fit pn and MOS spectra simultaneously in the 0.2–10 keV band using appropriate response matrixes (`arf` and `rmf`). Our main results are follows:

Most AGN spectra required only an (un)absorbed power law model, however we detect a fraction of the sources with additional spectral components such as a soft excess (11 sources) and iron line (7 sources).

No obvious correlation between spectral continuum and absorption or between Γ, $N_{\rm H}$ and redshift are found.

We observe a separation between the type-1 and the type-2 AGN as a consequence of different absorption column densities.

More than 90% of the source spectra are in agreement with the unified model, however a fraction of 'atypical' sources (absorbed type-1 AGN and unabsorbed type-2 AGN) was also discovered. Most of these 'atypical' objects have good signal-to-noise ratio which does not allow us to ascribe these properties to the poor spectra quality. The observed mismatch between X-ray and optical properties may be explained by a difference in the physical conditions surrounding the emission regions.

Optical spectra of X-ray absorbed sources have revealed a few examples of high-redshift, high-luminosity objects optically classified as BLAGN.

For the first time derived an integrated spectrum of the most distant type-2 QSOs, showing a strong X-ray absorption with a clear soft component (fitted with a scattering/partial covering model), which may imply that for the distant ($z > 2.5$) type-2 QSOs this component is required. An additional feature, a clear low hump at energy 1.35–1.86 kev in the observed frame, is clearly seen in our spectrum as well. The most plausible explanation of this feature would be that it is a smeared iron line, because the redshifts of the individual sources are in a broad range of 2.56 to 3.77.

We confirm a progressive hardening for the combined integrated spectra for faint objects, which at first was noted in the Chandra analysis of CDFS. However, the

detailed comparison of $\langle\Gamma\rangle$ values shows that the spectral slopes determined from XMM-Newton data are steeper typically by 0.1 than these detected by Chandra, even if exactly the same energy range (1–7 keV) is used by both instruments. The discrepancy becomes even larger if the soft 0.3–1 keV energy range is included in the fitting.

The comparison between Chandra and XMM-Newton fitting strategy reveals that there is a strong dependence between the obtained spectral slope and absorption in the selected energy range for spectral fitting. As a result, for sources exhibiting low intrinsic absorption Chandra, due to the limited energy range, obtained systematically higher values of the absorption columns and consequently flatter power law slopes.

Table 3.1: Best fit parameters for the whole sample of identified sources in the CDFS. ID corresponds to Chandra catalog (Giacconi et al. 2002). Redshift and optical class determined from optical spectroscopy (Szokoly et al. 2004), otherwise it photometric and taken from Zheng et al. (2004). N_H in units of 10^{22} cm^{-2}. Flux have been measured in 0.5–2 and 2–10 keV band and present in units of erg cm^{-2} s^{-1}. The 0.5–2 and 2–10 keV luminosities are corrected for absorption and given in units of erg s^{-1}.

ID	z	optical class	Γ	N_H	$F_{0.5-2}$	F_{2-10}	$L_{0.5-2}$	L_{2-10}
1	0.347	AGN II	$1.65^{+0.15}_{-0.14}$	$0.37^{+0.08}_{-0.08}$	1.74×10^{-15}	5.40×10^{-15}	9.87×10^{41}	2.03×10^{42}
2	0.730	AGN I	$1.82^{+0.20}_{-0.14}$	$0^{+0.08}$	1.65×10^{-15}	2.65×10^{-15}	3.48×10^{42}	5.87×10^{42}
4	1.260	AGN I	$2.30^{+0.12}_{-0.11}$	$0.26^{+0.13}_{-0.09}$	3.79×10^{-15}	3.29×10^{-15}	4.88×10^{43}	4.24×10^{43}
6	2.460	QSO I	$1.65^{+0.19}_{-0.28}$	$0.48^{+0.96}_{-0.47}$	1.90×10^{-15}	4.27×10^{-15}	4.65×10^{43}	1.33×10^{44}
7	1.840	QSO I	$1.86^{+0.05}_{-0.04}$	$0^{+0.01}$	2.05×10^{-14}	3.02×10^{-14}	3.52×10^{44}	6.37×10^{44}
8	0.990	AGN II	$1.67^{+0.16}_{-0.14}$	$1.00^{+0.22}_{-0.23}$	2.75×10^{-15}	8.76×10^{-15}	3.97×10^{42}	3.48×10^{43}
9	1.990	QSO I	$2.03^{+0.07}_{-0.05}$	$0^{+0.004}$	6.54×10^{-15}	7.40×10^{-15}	1.56×10^{44}	2.27×10^{44}
10^s	0.424	AGN II	$1.59^{+0.55}_{-0.25}$	$2.00^{+1.26}_{-0.98}$	8.60×10^{-16}	4.93×10^{-15}	1.31×10^{42}	2.98×10^{42}
11	2.579	QSO I	$1.93^{+0.04}_{-0.05}$	$0^{+0.05}$	5.94×10^{-15}	7.92×10^{-15}	2.08×10^{44}	3.99×10^{44}
12	0.251	AGN I	$2.30^{+0.90}_{-0.30}$	$0.08^{+0.15}_{-0.07}$	5.45×10^{-16}	3.28×10^{-16}	1.40×10^{41}	7.27×10^{40}
13	0.733	AGN I	$2.00^{+0.08}_{-0.08}$	$0.012^{+0.04}_{-0.003}$	3.63×10^{-15}	4.36×10^{-15}	8.69×10^{42}	1.09×10^{43}
15	1.227	AGN I	$2.03^{+0.12}_{-0.12}$	$0.30^{+0.09}_{-0.08}$	3.20×10^{-15}	4.18×10^{-15}	3.01×10^{43}	3.85×10^{43}
18	0.979	QSO I	$1.63^{+0.07}_{-0.08}$	$1.13^{+0.21}_{-0.10}$	7.32×10^{-15}	2.61×10^{-14}	4.29×10^{43}	1.02×10^{44}
19^b	0.740	AGN I	$2.00^{+0.04}_{-0.04}$	$0.05^{+0.01}_{-0.01}$	9.84×10^{-15}	1.23×10^{-14}	2.97×10^{43}	3.15×10^{43}
20	1.016	AGN II	$2.18^{+0.32}_{-0.19}$	$6.53^{+2.32}_{-1.52}$	7.65×10^{-16}	3.79×10^{-15}	2.67×10^{43}	2.69×10^{43}
21	3.476	QSO I	1.80^*	$0^{+0.83}$	1.85×10^{-16}	2.98×10^{-16}	8.37×10^{42}	2.51×10^{43}
22	1.92	QSO I	$1.97^{+0.06}_{-0.06}$	$0^{+0.01}$	3.93×10^{-15}	4.89×10^{-15}	8.21×10^{43}	1.29×10^{44}
23	0.730	AGN I	$1.86^{+0.18}_{-0.16}$	$0^{+0.04}$	9.81×10^{-16}	1.44×10^{-15}	2.13×10^{42}	3.30×10^{42}
24	3.61	QSO I	$1.72^{+0.10}_{-0.11}$	$0.21^{+0.52}_{-0.20}$	1.93×10^{-15}	3.55×10^{-15}	8.54×10^{43}	2.88×10^{44}
25	2.26	QSO II	$1.50^{+0.26}_{-0.32}$	$16.2^{+5.90}_{-6.60}$	7.70×10^{-16}	5.59×10^{-15}	4.69×10^{43}	1.42×10^{44}
26	1.650	AGN I	$1.61^{+0.34}_{-0.28}$	$3.38^{+2.53}_{-1.65}$	9.26×10^{-16}	3.83×10^{-15}	1.83×10^{43}	4.86×10^{43}
27	3.064	QSO II	$1.79^{+0.49}_{-0.49}$	$44.8^{+21.1}_{-21.1}$	4.23×10^{-16}	3.41×10^{-15}	8.70×10^{43}	2.44×10^{44}
29^s	0.300	AGN II	$1.83^{+0.10}_{-0.16}$	$4.73^{+0.67}_{-0.62}$	2.11×10^{-15}	2.75×10^{-14}	6.01×10^{42}	9.38×10^{42}
30	0.837	QSO I	$2.05^{+0.04}_{-0.03}$	0	9.69×10^{-15}	1.89×10^{-14}	3.25×10^{43}	6.78×10^{43}
31	1.603	QSO II	$2.14^{+0.06}_{-0.07}$	$1.43^{+0.15}_{-0.15}$	6.74×10^{-15}	9.74×10^{-15}	1.68×10^{44}	1.96×10^{44}
32	0.664	AGN I	$1.81^{+0.09}_{-0.13}$	$0.04^{+0.05}_{-0.03}$	2.76×10^{-15}	4.53×10^{-15}	4.85×10^{42}	8.05×10^{42}
33	0.665	AGN I	$1.90^{+0.10}_{-0.14}$	$0.30^{+0.08}_{-0.08}$	2.24×10^{-15}	4.03×10^{-15}	5.17×10^{42}	7.56×10^{42}
34	0.839	AGN I	$2.22^{+0.38}_{-0.31}$	$0.98^{+0.39}_{-0.34}$	1.36×10^{-15}	2.15×10^{-15}	9.46×10^{42}	8.74×10^{42}
35^s	1.512	QSO II	$1.62^{+0.08}_{-0.12}$	$5.50^{+1.15}_{-0.99}$	3.91×10^{-15}	2.15×10^{-14}	8.52×10^{43}	2.26×10^{44}
36	1.030	AGN I	$1.81^{+0.36}_{-0.45}$	$1.38^{+1.25}_{-0.66}$	6.68×10^{-16}	1.86×10^{-15}	5.62×10^{42}	9.63×10^{42}
37	0.960	AGN I	1.80^*	$0^{+0.07}$	9.66×10^{-16}	1.56×10^{-15}	3.95×10^{42}	6.85×10^{42}
38	0.738	AGN I	$2.23^{+0.09}_{-0.06}$	0	3.66×10^{-15}	7.69×10^{-15}	1.01×10^{43}	2.21×10^{43}
39	1.218	QSO I	$2.19^{+0.04}_{-0.04}$	0	9.54×10^{-15}	8.54×10^{-15}	8.69×10^{43}	8.75×10^{43}
40	0.550	AGN I	$1.95^{+0.11}_{-0.14}$	$0.09^{+0.06}_{-0.05}$	3.50×10^{-15}	5.04×10^{-15}	4.55×10^{42}	6.10×10^{42}
41^s	0.667	AGN II	$1.76^{+0.16}_{-0.19}$	$5.70^{+1.75}_{-1.40}$	1.58×10^{-15}	1.08×10^{-14}	1.18×10^{43}	2.19×10^{43}
42^b	0.734	QSO I	$2.03^{+0.02}_{-0.03}$	0	5.21×10^{-14}	5.88×10^{-14}	1.40×10^{44}	1.50×10^{44}
44^b	1.031	QSO I	$2.45^{+0.04}_{-0.04}$	$0^{+0.004}$	2.69×10^{-14}	1.58×10^{-14}	2.85×10^{44}	1.27×10^{44}
45	2.291	QSO II	$2.14^{+1.51}_{-0.28}$	$10.85^{+4.65}_{-5.75}$	1.14×10^{-15}	4.74×10^{-15}	7.50×10^{43}	1.55×10^{44}
46	1.617	QSO I	$2.29^{+0.32}_{-0.24}$	$0.57^{+0.41}_{-0.3}$	1.94×10^{-15}	1.80×10^{-15}	4.54×10^{43}	4.26×10^{43}
48	1.260	AGN II	$1.59^{+0.23}_{-0.18}$	$3.85^{+1.64}_{-1.04}$	1.16×10^{-15}	6.31×10^{-15}	1.76×10^{43}	4.43×10^{43}
49	0.534	AGN I	$2.10^{+0.14}_{-0.15}$	$0.10^{+0.07}_{-0.06}$	2.22×10^{-15}	2.59×10^{-15}	2.92×10^{42}	3.12×10^{42}
50	0.67	AGN II	$1.71^{+0.37}_{-0.33}$	$0.91^{+0.59}_{-0.41}$	7.01×10^{-16}	2.35×10^{-15}	2.06×10^{42}	4.09×10^{42}
51	1.097	QSO II	$1.96^{+0.67}_{-0.45}$	$29.0^{+10.50}_{-10.31}$	2.63×10^{-16}	1.16×10^{-14}	7.85×10^{43}	1.09×10^{44}
52	0.569	AGN I	$2.18^{+0.07}_{-0.07}$	$0.05^{+0.03}_{-0.02}$	5.04×10^{-15}	4.82×10^{-15}	7.47×10^{42}	7.04×10^{42}
53	0.675	AGN I	$1.96^{+0.15}_{-0.16}$	$0.03^{+0.07}_{-0.02}$	2.73×10^{-15}	3.53×10^{-15}	5.33×10^{42}	7.06×10^{42}
54	2.561	QSO II	1.80^*	$43.6^{+22.43}_{-15.3}$	3.51×10^{-16}	3.38×10^{-15}	1.58×10^{43}	1.53×10^{44}
55	0.122	AGN II	$1.33^{+0.17}_{-0.53}$	$1.20^{+0.27}_{-0.81}$	9.76×10^{-16}	1.15×10^{-14}	8.37×10^{40}	4.18×10^{41}

Table 3.1: Continued

ID	z	optical class	Γ	N_H	$F_{0.5-2}$	F_{2-10}	$L_{0.5-2}$	L_{2-10}
56	0.605	AGN II	$1.39^{+0.2}_{-0.12}$	$0.73^{+0.25}_{-0.20}$	2.12×10^{-15}	1.12×10^{-14}	3.88×10^{42}	1.36×10^{43}
57	2.562	QSO II	$1.49^{+0.04}_{-0.7}$	$12.5^{+4.10}_{-3.10}$	1.05×10^{-15}	6.03×10^{-15}	4.23×10^{43}	1.84×10^{44}
58	0.92	AGN I	$1.55^{+0.55}_{-0.25}$	$0.80^{+0.92}_{-0.55}$	6.51×10^{-16}	2.36×10^{-15}	2.82×10^{42}	7.63×10^{42}
59	0.970	AGN I	$1.67^{+0.12}_{-0.13}$	$1.98^{+0.50}_{-0.37}$	2.29×10^{-15}	9.34×10^{-15}	1.84×10^{43}	3.85×10^{43}
60	1.615	QSO I	$1.89^{+0.06}_{-0.04}$	$0^{+0.07}$	7.01×10^{-15}	9.79×10^{-15}	9.45×10^{43}	1.57×10^{44}
61	2.02	QSO I	$2.12^{+0.09}_{-0.09}$	$1.75^{+0.29}_{-0.29}$	5.92×10^{-15}	8.29×10^{-15}	2.26×10^{44}	2.94×10^{44}
62[s]	2.81	QSO I	$2.03^{+0.19}_{-0.19}$	$17.5^{+4.8}_{-4.3}$	2.55×10^{-15}	6.75×10^{-15}	2.93×10^{44}	5.18×10^{44}
63	0.544	QSO I	$1.96^{+0.01}_{-0.01}$	$0.05^{+0.01}_{-0.01}$	7.64×10^{-14}	1.01×10^{-13}	9.25×10^{43}	1.20×10^{44}
64	0.130	AGN I	$2.17^{+0.10}_{-0.13}$	$0.29^{+0.04}_{-0.06}$	3.63×10^{-15}	6.02×10^{-15}	3.03×10^{41}	2.82×10^{41}
65	1.100	QSO I	$1.55^{+0.20}_{-0.19}$	$0.23^{+0.25}_{-0.21}$	1.97×10^{-15}	5.11×10^{-15}	9.89×10^{42}	2.51×10^{43}
66[s]	0.574	AGN II	$1.74^{+0.14}_{-0.22}$	$6.42^{+1.34}_{-1.35}$	1.32×10^{-15}	1.51×10^{-14}	1.18×10^{43}	2.16×10^{43}
67	1.616	QSO I	$1.69^{+0.06}_{-0.07}$	$0.03^{+0.08}_{-0.02}$	6.51×10^{-15}	1.25×10^{-14}	7.36×10^{43}	1.64×10^{44}
68	2.726	QSO I	$1.69^{+0.21}_{-0.16}$	$0.80^{+0.98}_{-0.73}$	1.88×10^{-15}	3.92×10^{-15}	5.89×10^{43}	1.66×10^{44}
69	0.850	AGN I	$1.28^{+0.32}_{-0.19}$	$1.95^{+0.95}_{-0.72}$	2.04×10^{-15}	1.54×10^{-14}	9.45×10^{42}	3.62×10^{43}
70[s]	1.070	AGN II	$1.27^{+0.33}_{-0.21}$	$20.5^{+6}_{-5.7}$	1.19×10^{-15}	1.84×10^{-14}	2.17×10^{43}	8.38×10^{43}
71	1.037	AGN I	$2.22^{+0.06}_{-0.05}$	0	7.62×10^{-15}	6.52×10^{-15}	4.79×10^{43}	4.50×10^{43}
72	1.990	QSO I	$1.64^{+0.14}_{-0.14}$	$4.90^{+1.39}_{-0.98}$	2.81×10^{-15}	1.10×10^{-14}	8.69×10^{43}	2.24×10^{44}
73	0.734	AGN I	$1.86^{+0.13}_{-0.13}$	$0.25^{+0.10}_{-0.10}$	3.07×10^{-15}	5.51×10^{-15}	8.26×10^{42}	1.28×10^{43}
74	0.650	AGN I	$1.66^{+0.22}_{-0.21}$	$0^{+0.04}$	1.52×10^{-15}	3.03×10^{-15}	2.28×10^{42}	4.74×10^{42}
75	0.737	AGN II	$2.37^{+0.66}_{-0.45}$	$20.9^{+7.9}_{-5.9}$	3.15×10^{-16}	1.16×10^{-14}	1.03×10^{44}	6.65×10^{43}
76	2.394	QSO II	$1.94^{+0.12}_{-0.21}$	$19.7^{+4.8}_{-3.6}$	2.45×10^{-15}	1.18×10^{-14}	3.02×10^{44}	5.58×10^{44}
77	0.622	AGN I	$2.29^{+0.28}_{-0.31}$	$0.07^{+0.12}_{-0.07}$	1.38×10^{-15}	1.17×10^{-15}	2.75×10^{42}	2.25×10^{42}
78	0.960	AGN I	$2.23^{+0.05}_{-0.06}$	$0^{+0.01}$	2.78×10^{-15}	2.38×10^{-15}	1.45×10^{43}	1.35×10^{43}
79	1.82	AGN I	$1.90^{+0.55}_{-0.47}$	$0.32^{+0.78}_{-0.31}$	4.47×10^{-16}	6.44×10^{-16}	8.42×10^{42}	1.44×10^{43}
80	1.700	AGN I	$1.42^{+0.28}_{-0.16}$	$0^{+0.25}$	1.08×10^{-15}	3.75×10^{-15}	9.21×10^{42}	3.73×10^{43}
83	1.760	AGN I	$1.83^{+0.18}_{-0.17}$	$0^{+0.05}$	1.46×10^{-15}	2.25×10^{-15}	2.22×10^{43}	4.14×10^{43}
84	0.103	Gal	$2.35^{+0.18}_{-0.18}$	$0^{+0.003}$	2.18×10^{-15}	1.55×10^{-15}	6.09×10^{40}	4.35×10^{40}
87	2.801	AGN I	1.80*	$0^{+0.23}$	7.61×10^{-16}	1.52×10^{-15}	2.24×10^{43}	6.52×10^{43}
89	2.470	AGN I	1.80*	$0.16^{+1.37}_{-0.15}$	3.86×10^{-16}	6.35×10^{-16}	1.05×10^{43}	2.48×10^{43}
91	3.193	QSO I	$1.76^{+0.25}_{-0.29}$	$0.65^{+1.22}_{-0.64}$	5.62×10^{-16}	1.01×10^{-15}	2.27×10^{43}	6.69×10^{43}
94	2.688	AGN I	1.80*	$0.30^{+1.81}_{-0.29}$	4.15×10^{-16}	6.93×10^{-16}	1.40×10^{43}	3.28×10^{43}
97	0.181	Gal	$1.60^{+0.19}_{-0.12}$	$0^{+0.012}$	1.75×10^{-15}	3.62×10^{-15}	1.51×10^{41}	3.16×10^{41}
98	0.279	Gal	1.80*	$0^{+0.008}$	5.47×10^{-16}	8.80×10^{-16}	1.27×10^{41}	2.08×10^{41}
99	0.790	AGN I	$1.86^{+0.20}_{-0.24}$	$1.48^{+0.45}_{-0.42}$	2.46×10^{-15}	7.71×10^{-15}	1.42×10^{43}	2.20×10^{43}
101	1.625	AGN I	1.80*	$0.22^{+20}_{-0.21}$	3.34×10^{-16}	5.74×10^{-16}	4.48×10^{42}	8.51×10^{42}
116	0.076	Gal	$1.96^{+0.14}_{-0.14}$	$0^{+0.036}$	1.79×10^{-15}	2.31×10^{-15}	2.58×10^{40}	3.27×10^{40}
117	2.573	AGN I	$2.10^{+2.36}_{-0.17}$	$0^{+3.58}$	3.67×10^{-16}	5.95×10^{-16}	1.93×10^{43}	2.55×10^{43}
121	0.674	AGN II	$1.91^{+0.26}_{-0.41}$	$1.25^{+0.88}_{-0.49}$	8.85×10^{-16}	2.62×10^{-15}	3.64×10^{42}	5.23×10^{42}
138	0.972	AGN I	$2.05^{+0.21}_{-0.16}$	$0^{+0.06}$	1.55×10^{-15}	1.75×10^{-15}	7.51×10^{42}	9.06×10^{42}
145[s]	1.50	AGN II	$2.00^{+0.15}_{-0.32}$	$20.00^{+4.98}_{-5.21}$	6.21×10^{-16}	4.51×10^{-15}	5.90×10^{43}	8.14×10^{43}
147	0.990	AGN II	1.80*	$23.4^{+6.1}_{-4.5}$	1.46×10^{-16}	6.59×10^{-15}	2.37×10^{43}	4.11×10^{43}
151	0.604	AGN II	1.80*	$23.3^{+22.2}_{-11.8}$	1.06×10^{-17}	2.29×10^{-15}	3.08×10^{42}	5.15×10^{42}
159	3.300	QSO I	$1.74^{+0.09}_{-0.15}$	$6.27^{+1.98}_{-1.21}$	2.80×10^{-15}	7.37×10^{-15}	1.67×10^{44}	5.13×10^{44}
176	0.786	AGN I	$1.81^{+0.2}_{-0.14}$	$0.11^{+0.12}_{-0.10}$	1.74×10^{-15}	2.98×10^{-15}	4.78×10^{42}	7.96×10^{42}
200	0.85	AGN II	$1.45^{+0.16}_{-0.13}$	$0.02^{+0.11}_{-0.01}$	1.18×10^{-15}	3.29×10^{-15}	2.89×10^{42}	8.42×10^{42}
201	0.679	AGN II	1.80*	$1.98^{+0.83}_{-0.62}$	5.56×10^{-16}	2.43×10^{-15}	2.81×10^{42}	4.74×10^{42}
202	3.7	QSO II	1.80*	$51^{+19.9}_{-15.3}$	2.81×10^{-16}	1.96×10^{-15}	5.54×10^{43}	2.09×10^{44}
203	1.170	AGN I	$1.49^{+0.07}_{-0.05}$	$0^{+0.03}$	5.96×10^{-15}	1.52×10^{-14}	2.93×10^{43}	8.20×10^{43}
206	1.324	QSO I	$2.50^{+0.10}_{-0.10}$	$0.06^{+0.04}_{-0.04}$	1.43×10^{-14}	1.51×10^{-14}	2.22×10^{44}	2.06×10^{44}
207	0.40	AGN II	$1.93^{+0.30}_{-0.11}$	$3.49^{+0.95}_{-0.85}$	6.05×10^{-15}	4.90×10^{-14}	4.42×10^{43}	3.61×10^{43}
208	0.720	AGN I	$1.68^{+0.11}_{-0.11}$	$0^{+0.01}$	2.98×10^{-15}	5.74×10^{-15}	5.69×10^{42}	1.15×10^{43}

Table 3.1: Continued

ID	z	optical class	Γ	N_H	$F_{0.5-2}$	F_{2-10}	$L_{0.5-2}$	L_{2-10}
209	1.320	QSO I	$1.94^{+0.11}_{-0.10}$	$1.29^{+0.31}_{-0.23}$	7.48×10^{-15}	1.52×10^{-14}	1.05×10^{44}	1.57×10^{44}
213	0.60	AGN II	$1.77^{+0.45}_{-0.29}$	$0.93^{+0.74}_{-0.37}$	9.26×10^{-16}	2.99×10^{-15}	2.39×10^{42}	4.19×10^{42}
219	1.730	QSO I	$1.77^{+0.79}_{-0.60}$	$3.18^{+3.01}_{-1.79}$	6.99×10^{-16}	2.12×10^{-15}	1.68×10^{43}	3.61×10^{43}
220	1.4	AGN I	$1.98^{+0.19}_{-0.15}$	$0^{+0.10}$	9.22×10^{-16}	1.34×10^{-15}	1.20×10^{43}	1.71×10^{43}
224	0.738	Gal	1.80*	$0.02^{+0.08}_{-0.01}$	7.48×10^{-16}	1.01×10^{-15}	1.64×10^{42}	2.78×10^{42}
227	2.18	AGN II	1.80*	$4.05^{+4.96}_{-2.82}$	6.76×10^{-16}	1.84×10^{-15}	2.63×10^{43}	5.52×10^{43}
230	2.174	AGN I	1.80*	$0.29^{+0.88}_{-0.28}$	4.36×10^{-16}	7.36×10^{-16}	9.94×10^{42}	2.15×10^{43}
238	1.065	AGN I	$1.99^{+0.31}_{-0.26}$	$0^{+0.11}$	1.42×10^{-15}	1.73×10^{-15}	8.12×10^{42}	1.17×10^{43}
242	1.027	AGN I	$1.73^{+0.47}_{-0.33}$	$0^{+0.10}$	7.81×10^{-16}	1.40×10^{-15}	3.43×10^{42}	6.65×10^{42}
243	2.50	QSO II	1.80*	$20.0^{+21.9}_{-10.64}$	1.59×10^{-16}	8.52×10^{-16}	1.43×10^{43}	3.75×10^{43}
246	0.710	AGN I	1.80*	$0^{+0.10}$	4.98×10^{-16}	8.02×10^{-16}	9.83×10^{41}	1.66×10^{42}
247	0.038	Gal	1.80*	$0.33^{+0.26}_{-0.18}$	2.63×10^{-16}	8.37×10^{-16}	1.73×10^{39}	2.79×10^{39}
264	1.316	AGN II	1.80*	$17.9^{+22.1}_{-17.78}$	7.21×10^{-17}	1.07×10^{-15}	6.36×10^{42}	1.15×10^{43}
268	1.222	AGN II	1.80*	$0.01^{+0.69}_{-0.001}$	3.16×10^{-16}	5.41×10^{-16}	2.20×10^{42}	3.89×10^{42}
501	0.810	AGN I	$1.82^{+0.10}_{-0.13}$	$0.02^{+0.07}_{-0.01}$	2.08×10^{-15}	3.40×10^{-15}	5.71×10^{42}	9.59×10^{42}
503	0.540	AGN I	$1.85^{+0.08}_{-0.06}$	$0.03^{+0.03}_{0.01}$	7.17×10^{-15}	1.11×10^{-14}	7.94×10^{42}	1.23×10^{43}
504	0.52	AGN II	$1.90^{+0.71}_{-0.30}$	$0.02^{+0.15}_{-0.01}$	4.41×10^{-16}	6.13×10^{-16}	4.41×10^{41}	6.33×10^{41}
506	3.690	QSO I	1.80*	$5.84^{+6.67}_{-3.34}$	4.24×10^{-16}	9.42×10^{-16}	2.47×10^{43}	9.16×10^{43}
514	0.103	Gal	1.80*	$0.16^{+1.84}_{-0.15}$	2.35×10^{-16}	5.16×10^{-16}	8.56×10^{39}	1.39×10^{40}
517	2.330	QSO I	$1.36^{+0.24}_{-0.26}$	$2.78^{+1.46}_{-1.18}$	1.69×10^{-15}	8.24×10^{-15}	3.16×10^{43}	1.50×10^{44}
539	0.977	AGN I	$1.97^{+0.09}_{-0.07}$	$0.06^{+0.05}_{-0.05}$	7.44×10^{-15}	1.06×10^{-14}	3.57×10^{43}	5.29×10^{43}
545	0.97	AGN II	$1.82^{+0.30}_{-0.16}$	$0.03^{+0.11}_{-0.02}$	1.80×10^{-15}	2.79×10^{-15}	7.39×10^{42}	1.24×10^{43}
548	1.44	AGN I	$1.41^{+0.50}_{-0.37}$	$0.22^{+0.87}_{-0.21}$	1.06×10^{-15}	3.26×10^{-15}	7.69×10^{42}	2.50×10^{43}
550	1.930	AGN I	$1.83^{+0.09}_{-0.07}$	$0^{+0.03}$	3.92×10^{-15}	5.94×10^{-15}	7.24×10^{43}	1.37×10^{44}
552	0.673	Gal	1.80*	$0^{+0.02}$	1.86×10^{-16}	3.40×10^{-16}	3.24×10^{41}	6.65×10^{41}
566	0.734	Gal	1.80*	$0^{+0.02}$	3.36×10^{-16}	5.41×10^{-16}	7.16×10^{41}	1.21×10^{42}
571	1.44	Gal	1.80*	$0.50^{+0.93}_{-0.45}$	6.38×10^{-16}	1.23×10^{-15}	2.78×10^{42}	1.32×10^{43}
611	0.979	AGN II	1.80*	$49.2^{+40.6}_{-24.6}$	4.61×10^{-18}	1.81×10^{-15}	8.22×10^{42}	1.43×10^{43}
641	0.74	AGN II	$1.77^{+0.29}_{-0.46}$	$1.54^{+0.72}_{-0.66}$	1.38×10^{-15}	5.16×10^{-15}	6.74×10^{42}	1.19×10^{43}

[s] AGN with the soft component in their spectra modelled with a scattering or partial covering model

[b] AGN with the soft excess in their spectra modelled with a blackbody model

* fixed

Chapter 4

A relativistic Fe line in the mean X-ray spectra of type-1 and type-2 AGN

4.1 Introduction

As was intensively discussed in Section 1.4, the understanding of the origin of the iron line and determination of its profile is one of the important tasks in X-ray astronomy. So far, in most of the AGN we can detect the narrow Fe K_α line at 6.4 keV (rest-frame), interpreting it as a fluorescence from cold matter (Pounds et al. 1989). This neutral iron line is believed to be due to illumination of a torus or the outermost parts of an accretion disc (e.g. Pounds et al. 1990) by hard X-ray photons from the accretion disc corona. In some cases we can observe additionally a line profile consistent with the emission from matter moving at relativistic velocities in a disc-like configuration. Using specific line models we can determine the important parameters, such as the black hole spin, the emissivity profile, inclination and ionization state of the disc. However, to test such complex models we need high quality data, which we can obtain only for nearby bright objects. For high-z sources, frequently only a narrow component is observed in the Fe line, and the analysis of the broad, relativistic component is often hampered by systematic uncertainties in modelling the continuum. There is some evidence (e.g. Comastri et al. 2004) that the relativistic iron line is present, at least in some distant AGN as well. However, it was unclear how significant was the presence of this component in general for the high-z population of AGN.

The X-ray results discussed in this chapter are obtained from the longest and most sensitive observation of the X-ray background by *XMM-Newton*, a 770 ksec observation of the Lockman Hole (Hasinger 2004). This is a special region in the sky with an extremely low Galactic hydrogen column density, $N_{\rm H} = 5.7 \times 10^{19}$ cm^{-2} (Lockman et al. 1986). The fraction of optically identified sources with redshifts and a sufficient number of X-ray photons is quite high in this field, so that for the first time we are able to analyse the mean rest-frame spectra for a representative sample of type-1 and type-2 AGN at considerable redshifts. The obtained results can significantly improve our knowledge and understanding of the nature of the iron line in the spectra of distant AGN. The remaining part of this chapter is largely based on the work presented by

Streblyanska et al. (2005), A&A, 432, 395.

4.2 Observations and data reduction

The deepest *XMM-Newton* observation has been carried out in the Lockman Hole field, that is centred on the sky position RA: 10:52:43 and DEC: +57:28:48 (J2000). The data were obtained by adding 16 observations obtained in three periods from 2000 to 2002 (in the PV [EPIC-Payload Verification Phase], and AO1 and AO2 [the first and second Announcement of Opportunity] phases). The 16 XMM-Newton observations gave a total exposure (after removal of periods of high background) of $\sim$ 850 ksec for MOS1 and MOS2 detectors and $\sim$650 ksec for pn. Some AO2 observations have an offset of more than $\sim$25 arcmin from the centre of the field. This means that the total exposure time in the centre of the field is smaller, but the total solid angle covered by the observations is increased. The pn and MOS data were preprocessed by the *XMM Survey Science Centre* with the XMM standard Science Analysis System (SAS, version 5.4) routines, using the latest calibration data. Spurious noise events not created by X-rays were filtered from the event files using the XMM-Newton pipeline standard filtering. We have cleaned the event files of the individual observations from periods of high background due to soft high background flares. For each observation and detector we built light curves (histograms of counts as a function of time). The light curves were visually inspected to search for time intervals affected by high flaring background periods. Thresholds in count rate were determined separately for each observation and camera.

Due to the large offset between the different observations of the field and different filters for each, we did not merge the event files. We extracted the products (images, exposure maps and background maps) for each individual observation, detector and energy band, and then, we combined them to obtain the total observation of the field for each X-ray detector and energy band.

An automated procedure has been used to obtain for each individual object the spectrum of the total observation, hereafter, the time average spectrum of the sources. In addition a background spectrum and a response calibration matrix have also been generated by combining individual products from each exposure.

First we have extracted the spectra of each object for each detector (pn, MOS1 and MOS2) and observation. We used the coordinates of the objects (RA and Dec) that we obtained from the source detection process, and the SAS task region to define the source and background extraction regions. The first was defined as a circle with a radius that varied depending on the position of the source within the detector. We extracted the background for each object in an annulus centred on the source position. The task `region` checks the source and background regions for overlapping with neighbouring sources. If overlapping exists, then, the size of the source region is reduced until it is removed. For the background regions, if neighbouring objects fall inside the background region they are masked out. Once the regions were defined, we used the SAS task `evselect` to extract from the event files the spectra of each object. Calibration matrices (`arf` and `rmf`) for each spectrum were obtained with SAS tasks

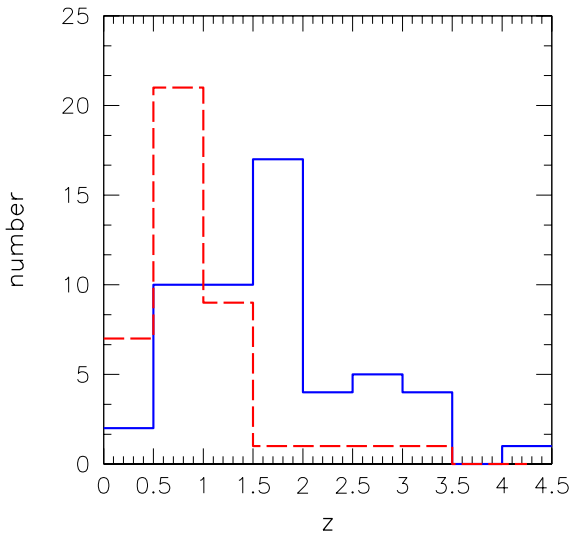

Figure 4.1: Redshift distribution of the LH X-ray sources in our selected sample. The blue solid and red dashed lines correspond to type-1 and type-2 AGN, respectively. Among type-2 AGNs, the objects at low redshifts ($z < 1$) constitute about 70%.

`arfgen` and `rmfgen`.
The last step was the combination of the spectral products of each source. Source and background spectra are obtained adding the counts for each channel. The areas used to extract the spectra and the response matrices were weighted with the exposure times of each individual observation.

We did not use the spectra from observations where the objects were near the borders of the FOV, or near CCD gaps or bad columns, because in these cases we found that the spectral products, specially the response matrices were often incorrect.

Complete information about the source products is described in detail by Mateos et al. (2005).

4.3 X-ray sample

Images, background maps and exposure maps were generated for each observation and detector individually in the standard 5 energy bands: 0.2–0.5, 0.5–2, 2–4.5, 4.5–7.5 and 7.5–12 keV. We ran the SAS source detection algorithm `eboxdetect-emldetect` on each instrument independently, using the five energy bands simultaneously. Afterwards we cross-correlated the pn source list with the lists obtained for MOS1 and MOS2 to build a complete unique catalogue of sources. As a last step we also cross-check our catalogue with the source catalogue by Mainieri et al. (2002) from the PV observation.

We selected a sample of 104 X-ray sources with spectroscopic identification and counts larger than 200 in the 0.2–10 keV band. A large fraction of the source identifi-

cation comes from the flux limited ROSAT 0.5–2 keV sample (Lehmann et al. 2001). The XMM-Newton observations cover a large solid angle and reveal additional sources due to the superb high energy response of the XMM-Newton detectors (the whole field source catalog will be presented by Brunner et al. 2006, in preparation). For newly detected XMM-Newton sources, some additional spectroscopic redshifts have been obtained with the LRIS and Deimos instruments at the Keck telescopes in 2001, 2003, and 2004 (PI: M. Schmidt and P. Henry). The spectroscopic and photometric identification of these objects will be presented in forthcoming papers by Szokoly et al. (2006, in preparation), and by Mainieri et al. (2006, in preparation), respectively.

Most of these sources have been analysed individually by Mainieri et al. (2002) based on 100 ksec XMM-Newton observations (PV phase). Mateos et al. (2005) present a detailed individual spectral analysis of the brightest sources, using the same data utilized in our analysis.

In the following we will refer to type-1 and type-2 objects using the optical spectroscopic classification (see for details Schmidt et al. 1998, Lehmann et al. 2001). Sources were classified depending on the properties of their UV/optical emission lines. The objects with UV/optical emission lines with FWHM > 1500 km s^{-1} in their optical spectra were classified as type 1 AGN. Sources that do not exhibit broad emission lines but that show Ne emission lines ([Ne V] and/or strong [Ne III]) were classified as type 2 AGN. Our final sample includes 53 type-1 AGN, 41 type-2 AGN and 10 galaxies.

4.4 Spectral analysis

The redshift distribution of the sources in our sample in shown in Fig. 4.1 and peaks at redshifts below 1 for type-2 AGN and close to 2 for type-1 AGN.

We used `XSPEC (v11.2)` for the spectral fitting analysis. All spectra have been extracted in the 0.2–10 keV band, MOS1 and MOS2 spectra have been merged. For every source we use a separate response matrix and ancillary response files.

For every object in our sample we fit the pn and MOS spectra with a single power law model modified by an intrinsic absorption, having the slope of the power law, its normalization and the absorbing column as free parameters. We save as ASCII files the ratio of the data to the model as well as a reconstructed unfolded spectrum. The next step consists of shifting the spectrum to the rest frame. For the ratio we simply increase the energies and its errors by the factor of $(1 + z)$. Analysis of the unfolded spectra is more complicated due to the different values of normalization for the different objects. In order to obtain all spectra in the same rest frame we need not only to shift the energy range but also renormalize each spectrum to the same value for further averaging. For this purpose we use the normalization value in the 2–10 keV rest frame energy band and divide each spectrum by this number.

We separate objects by spectral type (type-1 and type-2 AGN) and include in the corresponding ASCII files all the necessary information for further analysis (energy and normalization with corresponding errors). As a last step we convert each file to the spectrum in order to fit in `XSPEC` with different physical models. For this purpose we used a dummy response.

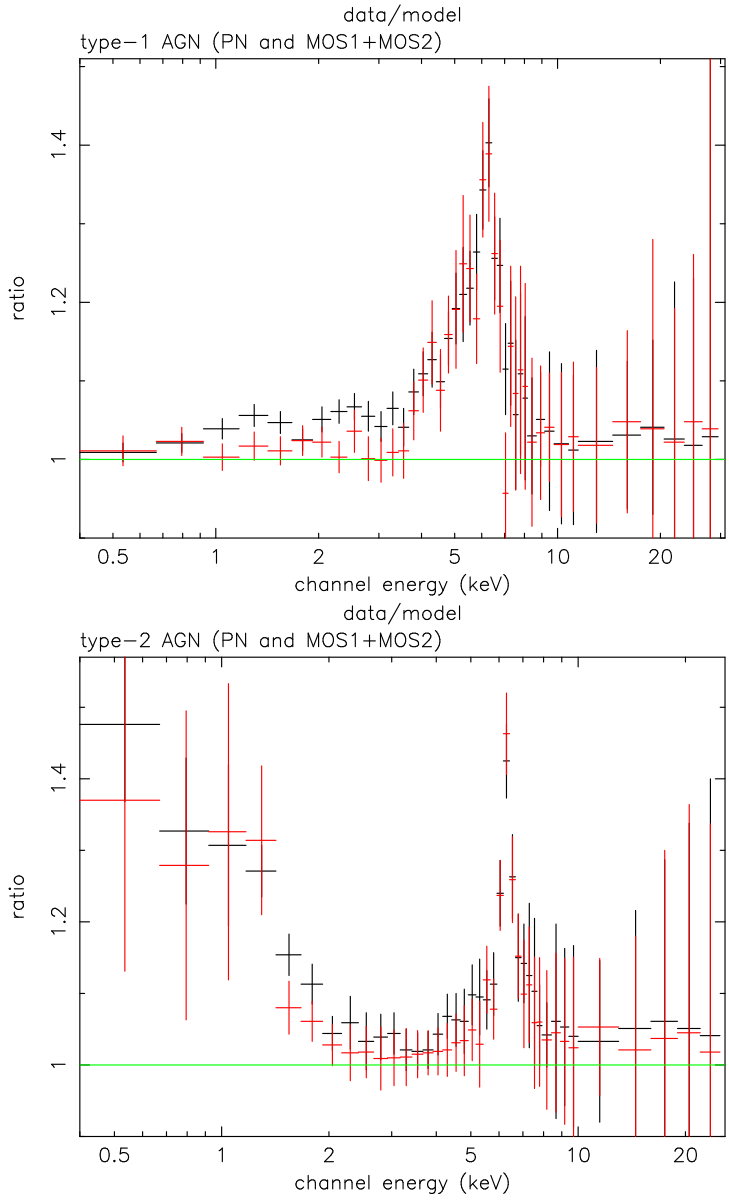

Figure 4.2: The resulting mean ratio plots from type-1 (upper plot) and type-2 (lower plot) AGN spectra. The plots were obtained by adding together all individual ratio plots shifted to the rest frame (see text for details). The EPIC-pn (black) and MOS (red) spectral data show a clear broad excess at 4–7 keV for type-1 AGN, and a more narrow component between 5 and 7 keV for type-2 AGN. An additional bright feature at low energies in type-2 AGN ratio corresponds, on the one hand, with improperly modelled absorption and, on the other hand, with the presence of a soft excess in the individual spectra. Since we do not specifically include a component to account for any possible soft excess in the individual spectra, the sources with this component contribute significantly to the mean ratio.

As the redshifts of the sources vary, their rest frame spectra have different energy boundaries. To provide an average spectrum, we select a common energy grid. We used a bin width of 0.25 keV for energies lower than 8 keV and a bin width 2 keV above. Such a choice is determined by the available counts. In a separate analysis, to study the Fe line profile in more detail, we rebinned the data using a binsize of 0.23 keV between 4 and 7 keV for the type-1 AGN spectra.

As the input spectra often have energy bins spread over two or more energy bins of the output spectrum, in such instance we use the Monte-Carlo method to choose the bin into which to add the data. As a final operation, we normalize the flux in each energy bin of the output spectrum by the number of points that were added to it. We propagate the errors accordingly.

Such an averaging is similar between the ratio and the unfolded spectra and both methods yield comparable results (see Fig.4.2 and Fig. 4.3–Fig. 4.4). As long as the redshifts of the objects in our sample are of order 1, it is possible to observe the rest frame averaged spectrum above 12 keV.

An important note for our method is that we obtained pn and MOS mean spectra of type-2 AGN without signature of absorption. Of course, individual spectra of type-2 objects have absorption with $N_{\rm H}$ larger than the fitted values to the stacked spectrum. But then, the objects with less absorption dominate the signal at low energies in the stacked spectra, and the fitted $N_{\rm H}$ value is actually dominated by these - and therefore very small. In other words, the average $N_{\rm H}$ in the individual sources is much higher than the $N_{\rm H}$ in the average spectrum of these sources. All this has effects on the underlying (average) Γ as well.

The unfolded spectrum for the type-2 AGN with skewed line wings looks similar to that of the type-1 AGN, except that an additional narrow iron line component at a rest energy of ~ 6.4 keV seems to be present in the type-2 AGN, but our statistics do not required this additional component to fit it.

The averaged spectra for both type-1 and type-2 AGN show a prominent spectral feature at 6.4 keV. We observed an excess in the data/model ratio between 4–7 keV for the both type-1 and type-2 AGN (Fig. 4.3 and Fig. 4.4).

Such a feature can be due either to a broad emission line or to complex absorption. For the latter we have modelled the spectrum in terms of a partially-covered source (e.g. Boller et al. 2003) and obtain a good fit for the following parameters: $\Gamma = 2^{+0.06}_{-0.05}$, $N_{\rm H} = 14^{+2}_{-2} \times 10^{22}$ cm^{-2} and covering fraction $= 0.4^{+0.05}_{-0.05}$. Such a strong partial-covering is usually not seen in nearby sources and to observe it in the average spectrum would require the individual sources to be very similar to each other. A variability analysis of the individual source components may be a useful test. In the remainder of this chapter we explore the broad emission line interpretation.

4.4.1 Origin of the broad line feature in the type-1 AGN spectrum

The energy of this broad line indicates that Fe atoms responsible for the line are in a low ionization state, with mean energy near 6.4 keV (in the rest-frame). Most probably such a broad and intense Fe K_α line is due to low (moderate) ionization

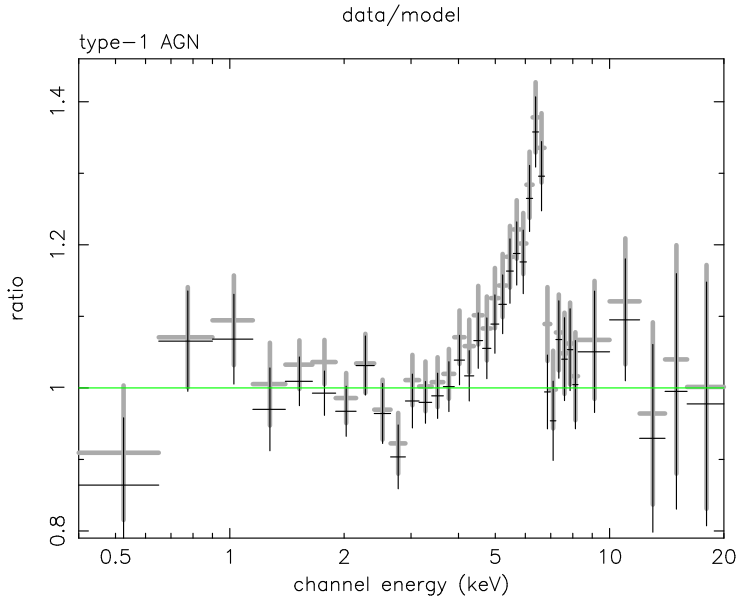

Figure 4.3: The resulting ratio plots from mean unfolded type-1 AGN spectra obtained by using averaging methods. The unfolded spectra are fit with a simple power-law model in the ranges 0.2–3 and 8–20 keV (excluding the portion of the spectrum where the emission associated with the relativistic Fe line is present). The EPIC-pn (grey) and MOS (black) spectral data show a clear broad excess at 4–8 keV in the rest-frame.

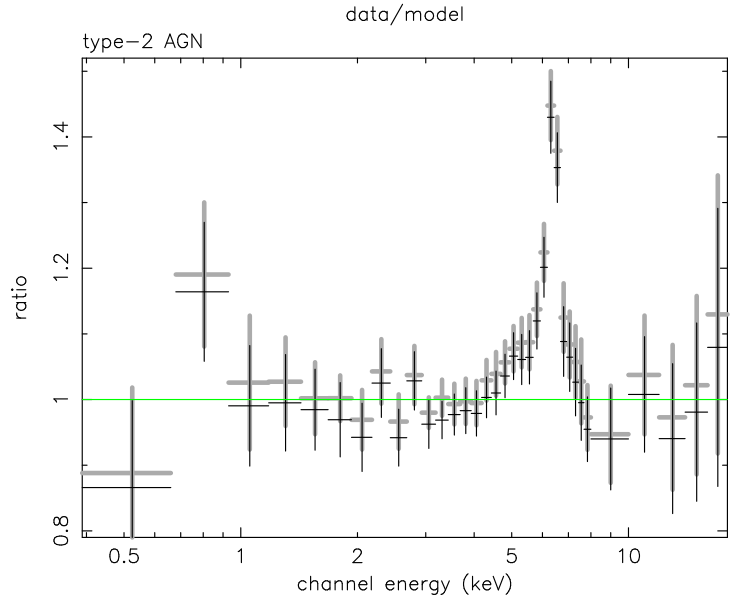

Figure 4.4: The 0.2–3 and 8–20 keV power-law model fits for the pn (grey) and MOS (black) type-2 AGN spectral data, showing a broad excess similar to type-1 AGN but in conjunction with a narrow component near 6.4 keV.

Table 4.1: Results of the spectral fitting in 0.4–20 keV band with a four-component model consisting of a power law and a line model with two absorption components, one representing intrinsic absorption (a free parameter during the fit) and the other was fixed at the Galactic column density of 5.7×10^{19} cm^{-2} *(wabs * wabs(po + linemodel)). The line models are Gaussian, diskline ((non-rotating BH) and laor (rotating BH). From our model fits, we computed the slope of a power law spectrum (photon index* Γ*), a intrinsic column density* $N_{\rm H}$ *(in units of* $\times 10^{20}$*) and the line parameters. We assumed fixed* $\beta = 2$ *for the diskline model and 3 for laor model. Note that the absorption obtained in the fit of the summed spectrum is heavily driven by the AGN of low absorbing column, and not equivalent to the averaging of the* $N_{\rm H}$ *values obtained individually. As a result of such a biased averaging of* $N_{\rm H}$*, a flatter spectral slope is obtained, compared to the straight averaging.*

Model	parameter								
	Type-1 AGN								
	Γ	$N_{\rm H}$	Energy	EW	σ	R_{in}	R_{out}	i	χ^2_ν/dof
		cm^{-2}	keV	eV	keV	R_g	R_g	deg	
Gaussian	$1.75^{+0.02}_{-0.02}$	$7.9^{+0.9}_{-0.6}$	$5.9^{+0.2}_{-0.1}$	420^{+35}_{-30}	$0.69^{+0.05}_{-0.05}$	–	–	–	1.35/68
diskline	$1.73^{+0.02}_{-0.01}$	7.5^{+1}_{-1}	6.40*	480^{+60}_{-60}	–	$6.4^{+1.8}_{-0.4}$	22^{+6}_{-3}	$29.1^{+3.2}_{-0.9}$	0.70/67
laor	$1.74^{+0.01}_{-0.02}$	$7.5^{+1.0}_{-0.9}$	6.40*	560^{+90}_{-110}	–	$3.1^{+1.2}_{-0.8}$	400_{-120}	$29.6^{+1.8}_{-1.7}$	0.73/67
	Type-2 AGN								
	Γ	$N_{\rm H}$	Energy	EW	σ	R_{in}	R_{out}	i	χ^2_ν/dof
		cm^{-2}	keV	eV	keV	R_g	R_g	deg	
Gaussian	$1.59^{+0.02}_{-0.01}$	$5.1^{+0.9}_{-0.8}$	$6.34^{+0.03}_{-0.03}$	280^{+25}_{-15}	$0.27^{+0.04}_{-0.02}$	–	–	–	0.83/64
diskline	$1.59^{+0.01}_{-0.01}$	$5.0^{+0.8}_{-0.9}$	6.40*	320^{+25}_{-30}	–	$6.0^{+0.1}$	800^{+400}_{-360}	$33.2^{+1.4}_{-2.2}$	0.80/63
laor	$1.61^{+0.02}_{-0.01}$	$5.3^{+0.9}_{-0.8}$	6.40*	455^{+45}_{-30}	–	$6.2^{+1.5}_{-0.2}$	400_{-100}	$30.1^{+0.6}_{-1.8}$	0.66/63

* fixed

states of iron (i.e., <Fe XVI). The line shape appears to be as predicted from disk theory and skewed toward energies lower than the rest energy of the emission line. The simplest interpretation of the skewed shape of the line is that it is due to Doppler and gravitational redshifts from the deep gravitational potential (the inner parts of a disc around a massive black hole). A strong red wing is indicative of gravitational redshifts close to a central black hole, and accretion disk models provide an excellent description of the data. Such line profile can be fitted with a relativistic profile from an accretion disc around either a Schwarzschild (non-rotating) or a Kerr (rotating) black hole (`XSPEC` models `diskline` and `laor`, respectively; Fabian et al. 1989; Laor 1991).

In both models we fixed the line energy to 6.4 keV and the emissivity index (-2 for `diskline` and 3 for `laor`) and fitted the rest of the parameters: inner R_{in} and outer R_{out} radii and inclination angle of the disc i. The initial parameters for the last stable orbit are 6 R_g for a non-rotating black hole, and 1.235 R_g for a maximally rotating black hole. The maximum values allowed by the models for the outer radius are 1000 R_g and 400 R_g, for the `diskline` and `laor` models, respectively. The resulting values after fitting are presented at Table 4.1. The results for the inclination angle are close to the standard value of 30 deg observed for a wide sample of AGN, consistent with the sharp drop near 7 keV and observed peak around the rest energy (6.4 keV).

The `laor` and `diskline` model yield similar reduced χ^2_ν, but the disk line model,

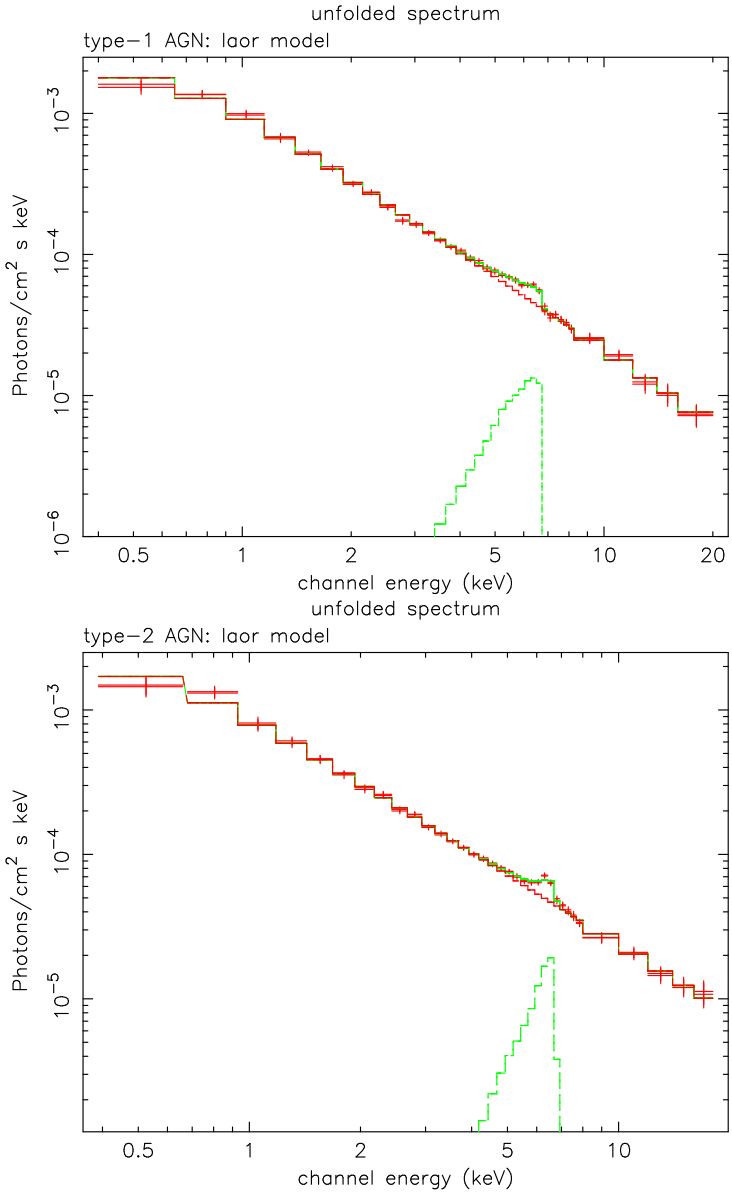

Figure 4.5: The unfolded stacked X-ray spectra and best fit model (laor) representative of the type-1 and type-2 AGN. Note that the resulting line profiles from the laor model differ for type-1 and type-2 AGN. The former shows a broad-shaped component without an evident peak, and the latter is represented by a more narrow component centred at 6.4 keV.

at least for type-1 AGN spectra prefers an inner disk radius at the last stable orbit and an unreasonably small outer radius.

In order to estimate the errors for the equivalent widths, we assumed the relative errors to be the same as that of the line flux, because the errors in the continuum at the position of the Fe line are negligible compared to this. It was found to have an average equivalent width of 560^{+90}_{-110} eV (`laor` model).

4.4.2 Fe line in type-2 AGN

Our initial fit for the unfolded spectrum was an absorbed power law with a Gaussian component to represent the iron line. Moreover we used, as for type-1 AGN spectra, disk line models to fit our asymmetric line profiles. Disk line models provide a good fit to the red wing of the data. Results are shown in Table. 4.1. As an additional test, we use an additional zero-width Gaussian to fit a possible narrow line component in the Fe emission separately, which could come from reflection in material much further away from the accretion disk, e.g. in the molecular torus, but this does not improve our χ^2_ν significantly (most probably due to the lack of statistics) and therefore we neglect this Gaussian.

Again, we assumed the relative error of the equivalent width to be that of the line flux. It was found to have an average equivalent width of 455^{+45}_{-30} eV (laor model).

Another intriguing result concerns the redshift distribution of our sources. Most of our type-2 objects are located in a quite narrow redshift bin between 0.5 to 1, and hence these objects contribute the most to the mean spectrum. From this point of view, it is possible to say that the obtained line profile is representative of nearby type-2 AGN ($z < 1$), and must be common for low z sources. Unfortunately, in most cases, the individual source spectra did not have high enough signal to noise ratios to apply a more physical model to fit the line profile; only a very narrow component is observed in the individual spectra.

4.5 Discussion

Mateos et al. (2005) conducted a detailed study of the Fe K_α emission in the individual spectra of the 123 brightest sources (we used all of their sources for which redshift information is available) with the best spectral quality (more than 500 MOS+pn background subtracted counts in the 0.2–12 keV band). This analysis showed that the signatures of line emission with F-test significance more than 95% were detected only in 8 sources (1 type-1 AGN, 5 type-2 AGN and 2 unidentified sources). Although in some sources the profiles of the lines did not appear to be symmetrical, the signal to noise of the spectra was not high enough to use more physical models. Therefore the lines were fitted with a Gaussian model. The centroids of the lines are found to be consistent with the rest frame energy of ~ 6.4 keV, which corresponds to the neutral Fe line. The equivalent widths of the lines were between 126 and 328 eV, and only one objects shows EW of 976 eV. These results differ significantly from our results. However, it is important to note that we used the average (de-redshifted) spectra of

type-1 and type-2 AGN, and hence, our data had much better signal to noise. As was already discussed, the contribution of the broad component in objects with broad Fe lines is difficult to detect in the individual spectra, since its contribution is less than 10% above the continuum over most of the spectrum.

A Doppler-broadened line with a full width at half-maximum, $FWHM \sim 150,000$ km s^{-1} can only be produced in the inner region of a relativistic accretion flow by fluorescence (Fabian et al. 2002). The observed FWHM and EW is larger than the average value found in Seyfert 1 galaxies ($\sim$ 500 eV, e.g. Nandra et al. 1997), but similar to the FWHM of some of the brightest nearby active galaxies (for example, to MCG-6-30-15 with z=0.007749).

One of the explanations for the large EWs for these objects can be given by a model including ionized disc reflection with lines and edges from different ionization stages of iron blurred together by relativistic effects (Ross & Fabian 1993, Fabian et al. 2002b). In this model, the value of the Fe abundance determines the relative importance of the line complex in respect to the comptonization bump, seen at energies exceeding 10 keV. Since the observed equivalent width of the broad Fe line is high, while the amplitude of a possible reflection component observed above 10 keV is small, this model yields a high Fe abundance as an explanation of the observation. This is in fact a novel method of measuring Fe abundance in QSO at X-rays, which in addition to the determination of redshifts will allow future X-ray surveys to give insight in the chemical evolution of the host environment of QSO. This model has been applied for several nearby objects and can account for all the observed spectral features, but yields a large iron overabundance of 3–7 $\times$ solar (Tanaka et al. 2004, Boller et al. 2003). In our sample we also most likely obtain the large EW as the result of a high metallicity. To test this idea, we used the blurred ionised reflection models (Ross & Fabian 1993) with an iron abundance of 3 $\times$ solar (as needed for MCG-6-30-15) in order to obtain a high EW. The results describe our data very well.

An additional reason why our large equivalent width may be connected with a large metallicity is that most of our objects are quite distant and rather luminous AGNs. As shown by Shemmer et al. (2004) using an optically selected sample of luminous high-z QSOs, the metallicity is correlated with the accretion rate, which is in turn related to the luminosity. It is possible that the large equivalent widths are representative of a high metallicity, since these objects are both distant and luminous.

Our results are most consistent with a Laor model with inner disk radius well inside the maximum stable orbit for a Schwarzschild black hole, implying that the average X-ray bright AGN should contain rotating Kerr BH at their centres [1]. If this is the case, it implies that the spin will affect demographic arguments relating the AGN luminosity function to the mass function of remnant black holes in nearby galaxies (Sołtan 1982) since the radiative efficiency of accretion will increase. Indeed, this is

[1]The Laor (1991) model which is appropriate for spin a/m=0.998 gives a best fit $R_{\rm in} = 3$. Dovčiak, Karas & Yaqoob (2003) plot the maximum redshift as a function of radius and spin (their Fig. 2). Assuming that the spectral fit is determined by the maximum redshift and that the emitting region is outside the radius of marginal stability (see Krolik & Hawley 2003 for a discussion of that point), $R_{\rm in} = 3$ corresponds to $a/m > 0.6$.

postulated by recent work updating the Sołtan argument with modern galaxy – black hole correlation functions and AGN energetics based on hard X-ray surveys (Yu & Tremaine 2002, Elvis, Risaliti & Zamorani 2002, Marconi et al. 2004). Accretion is expected to build massive black holes with significant spin (Hughes & Blandford 2003; Volonteri et al. 2004).

The intensity of the relativistic line in our mean spectra implies that this line must be present in the majority of AGN in our sample. Using a similar technique we followed the same procedure with a source list and spectra from the XMM-Newton observation of the Chandra Deep Field South (see Chapter 3). The results are consistent with our analysis of the LH and also with an independent analysis of the Chandra deep fields data by Brusa et al. (2005). We also investigated, whether the signal could be dominated by a small number of objects with extremely bright features. For this purpose we applied a σ-clipping before averaging our spectral bins, but the resulting spectra do not differ significantly.

In future work we plan to investigate the dependence of the line on other parameters, such as redshift or luminosity. We will also consider a composite model with a range of inclinations.

4.6 Conclusions

This chapter presented analysis of the Fe line profile from the mean EPIC-pn and MOS1/2 X-ray spectra of type-1 and type-2 AGN together with the general information about 770 ksec XMM-Newton deep survey on the LH field. By shifting the individual spectra to the rest-frame and combining them together, we have derived the average X-ray spectral properties for the sample of 104 sources with redshift identification and photon counts > 200. The resulting mean spectra of the different AGN populations were parameterized with a simple power law model. The continuum at 4–7 keV shows residuals above the power-law model, suggesting the presence of a strong broad feature, most likely a relativistic iron disk line. We model the broad component with several line models (`Gaussian`, `diskline`, `laor`) which describe different origins of the line, depending on the BH spin.

Our results imply that this component is a relativistically broadened fluorescent Fe line from the accretion disk around a Kerr (rotating) black hole (Laor 1991), with equivalent widths of ~ 560 eV and ~ 460 eV for the average spectra of type 1 and 2 AGN, respectively. The most plausible explanation for a such broad and strong iron line may be a high metallicity in the average AGN population.

This detection of the relativistically broadened lines beyond the local universe requires the revision of the current XRB models.

Chapter 5

Conclusions

In this thesis we analysed the deepest observations carried out with XMM-Newton in the Chandra Deep Field South and the Lockman Hole. These two fields provide a unique opportunity to study physical and evolutionary properties of different source classes which make up the X-ray background using a statistically significant sample of sources. The main goal of the work was a further improvement of the knowledge about X-ray properties of AGN in the distant Universe using the statistical treatment of these large samples of detected sources.

The main results can be summarized as follows.

5.1 Statistical properties of Chandra Deep Field South sources

The 370 ksec XMM-Newton observation of the CDFS subtends solid angle of 0.223 deg^2 and reached the flux limit of 1×10^{-16} and 9×10^{-16} erg cm^{-2} s^{-1} in the 0.5–2 and 2–10 keV bands, respectively. We created a source catalog of the 363 sources and made comparison in different aspects between our source list and available Chandra source catalogs. The main results are the following (Chapter 2).

• The derived log N–log S relation is consistent with previous Chandra 1 Ms results. The cumulative number counts in the very hard band (5–10 keV) have a steeper slope than the soft (0.5–2 keV) and hard (2–10 keV) bands source counts. This result is mainly due to the hardening of the average spectrum at low fluxes (and as a consequence the higher fraction of hard band sources at fainter fluxes), confirming the idea about the existence of a fainter and progressively harder population of sources that are likely to fill the remaining fraction of the hard X-ray background. Most of the sources contributing to this band should be strongly absorbed AGN at relatively low redshifts.

• Comparison between the XMM-Newton, Chandra 1 Ms (Giacconi et al. 2002) and E-CDFS (Lehmer et al. 2005) source catalogs reveal a good agreement between the source positions ($\sim$ 2 arcsec), showing that the XMM-Newton datasets are not significantly affected by source confusion. The comparison of the derived fluxes in the soft and hard bands reveal a reasonable agreement between the obtained values, however with a noticeable scatter for sources with relatively low hard band fluxes. The

scatter could indicate possible variability of some of the AGN between the different observation epochs, although it could also be due to systematic effects of the source detection procedure.

• We create a catalog of the 15 extended sources in our field, 7 of them are known previously from the deep Chandra observation and have been identified with galaxies and groups/clusters of galaxies. From the number of the detected extended sources we estimated the cluster number density of 84± 22 clusters per square degrees at the 4×10^{-16} erg cm^{-2} s^{-1} flux level in the 0.5–2 keV band. Such cluster number density is among the highest known, and in agreement with other estimates at such flux levels. Our preliminary spectral analysis of these objects shows that the X-ray luminosities ($L_X \sim 10^{41}$–10^{43} erg s^{-1}) and temperatures ($kT < 3$ keV) are in good agreement with previous findings from deep surveys for such bright objects.

• From colour-colour and colour-flux diagrams we found that 165 newly detected XMM-Newton sources have similar hardness ratio properties to previously identified sources from 1 Ms Chandra dataset, and most likely have a similar fraction of type-1 to type-2 AGN.

5.2 Spectral analysis of individual sources and statistical treatment of background AGN population

We constructed a large sample of AGN over a wide range of redshifts and luminosities for accurate source-by-source X-ray spectral analysis with different models, selecting only the sources with spectroscopic/photometric redshift information and with number of counts larger than 100 (pn detector). The existing Chandra 1 Ms source sample (Tozzi et al. 2005) provided a unique opportunity for comparison between these two datasets. Statistical analysis of 127 source spectra (78 type-1 AGN, 39 type-2 AGN and 10 galaxies) reveals the following properties (Chapter 3).

• We observe a separation between the type-1 and the type-2 AGN as a consequence of their different absorption column densities. We do not notice statistically significant difference between the spectral slopes of the two AGN classes.

• More than 90% of the source spectra are in agreement with the unified model, however a fraction of 'atypical' sources (absorbed type-1 AGN and unabsorbed type-2 AGN) was also discovered.

• Although, we cannot reach any strong conclusion about three unabsorbed type-2 AGN, due to low statistics of the data, we can confirmed previous discovery from other deep and shallow surveys about absorbed type-1 AGN. We detected that $\sim$ 10% of high-redshift (z>2), high-luminosity ($L_X > 10^{44}$ erg s^{-1}) objects optically classified as unobscured BLAGN are absorbed in X-rays by column densities of $\sim 10^{22}$ cm^{-2}. The observed mismatch between X-ray and optical properties may be explained by the difference in the physical conditions surrounding the emission regions.

• Most AGN spectra require only an (un)absorbed power law model, however we detect a fraction of sources with additional spectral components such as a soft excess (11 sources) and an iron line (7 sources).

• No obvious correlation between spectral continuum and absorption or between Γ, $N_{\rm H}$ and redshift are found.

• The staked spectrum of the most distand type-2 QSO, derived here for the first time, shows a strong X-ray absorption with a clear soft component (fitted with a scattering/partial covering model), implying that for the distant (z > 2.5) type-2 QSOs this component is required. The general X-ray properties of the average high-z type-2 QSO spectrum is comparable to that of the highly absorbed sources in the local universe.

• We confirm a progressive hardening for the combined integrated spectra for faint objects, which at first was noted in the Chandra analysis of CDFS. Using the staking procedure to obtain integrated spectra for faint objects combined in groups by flux, we detected a clear evolution of decrease of $\langle\Gamma\rangle$ with decreasing flux in the hard 2–10 keV band. However, the detailed comparison of $\langle\Gamma\rangle$ values shows that the spectral slopes determined from XMM-Newton data are steeper typically by 0.1 than these detected by Chandra, even if exactly the same energy range (1–7 keV) is used by both instruments. The discrepancy becomes even larger if the soft 0.3–1 keV energy range is included in the fitting.

• The comparison between Chandra and XMM-Newton fitting strategy reveals that there is a strong dependence between the obtained spectral slope and absorption in the selected energy range for spectral fitting. As a result, for sources exhibiting low intrinsic absorption Chandra, due to the limited energy range, obtained systematically higher values of the absorption columns and consequently flatter power law slopes.

5.3 The iron line feature in the mean rest-frame spectra of type-1 and type-2 AGN

The Fe K_α line is arguably the most important component in the observed X-ray spectrum of an AGN, however the detailed studies of this component required the high quality data, which so far is impossible to reach in the individual spectra of distant AGN. Using the high quality data obtained in the deepest 770 ksec XMM-Newton observation on the Lockman Hole field, we applied an alternative approach for studying iron line contribution to the AGN spectra. By shifting the individual spectra to the rest-frame and combining them together, we have avoided the line smearing due to the large redshift range over which AGN spectra are commonly summed, and in the same time increased statistics of the spectra. In this way, we derived the mean pn and MOS1/2 spectra for the type-1 and type-2 AGN using a sample of 104 sources (Chapter 4). The most important conclusions which follow from our analysis are the following.

• After parameterization with a simple power law model, the continua at 4–7 keV show residuals above the power-law model, suggesting the presence of a strong broad feature, most likely a relativistically broadened fluorescent Fe K_α line at rest-frame energy of $\sim$ 6.4 keV.

• Modelling of the strong red wing of the Fe line with different line models shows

that a Laor line profile (i.e. rotating Kerr black hole) with an inner disk radius smaller than the last stable orbit of a Schwarzschild black hole, indicates some component of spin in the average black hole. However, the statistical quality of the data does not rule out a Schwarzschild black hole with the entire emission comming from the last stable orbit.

• Equivalent widths of the broad relativistic lines range between 400–600 eV, which are larger than typical values found in most nearby AGN.

• We used the disk reflection model to compare the observed strength of the line with the amplitude of the reflection component, concluding that to consistently describe the observations the average iron abundance should be about three times the solar value. This result could imply that the presence of a strong, relativistic iron line in rest-frame spectra of the XRB sources is possibly due to a high metallicity in the average population.

• In spite of the variety and complexity of Fe features at low z bright objects (both type-1 and type-2 Seyfert), the average line shape at higher redshift is consistent with a relativistic disc line for type-1 and type-2 AGN with some evidence of an additional narrow component for type-2 AGN.

• The detection of the relativistically broadened lines beyond the local universe requires the revision of the current population synthesis models for the X-ray background: a very broad line feature, which is expected in the average X-ray background spectra (Fabian et al. 2000, Gilli et al. 2001), should be included in future XRB models.

• These findings strongly reinforce the science case of the XEUS/Constellation-X mission; with the very large collecting area we can expect to measure the relativistic Fe line parameters of individual objects out to very high redshifts ($z \approx 10$) and explore the evolution of black hole spin.

5.4 Discussion and Future work

Thanks to the deep and shallow observations of the X-ray background with Chandra and XMM-Newton, our knowledge about high-z sources improved fundamentally over last years. However, together with shedding the light on physical nature of these sources we also created new questions to be answered as well. This thesis helps to improve our knowledge about distant Universe, however we cannot obtained robust answer for the two of most interesting and important questions of modern extragalactic astronomy: *How significant is the presence of the relativistic iron line in the AGN population at different redshifts?* and *Do the unified scheme of AGN really work in the distant Universe?*

Hopefully, some of these questions will be answered with the ongoing shallow surveys, such as COSMOS and E-CDFS. These survey, although not as deep as the data presented here, due to its significantly larger area, will contain enough objects to perform statistycal studies for different type of background objects.

The significance of the broad iron line detected in this dissertation is enormous for the physics in the presence of strong gravitational field, as well as for cosmological

evolution of the black holes. Various models have been tested to fit our detected profile (Müller, priv. comm.).

With this vast amount of coming high-quality X-ray data from XMM-Newton and Chandra, and theoretical work motivated by our results, we will soon know more about sources that inhabit the X-ray Universe.

Bibliography

[1] Abrassart, A., Czerny, B., 2000, A&A, 356, 475

[2] Akiyama, M., Ohta, K., Yamada, T., et al. 2000, ApJ, 532, 700

[3] Akiyama, M., Ueda, Y., Ohta, K., et al. 2003, ApJS, 148, 275

[4] Alexander, D. M. et al., 2003, AJ, 126, 539

[5] Antonucci, R., Miller, J. S., 1985, ApJ, 297, 621

[6] Antonucci, R., 1993, ARA&A, 31, 473

[7] Arnaud, K., 1996, in: *Astronomical Data Analysis Software and Systems*, Jacoby G., Barnes J., eds, ASP Conf. Series Vol. 101, p17

[8] Awaki, H., Kunieda, H., Tawara, Y., & Koyama, K., 1991, PASJ, 43, 37

[9] Balestra, I., Bianchi, S., & Matt, G. 2004, A&A, 415, 437

[10] Bardeen, J. M., Press, W. H., Teukolsky, S. A. 1972, ApJ 178, 347

[11] Barger, A. J., Cowie, L. L., Mushotzky, R. F., Richards, E. A. 2001, AJ, 121, 662

[12] Barger, A., Cowie, L. L., Brandt, W. N., et al. 2002, AJ, 124, 1839

[13] Barger, A., Cowie, L. L., Brandt, W. N., et al. 2003, AJ, 126, 632

[14] Bassani, L., Dadina, M., Maiolino, R., et al. 1999, ApJS, 121, 473

[15] Bauer, F. E., Alexander, D. M., Brandt, W. N, et al. 2004, AJ, 128, 2048

[16] Bauer, F. E., Vignali, C., Alexander, D. M., et al. 2003, AN, 324, 175

[17] Bennert, N., Falcke, H., Schulz, H., et al. 2002, ApJ, 574, 105

[18] Boller, Th., Gallo, L., 2005, in prep.

[19] Boller, Th., Tanaka, Y., Fabian, A., et al. 2003, MNRAS, 343, 89

[20] Brandt, W. N, Alexander, D. M., Hornschemeier, A. E., et al. 2001, AJ, 122, 2810

[21] Brandt, W. N., Hornschemeier, A. E., Schneider, D. P., et al. 2001, ApJ, 558, L5

[22] Brandt, W., & Hasinger G., 2005, ARAA, 43, 827

[23] Brusa, M., Comastri, A., Mignoli, M., et al. 2003, A&A, 409, 65

[24] Brusa, M., Gilli, R., & Comastri, A. 2005, ApJ, 621, 5

[25] Chartas, G., Worrall, D. M., Birkinshaw, M., 2000, ApJ, 542, 655

[26] Comastri, A., Setti, G., Zamorani, G. & Hasinger, G. 1995, A&A, 296, 1

[27] Comastri, A., Fiore, F., Vignali, C., et al. 2001, MNRAS, 327, 781

[28] Comastri, A., 2004. Chapter 8 in "Supermassive Black Holes in the Distant Universe", 245. Ed. A. J. Barger, Kluwer Academic

[29] Comastri, A., 2004, in Maiolino R., Mujica R., eds, Proc. Multiwavelength AGN

[30] Comastri, A., Brusa, M., & Civano, F., 2004, MNRAS, 351, L9

[31] Croom, S. M., Smith, R. J., Boyle, B. J., et al. 2004, MNRAS, 349, 1397

[32] De Luca, A., & Molendi, S. 2004, A&A, 419, 837

[33] Della Ceca, R., Maccacaro, T., Caccianiga, A., et al. 2004, A&A, 428, 383

[34] Della Ceca, R., Castelli, G., Braito, V., et al. 1999, ApJ, 524, 674

[35] den Herder, J.W., Brinkman, A.C., Kahn, S.M., et al., 2001, A& A 365, 7

[36] Dickey, J. M., & Lockman, F. J. 1990, ARA&A, 28, 215

[37] Dovčiak, M., Karas, V., & Yaqoob T. 2003, ApJS, 153, 205, astro-ph/0403541

[38] Dwek, E., et al. 1998, ApJ, 508, 106

[39] Ehle, M., et al. 2004, *XMM-Newton* Users's Handbook, v2.2

[40] Elvis, M., Lockman, F. J., Fassnacht, C., 1994, ApJS, 95, 413

[41] Elvis, M., Risaliti, G., Zamorani, G., 2002, ApJ 565, L75

[42] Fabian, A. C., Rees, M. J., Stella, L., & White, N. E. 1989, MNRAS, 238, 729

[43] Fabian, A. C., Iwashawa, K., Reynolds, C.S., & Young, A.J. 2000, PASP, 112, 1145

[44] Fabian, A. C., Vaughan, S., Nandra, K., et al. 2002, MNRAS, 335, 1F

[45] Fabian, A. C., Ballantyne, D. R., Merloni, A., et al. 2002b, MNRAS, 331, 35F

[46] Fabian, A. C., & Iwasawa, K., 1999, MNRAS, 303, L34

[47] Fabian, A. C., 2004, In 'Coevolution of Black Holes and Galaxies', Carnegie Observatories Astrophysics Series, Vol. 1, ed. L. C. Ho (Cambridge: Cambridge Univ. Press), astro-ph/0304122

[48] Fan, X., Strauss, M. A., Schneider, D. P., et al. 2001, AJ, 121, 54

[49] Fanaroff, B. L. & Riley, J. M.,1974, MNRAS, 167, 31

[50] Ferrarese, L., & Ford, H., 2005. Space Sci. Rev., 116, 523 (astro-ph/0411247)

[51] Field, G. B., & Perrenod, S. C. 1977, ApJ, 215, 717

[52] Fiore, F., La Franca, F., Vignali, C., et al. 2000, New Astronomy, 5, 143.

[53] Finoguenov, A., Briel, U. G., & Henry, J. P., 2003, A&A, 410, 777

[54] Franceschini, A., Braito, V., Fadda, D., 2002, MNRAS, 335, L51

[55] Freyberg, M., Briel, U., Dennerl, K., et al. 2003, Proc. SPIE 5165, 'X-Ray and Gamma-Ray Instrumentation for Astronomy XIII', San Diego, USA, 2003, eds. K.A. Flanagan & O.H.W. Siegmund

[56] Gallo, L., 2004, PhD thesis, MPE

[57] Gandhi, P., Fabian, A. C., 2003, MNRAS, 339, 1095

[58] Gandhi, P., Crawford, C. S., Fabian, A. C., Johnstone, R. M. 2004 MNRAS, 348, 529

[59] Gebhardt, K., Kormendy, J., Ho, L., et al. 2000, ApJ, 543, L5

[60] Gendreau, K. C.,, Barcons, X., & Fabian, A. C. 1998, MNRAS, 297, 41

[61] Genzel, R., Eckart, A., Ott, T., Eisenhauer, F. 1997, MNRAS, 291, 219

[62] Georgantopoulos, I., & Zezas, A., 2003, ApJ, 594, 704

[63] Giacconi, R., Gursky, H., Paolini, F., & Rossi, B., 1962, Phys. Rev. Lett. 9, 439

[64] Giacconi, R., Rosati, P., Tozzi, P., et al. 2001, ApJ, 551, 624

[65] Giacconi, R., Rosati, P., Tozzi, P., et al. 2002, ApJS, 139, 369

[66] Giavalisco, M., et al. 2004, ApJ, 600, L93

[67] Gilli, R., Comastri, A., Setti, G., & Brunetti, G., 1999, NewA, 4, 45

[68] Gilli, R., Salvati, M., & Hasinger, G. 2001, A&A, 366, 407

[69] Gilli, R., Cimatti, A., Daddi, E., et al. 2003, ApJ, 592, 721

[70] Gilli, R., Daddi, E., Zamorani, G., et al. 2005, A&A, 430, 811

[71] Green, P. J., Schartel, N., Anderson, S. F., et al. 1995, ApJ, 450, 51

[72] Guainazzi, M., Matt, G., Perola, G.C, 2005, A&A, accepted

[73] Haardt, F., & Maraschi, L., 1991, ApJ, 380, L5

[74] Haardt, F., & Maraschi, L., 1993, ApJ, 413, 507

[75] Halpern, J. P., 1984, ApJ, 281, 90

[76] Hasinger, G., Burg, R., Giacconi, R., et al., 1993, A&A, 275, 1

[77] Hasinger, G., Burg, R., Giacconi, R., et al. 1998, A&A, 329, 482

[78] Hasinger, G., Altieri, B., Arnaud, M., et al. 2001, A&A, 365, L45

[79] Hasinger, G. 2000, In 'ISO Surveys of a Dusty Universe', eds. D. Lemke, M. Stickel, K. Wilke, (astro-ph/0001360)

[80] Hasinger, G. 2004, Nuclear Physics B (Proc. Suppl.) 132, 86, (astro-ph/0310804)

[81] Hasinger, G., Miyaji, T., & Schmidt, M., 2005, A&A, submitted

[82] Holt, S. S., Mushotzky, R. E., Boldt, E. A., et al. 1980 ApJ, 241, L13

[83] Hornschemeier, A. E., Brandt, W. N., Alexander, D. M., et al. 2002, ApJ, 568, 82

[84] Hornschemeier, A., E., Bauer, F., Alexander, D., et al. 2003, AJ, 126, 575

[85] Hughes, S. A., Blandford, R. D. 2003, ApJ 585, L101

[86] Ishisaki, Y., et al., 2001, PASJ, 53, 445

[87] Jansen, F., Lumb, D., Altieri, B., et al. 2001, A&A 365, 1

[88] Kaspi, S., Smith, P.S., Netzer, H., et al. 2000, ApJ, 533, 631

[89] Krivonos, R., Vikhlinin, A., Churazov, E., et al. 2005, ApJ 625, 89

[90] Krolik, J. H., Hawley, J. F. 2002, ApJ 533, 754

[91] Laor, A. 1991, ApJ, 376, 90

[92] Le Fevre, O., et al. 2004, A&A, 428, 1043

[93] Lehmann, I., Hasinger, G., Schmidt, M., et al. 2001, A&A, 371, 833

[94] Lehmann, I., Hasinger, G., Schmidt, M., et al. 2000, A&A, 354, 34

[95] Lehmer, B., Brandt, W., Alexander, D., et al. 2005, ApJ, accepted

[96] Ledlow, M. J., Owen, F., 1996, AJ, 112, 9L

[97] Lockman, F. J., Jahoda, K., & McCammon, D. 1986, ApJ, 302, 432

[98] Lonsdale, C. J., et al. 2003, PASP, 115, 897

[99] Maccacaro, T., della Ceca, R., Gioia, I., et al. 1991, ApJ, 374, 117

[100] Magdziarz, P., & Zdziarski, A., 1995, MNRAS, 273, 837

[101] Magorrian, J., et al. 1998, AJ, 115, 2285

[102] Mainieri, V., Bergeron, J., Rosati, P., et al. 2002, A&A, 393, 425

[103] Mainieri, V., Rosati, P., Tozzi, P., et al. 2005, A&A, 437, 805

[104] Maiolino, R., Marconi, A., Salvati, M., et al. 2001, A&A, 365, 28

[105] Maiolino, R., Marconi, A., & Oliva, T., 2001, A&A, 365, 37

[106] Marconi, A., Risaliti, G., Gilli, R., et al. 2004, MNRAS 351, 169

[107] Marshall, F. E., Boldt, E. A., Holt, S. S., et al. 1980, ApJ, 235, 4

[108] Mason, K.O., Breeveld, A., Much, R. et al. 2001, A&A 365, 36

[109] Mateos, S., Barcons, X., Carrera, F. J., et al. 2005, A&A, accepted

[110] Mather, J.C., Cheng, E. S., Eplee, R. E., et al. 1990, ApJ, 354, L37

[111] Matt, G., Brandt, W.N., Fabian, A.C., 1996, MNRAS 280, 823

[112] Matt, G., Fabian, A. C., Guainazzi, M., et al. 2000, MNRAS, 318, 173

[113] Matt, G., Guainazzi, M., Perola, G., et al. 2001, A&A, 377L, 31

[114] Miller, K., & Stone, J., 2000, ApJ, 534, 398

[115] Miyaji, T., Hasinger, G., Schmidt, M., 2000, A&A, 353, 25

[116] Miyaji, T., Griffiths, R. E., 2002, ApJ, 564, 5

[117] Moran, E. C., Filippenko, A. V, Chornock, R., 2002, ApJ, 579, 71

[118] Moretti, A., Lazzati, D., Campana, S., Tagliaferri, G., 2002, ApJ, 570, 502

[119] Moretti, A., Campana, S., Lazzati, D., Tagliaferri, G., 2003, ApJ, 588, 696

[120] Mushotzky, R. F., 1984, Adv. Space Res. 3, 157

[121] Nandra, K., Mushotzky, R. F., Arnaud, K., et al. 2002, ApJ, 576, 625

[122] Nandra, K., George, I. M., Mushotzky et al. 1997, ApJ, 477, 602

[123] Norman, C., Hasinger, G., Giacconi R., et al. 2002, ApJ, 571, 218

[124] Norman, C., Ptak, A., Hornschemeier, A., et al. 2004, ApJ, 607, 721

[125] Osterbrock, D., & Shaw, R., 1988, ApJ, 327, 89

[126] Osterbrock, D.E., 1989, Astrophysics of Gaseous Nebulae and Active Galactic Nuclei, University Science Books

[127] Page, M. J., McHardy, I. M., Gunn, K. F., et al. 2003, AN, 324, 101

[128] Panessa, F., & Bassani, L., 2002, A&A, 394, 435

[129] Pappa, A., Georgantopoulos, I., Stewart, G.C., & Zezas, A.L., 2001, MNRAS, 326, 995

[130] Paolillo, M., Schreier, E. J., Giacconi, R., et al. 2004, ApJ, 611, 93

[131] Papovich, C., et al. 2004, ApJS, 154, 70

[132] Perola, G. C., et al. 2002, A&A, 389, 802

[133] Perola, G. C., Puccetti, S., Fiore, F., et al. 2004, A&A, 421, 491

[134] Peterson, B.M., Wanders, I., Bertram, R., et al. 1998, ApJ, 501, 82

[135] Pounds, K., Nandra, K., Stewart, G. C., et al. 1990, Nature, 344, 132

[136] Pozdnyakov, L., Sobol I., & Sunyaev, R., 1979, A&A, 75, 214

[137] Proga, D., Stone, J., Kallman, T., 2000, ApJ, 543, 686

[138] Rees, M., 1984, ARA&A, 22, 471

[139] Reeves, J. N., Turner, M. J., Bennie, P. J. et al. 2001, A&A, 365L, 134

[140] Reynolds, C. S., 1997, MNRAS, 286, 513

[141] Revnivtsev, M., Gilfanov, M., Sunyaev, R., et al. 2003, A&A, 411, 329

[142] Renzini, A., et al. 2003, In *The Mass of Galaxies at Low and High Redshift*, eds. R. Bender and A. Renzini (New York: Springer), 332

[143] Risaliti, G., Maiolino, R., & Salvati, M., 1999, AJ, 522, 157

[144] Rix, H., et al. 2004, ApJS, 152, 163

[145] Rosati, P., della Ceca, R., Burg, R., et al. 1995, ApJ, 445, 11

[146] Rosati, P., Borgani, S., Norman, C., 2002, ARAA, 40, 539

[147] Rosati, P., Tozzi, P., Giacconi, R., et al. 2002, ApJ, 566, 667

[148] Ross, R. R., Fabian, A. C. 1993, MNRAS 261, 74

[149] Ross, R.R., Fabian, A.C., 2005, MNRAS, 358, 211

[150] Schmidt, M., Schneider, D. P., Gunn, J., 1995, AJ, 110, 68

[151] Schmidt, M., Hasinger, G., Gunn, J., et al. 1998, A&A, 329, 495

[152] Schödel, R., Ott, T., Genzel, R. 2002, Natur, 419, 694

[153] Schwartz, D. A. 1980, PhyS, 21, 644

[154] Schwartz, D. A., Tucker W. H. 1988, ApJ 332, 157

[155] Schurch, N. J., Warwick, R. S., Griffiths, R. E., Kahn, S. M., 2004, MNRAS, 350, 1

[156] Shafer, R. A., & Fabian, A. C., 1983, IAUS 104, 333

[157] Shemmer, O., Netzer, H., Maiolino, R., et al. 2004, ApJ, 614, 547

[158] Silverman, J., Green, P., Barkhouse, W., et al. 2005, ApJ, 618, 123

[159] Snowden, S. L., Collier, M. R., & Kuntz, K.D., 2004, ApJ, 610, 1182

[160] Sołtan, A. 1982, MNRAS, 200, 115

[161] Sołtan, A. 2003, A&A, 408, 39

[162] Sołtan, A. M., Freyberg, M. J., Hasinger, G., 2005, A&A, 436, 67S

[163] Spergel, D. N., Verde, L., Peiris, H. V., et al. 2003, ApJ, 148, 175

[164] Stern, D., Moran, E. C., Coil, A.L., et al. 2002, ApJ, 568, 71

[165] Streblyanska, A., Bergeron, J., Hasinger, G., et al. Proceedings of the Second BeppoSAX Symposium 'The Restless High-Energy Universe', 2004, Nucl. Physics B. Suppl. Ser., 132, 232, astro-ph/0309089

[166] Streblyanska, A., Hasinger, G., Finoguenov, A., Barcons, X., Mateos, S., Fabian, A. C., 2005, A&A, 432, 395

[167] Strüder, L., Briel, U., Dennerl, K., et al. 2001, A&A 365, 18

[168] Szokoly, G., et al. 2004, ApJS, 155, 271

[169] Tanaka, Y., Nandra, K., Fabian, A. C., et al. 1995, Nature, 375, 659

[170] Tanaka, Y., Boller, Th., Gallo, L., et al. 2004, PASJ, 56, 9

[171] Tozzi, P., Rosati, P., Nonino, M., et al. 2001, ApJ, 562, 42

[172] Tozzi, P., Gilli, R., Mainieri, V., et al. 2005, accepted

[173] Turner, T. J., Pounds, K. A., 1989, MNRAS, 240, 833

[174] Turner, T. J., Weaver, K. A., Mushotzky, R. F., et al. 1991, ApJ, 381, 85

[175] Turner, T. J., George I. M., et al. 1997, ApJS, 113, 23

[176] Turner, T. J., Perola, G. C., Fiore, F., et al. 2000, ApJS, 531, 245

[177] Turner, M.J.L., Abbey, A., Arnaud, M., et al. 2001, A&A 365, 27

[178] Ueda, Y., Takahashi, T., Ishisaki, Y., et al. 1999, ApJ, 524, L11

[179] Ueda, Y., Akiyama, M., Ohta, K., Miyaji, T., 2003, ApJ, 598, 886

[180] Ulrich, M. H., 2000, A&A Rev. 10, 135

[181] Vanzella, E., et al. 2005, A&A, 434, 53

[182] Volonteri, M., Madau, P., Quataert, E., & Rees, M. 2005, ApJ, 620, 69

[183] Walter, R., Fink, H. H., 1993, A&A, 274, 105

[184] Warwick, R. S. & Roberts, T. P., 1998, AN, 319, 59

[185] Watanabe, C., Ohta, K., Akiyama, M., Ueda, Y., 2004, ApJ, 610, 128

[186] Weingartner, J., & Murray, N., 2002, ApJ, 580, 88

[187] Wilms, J., Christopher S., Begelman, M. C., et al. 2001, MNRAS, 328, 27

[188] Wilson, A. S., Yang, Y., 2002, ApJ, 568, 133

[189] Wilson, A. S., Elvis, M., Lawrence, A., Bland-Hawthorn, J., 1992, ApJ, 391, 75

[190] Wolf, C., et al. 2004, A&A, 421, 913

[191] Worsley, M., Fabian, A. C., Mateos, S., et al. 2004, MNRAS 352, L28

[192] Worsley, M., Fabian, A. C., Bauer, F., et al. 2005, MNRAS, 357, 1281

[193] Yaqoob, T., Padmanabhan, U., Dotani, T., Nandra, K., 2002, ApJ, 569, 487

[194] Yu, Q., & Tremaine, S. 2002, MNRAS, 335, 965

[195] Zamorani, G., Mignoli, M., Hasinger, G., et al. 1999, A&A, 346, 731

[196] Zdziarski, A. A., et al. 1994, MNRAS 269, L55

[197] Zdziarski, A. A., Johnson, W. N., Done, C., et al. 1995, ApJ, 438, 63

[198] Zhang, Y.-Y., et al. 2004, A&A, 413, 49

[199] Zheng, W., Mikles, V. J., Mainieri, V., et al. 2004, ApJS, L55, 73
332, 231

Personal data

Name: Alina Streblyanska

Date of birth: 05 August 1979

Place of birth: Kramatorsk (Ukraine)

Nationality: Ukrainian

Current adress:
Max Planck Institut für extraterrestrische Physik
Postfach 1312
D-85741, Garching, Germany

Tel: (+49) 89 30000-3611

E-mail: alina@mpe.mpg.de

Education

2002 – 2005 International Max-Planck Research School on Astrophysics (IMPRS) at Max Planck Institut für extraterrestrische Physik (Germany).

PhD in Astrophysics (Ludwig Maximillians Universität, Munich, Germany)

Thesis Project: Spectral properties of X-ray background sources

Thesis Advisor: Prof. Dr. Günther Hasinger

1996 – 2001 Diploma of Specialist (Honours) (equivalent to Master of Science degree) in Astronomy and Physics. Kharkov National University (Ukraine).

Topic: Determination of the chemical and mineralogical composition of the lunar surface using optical and IR-spectra

Advisor: Dr. Dmitriy Stankevich